Challenge Journal of
CONCRETE RESEARCH LETTERS

Vol.16 No.2 (2025)

acoustic emission aerated concrete artificial neural network compressive strength corrosion cracking ductility durability energy absorption ferrocement flexural strength fly ash fracture mechanics mechanical properties mortar nanoparticle reinforced concrete self-compacting concrete steam curing strengthening superplasticizer tensile strength workability waste disposal water a tion

TULPAR
ACADEMIC PUBLISHING

ISSN 2548-0928

Challenge Journal of Concrete Research Letters

E-mail: *cjcrl@challengejournal.com*

Web page: *cjcrl.challengejournal.com*

Tulpar Academic Publishing
www.tulparpublishing.com

Challenge Journal of Concrete Research Letters

CONTENTS

Research Articles

TULPAR
ACADEMIC PUBLISHING

Challenge Journal of Concrete Research Letters

Research Article

Tea waste ash: Characterization, pozzolanic activity and effects on the fresh properties of cement pastes

İlknur Bekem Kara [a,*], Cuma Kara [a]

[a] *Department of Construction Technology, Borçka Acarlar Vocational School, Artvin Çoruh University, 08400 Artvin, Türkiye*

ABSTRACT

It is a well-known fact that the use of agricultural wastes in cementitious composites by turning them into ash provides both ecological and economic benefits. Tea factories in Türkiye are located in the Eastern Black Sea region. Tea waste generated in factories locally causes environmental problems. This study focuses on the usability of the wastes left over from the products processed in the tea factory. Tea waste from Artvin, Türkiye was turned into ash at 850 °C. Physical, chemical, mineralogical, thermogravimetric and morphological properties of tea waste ash were examined. Pozzolanic activity test was performed to determine its usability in cement systems. Blended cement pastes were prepared by substituting up to 10% tea waste ash. Physical and chemical properties of blended cement pastes were determined. As a result, the tea waste ash was found to contain a high proportion of K_2O. The waste material does not show pozzolanic properties. The hydration of cement pastes has accelerated with tea waste ash. Tea waste ash substitution has increased standard consistency water of blended cement pastes. Tea waste ash substitution up to 8% provided the initial setting time included in the standard. It was concluded that tea waste ash could be used as a setting accelerator.

ARTICLE INFO

Article history:

Received	– January 7, 2025
Revision requested	– February 24, 2025
Revision received	– February 26, 2025
Accepted	– March 3, 2025

Keywords:
Tea waste ash
Agricultural waste utilization
Pozzolanic activity
Characterization techniques
Cement paste properties

Citation: Bekem Kara İ, Kara C (2025). Tea waste ash: Characterization, pozzolanic activity and effects on the fresh properties of cement pastes. *Challenge Journal of Concrete Research Letters*, 16(2), 51–59.

1. Introduction

Expansion of the construction sector driven by population growth has confronted humanity with unprecedented challenges. One major consequence of these developments is the significant increase in waste production (Çelik et al. 2024; Şengel et al. 2022; Canbaz et al. 2021). The utilization of waste materials in concrete structures plays a critical role in promoting environmental sustainability and supporting recycling efforts (Bulut 2024; Karalar and Çavuşlu 2022). Agricultural waste is contingent upon the nature of the agricultural activities undertaken, which can be generated from crop residues in the field, or from agro-based industries (Bekem Kara 2024). After the harvest and consumption of some agricultural products such as corn, peanuts, sugar cane; wastes such as corn cobs, peanut shells and sugar cane pulp are generated (Raheem and Ikotun 2020). Safe disposal of agricultural wastes is an important issue in terms of reducing the volume of waste and eliminating storage problems and costs, as well as preventing environmental pollution. In recent years, it has been ascertained that the use of these wastes in cementitious composites can be beneficial both economically and ecologically.

Studies on agricultural wastes point that the agricultural product that leaves the most residues is rice. The annual production of rice worldwide is 600 million tons (Younes et al. 2018). While only 17% of this amount is used, it is known that 83% is rice husk waste. Burning rice husk in open areas for disposal causes soil and water pollution (Khan et al. 2020). In recent years, the most no-

---

* *Corresponding author.* Tel.: +90-466-215-1000 ; E-mail address: ilknurbekem@artvin.edu.tr (İ. Bekem Kara)

ISSN: 2548-0928 / DOI: https://doi.org/10.20528/cjcrl.2025.02.001

table agricultural waste is rice husk ash. It is known that rice husk ash has pozzolanic properties. Rice husk ash, which has a high silica content, is substituted for cement. (Mohseni et al. 2016; Younes et al. 2018; Zahedi et al. 2015).

Morever, studies on the usability of regionally produced agricultural wastes in cementitious composites are available in the literature (Baran et al. 2020; Tekin et al. 2021). One of the agricultural wastes with regional production is tea, which is the most consumed beverage after water. In this context, studies published in recent years are summarized. Anjum et al. (2020) washed the tea wastes they collected with distilled water 4-5 times to separate them from sugar and milk components and used them in brick production by sieving. Jakhrani et al. (2019), on the other hand, collected the tea waste from student cafes and local restaurants in the Seoul area and used it in the production of mortar. Nasr et al. (2019) obtained tea waste ash by burning domestic waste tea at 600 °C and replaced it with cement up to 10% in mortar production. They found that the 7.5% substitution increased the compressive strength compared to the reference. Gupta et al. (2015) named the tea powder obtained after the preparation of home tea as “tea waste” and collected it from the university cafeteria for use in brick production. The common point of the mentioned studies is that the tea wastes used are the residues from the brewed tea. It is troublesome to collect these wastes from various places. In addition, milk, sugar, sweetener, etc. of collected tea wastes must also be removed. It is also known that the quality of teas differs from region to region. In this context, it will not be possible to talk about the same characteristics and homogeneity of domestic tea wastes. Therefore, this study focused on the factories that are the source of tea waste. In Türkiye, where there are 274 tea factories in total, the region that is suitable for tea cultivation in terms of climate is the Eastern Black Sea, and the planted tea areas and the amount of tea produced increase every year. Tea production map of Türkiye is seen in Fig. 1.

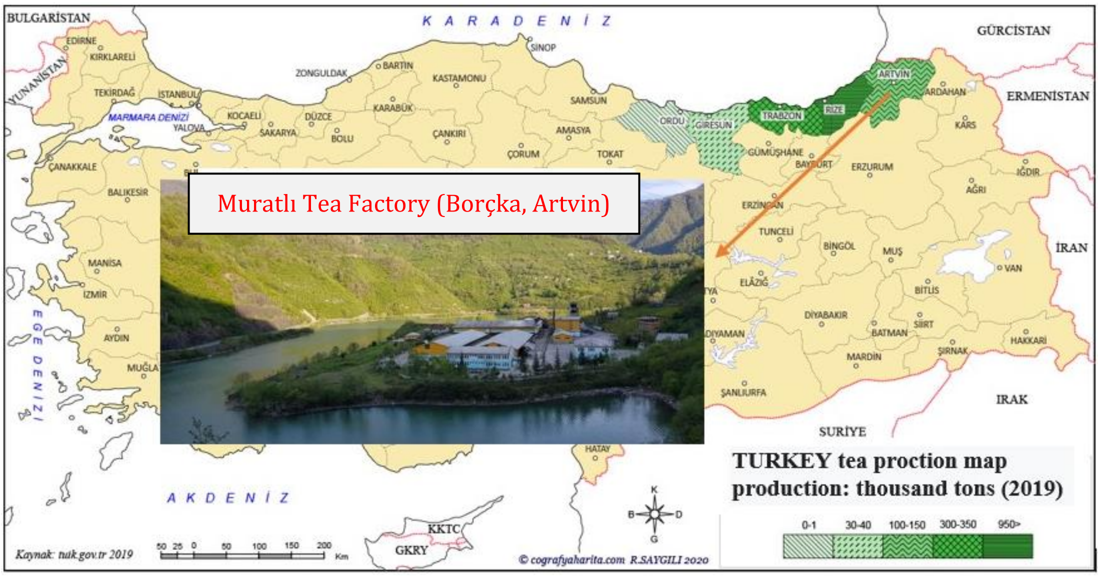

Fig. 1. Tea production amounts in Türkiye, and Muratlı Tea Factory (TEBGE 2024).

The total product obtained annually in the Eastern Black Sea region consists of around 1.5 million tons of fresh tea, so approximately 650 thousand tons of tea waste is generated every year (BEPA 2024). The collection of waste tea fibers in a closed volume creates storage problems and additional costs. Kara (2018) concluded that tea waste can be used as natural fiber up to 7 kg in 1 m^3 of concrete, but it would be appropriate to use it up to 5 kg in places that will be exposed to abrasion (Kara 2018). One of the methods of destroying waste tea fibers is incineration. However, burning this waste together with coal does not provide the limit values specified in the Regulation on Control of Industrial Air Pollution. In this context, it is more advantageous to burn waste tea fibers in a separate incineration unit (RTB 2013). Terzi et al. (2025) used tea ash together with blast furnace slag. Tea ash was substituted for cement at rates of 1.25%, 2.5%, 3.75%, 5%, 7.5% and 10%. Tea ash used with blast furnace slag exhibited lower strength than the control sample on days 2, 7, 28, and 90. As far as the author knows, the waste tea fibers obtained from the factory in the production of cement composites have not been turned into ashes and replaced with cement until now. In this regard, the potentiality of ash obtained from the incineration of tea waste to usability in cement systems is investigated in the present study.

2. Materials and Method

In this study, CEM I 42.5 R Portland cement (PC), $Ca(OH)_2$, tea waste and water were used. Cement was obtained Oyak Cement Plant (Ordu, Türkiye). The cement’s specific surface area was 3,316 cm^2/g, its specific gravity was 3.13 g/cm^3. Chemical properties of PC is given in Table 1.

Table 1. Chemical properties of cement.

Oxide	CaO	Al_2O_3	Fe_2O_3	SiO_2	SO_3	MgO	Na_2O	Loss of ignition	Insoluble matter
Value (%)	62.64	4.56	3.36	19.05	2.88	2.98	0.15	3.02	0.30

2.1. Preparation of TWA

Tea wastes taken from Muratlı Tea Plant (Artvin, Türkiye) storage area were first dried at 100±5 °C. According to Tekin et al. (2021) The incineration of agricultural wastes plays a crucial role in reducing their volume, enabling relevant industries to utilize smaller land areas and incur lower disposal costs (Tekin et al. 2021) . Then the tea waste was exposed to 850 °C for three hours and coded as TWA (Fig. 2). Upon reviewing the literature, it was observed that tea waste was burned at 600-700 °C. However, the loss of ignition values of the ash obtained in these studies are on average 13%. To minimize the loss of ignition, the temperature was increased in this study (Nasr et al. 2019; Terzi et al. 2025). No grinding process was performed on the ash after high temperature. TWA was sieved using a 250-micron sieve. Material passing through the sieve was used.

Fig. 2. Tea waste from tea factory and TWA.

2.2. Characterization of TWA

The elemental composition of TWA was determined using the X-ray fluorescence (XRF) method. Specific gravity and specific surface area were determined using the surface area analysis (BET) method. In addition, the particular size distribution of TWA was determined by laser particle size analyzer (Malvern, model 'Mastersizer Hydro 2000 MU'). Mass losses of TWA at increasing temperatures were determined with the help of thermogravimetric analysis (TG) in Perkin Elmer STA-6000 device. In this study, TG of TWA was performed at 10 °C / min heating rate up to 900 °C. X-Ray diffraction patterns (XRD) of TWA were obtained at room temperature, in Bruker brand Discover-D8 model powder diffractometer system and using copper radiation [$\lambda\ (CuK\alpha)$= 1.54056Å] in the scanning range of 2θ = 5.0–80.0°. SEM was used to investigate morphology of TWA.

2.3. Pozzolanic activity of TWA

The hydraulic property determined in terms of compressive strength with the mortar prepared by mixing ground natural pozzolan, water, $Ca(OH)_2$ and sand is defined as pozzolanic activity (TS 25 2008). The pozzolanic activity of The TWA utilized in the study was assessed in accordance with the TS 25 standard (Table 2).

The prepared mortar sample was poured into 40×40×160 mm^3 sized molds (Fig. 3). It was demoulded the next day and kept at 55±2 °C for 6 days.

2.4. Preparation of blended cement pastes with TWA

In this study, reference cement paste (M1) was prepared with 100% Portland cement. In addition, 2, 4, 6, 8, and 10% TWA was replaced by cement by weight. Thus, five different blended cement pastes were produced according to TS EN 196-3 (2017) standard. Blended cement pastes were labelled M2, M3, M4, M5 and M6.

Fig. 3. Mortar samples for pozzolanic activity.

Table 2. Amount of materials for pozzolanic activity.

Materials	TWA	TS 25
$Ca(OH)_2$	150 g	150 g
Pozzolan	218.30 g	T= 2x150x (density of pozzolan/ density of $Ca(OH)_2$)
Standard aggregate	1,350 g	1,350 g
Water	184.15+90=274.15	0.5x (150+T)

2.5. Preparation of blended cement pastes with TWA

In this study, reference cement paste (M1) was prepared with 100% Portland cement. In addition, 2, 4, 6, 8, and 10% TWA was replaced by cement by weight. Thus, five different blended cement pastes were produced according to TS EN 196-3 (2017) standard. Blended cement pastes were labelled M2, M3, M4, M5 and M6.

2.6. Experimental methods

The compressive strength of the mixture prepared for pozzolanic activity was measured on the 7th day in accordance with TS EN 196-1 (2016) standard. The standard consistency water and setting times of the produced cement pastes were determined with the Vicat device. The volume expansion of the mixtures was found with the Le Chatelier mold. The setting times were performed in accordance with the TS EN 196-3 (2017) standard, with the ambient temperature being 20±2 °C and the mixing water temperature being 20±2 °C, under experimental conditions. The volume expansion that may occur in the cement paste with the Le Chatelier mold was determined in accordance with the TS EN 196-3 (2017) standard.

3. Results and Discussion

3.1. Characterization of TWA

Specific gravity of TWA was 1.63 g/cm^3, and the specific surface area (BET) was 11,810 cm^2/g. Cumulative particle size distribution of TWA is seen in Fig. 4. The high peak was in the 10–100 µm range. There are two smaller peaks below 1 µm and above 100 µm. In addition, d90, d50 and d10 values of TWA were 54.52 µm, 12.663 µm, and 2.400 µm, respectively. It was seen that PC has more homogeneous distribution than TWA. d90, d50 and d10 values of PC were 46.265 µm, 15.404 µm, and 2.605 µm, respectively.

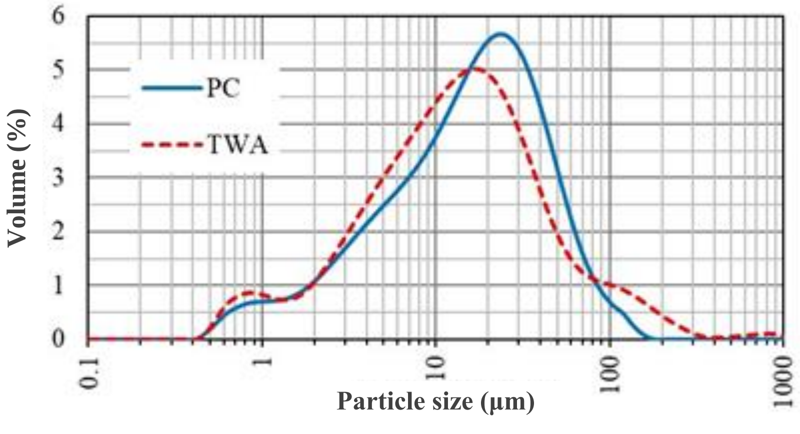

Fig. 4. Cumulative particle size distribution of TWA.

The chemical compositions of PC, TWA and blended cements are shown in Table 3. The chemical components of the blended cements were theoretically calculated according to the replacement amount of TWA with cement. Values were evaluated according to some TS EN 197-1 (2012) limitations. When the chemical compositions of TWA were examined, it was established that the SO_3, MgO and glow loss amounts were above the limit value required by the standard. However, it was observed that the SO_3, MgO and glow loss amounts of the cements blended with up to 10% TWA substitute used in this study did not exceed the standard value. The limit value of Cl^- for all cements is 0.1% (TS EN 197-1 2012). When the oxides of the blended cements are calculated theoretically, up to 4% TWA substitution provides a limit value.

However, in 6, 8 and 10% replacements, the Cl^- limit value is exceeded, which may cause rebar corrosion for reinforced concrete. The alkali content depends on the amount of K_2O and Na_2O in the cement (Zhang 2011). Alkalines, a minor but inevitable component of PC clinker, originate from the raw materials used in cement production. Owing to variations in the composition of raw materials, the alkali content in cement produced by different factories shows significant differences across various regions (Huang and Yan 2019). When the alkali presence of TWA is examined, it is observed that its main component is K_2O (31.31%). Due to the high alkali content of TWA and low content of SiO_2+Fe_2O_3+Al_2O_3, the alkali content of the blended cement increased significantly with the increase of TWA substitution. The total alkali content (%) for M1, M2, M3, M4, M5 and M6 mixtures was calculated as 0.88, 1.28, 1.67, 2.07, 2.47 and 2.86, respectively.

Table 3. Chemical properties of blended cements.

Oxide (%)	TWA	M1 (OPC)	M2	M3	M4	M5	M6
CaO	13.95	63.10	62.12	61.13	60.15	59.17	58.19
SiO_2	3.13	19.56	19.23	18.90	18.57	18.25	17.92
Al_2O_3	8.24	4.41	4.49	4.56	4.64	4.72	4.79
Fe_2O_3	1.18	3.16	3.12	3.08	3.04	3.00	2.96
K_2O	31.31	0.79	1.40	2.01	2.62	3.23	3.84
Na_2O	0.10	0.36	0.35	0.35	0.34	0.34	0.33
P_2O_5	8.24	–	0.16	0.33	0.49	0.66	0.82
MnO	3.90	–	0.08	0.16	0.23	0.31	0.39
SO_3	5.64	2.99	3.04	3.10	3.15	3.20	3.26
MgO	5.42	2.36	2.42	2.48	2.54	2.60	2.67
Cl^-	1.57	0.02	0.05	0.08	0.11	0.14	0.18
Loss of ignition (LOI)	9.47	2.70	2.84	2.97	3.11	3.24	3.38

Mass loss values of TWA at increasing temperatures are presented in Fig. 5. According to the DTG curves, endothermic peaks formed for TWA under 100 °C indicate that the adsorbed water in the material structure evaporates. The second endothermic peak, occurring at around 600 °C, is believed to signify the loss of water that is more strongly bonded to the structure. It was found that the total mass loss of TWA at 900 °C amounted to 7.61%. In XRD analysis, 77% of TWA was found to be crystalline and 23% amorphous. Sylvite is potassium chloride in natural mineral form (Fig. 6). It is known from the literature that crystalline materials do not exhibit pozzolanic properties (Bekem Kara 2022; Erdem et al. 2007). When the diffraction patterns are examined, it is seen that all minerals are of potassium origin. This situation is parallel to K_2O, which emerged as the main component in the XRF analysis. When the TWA image was magnified 5000X, it was found to have a needle-like structure (Fig. 7). This situation is attributed to the presence of K_2O, which has a high content in TWA. In addition, the acicular image supports the high specific surface area (11,810 cm^2/g) determined by BET.

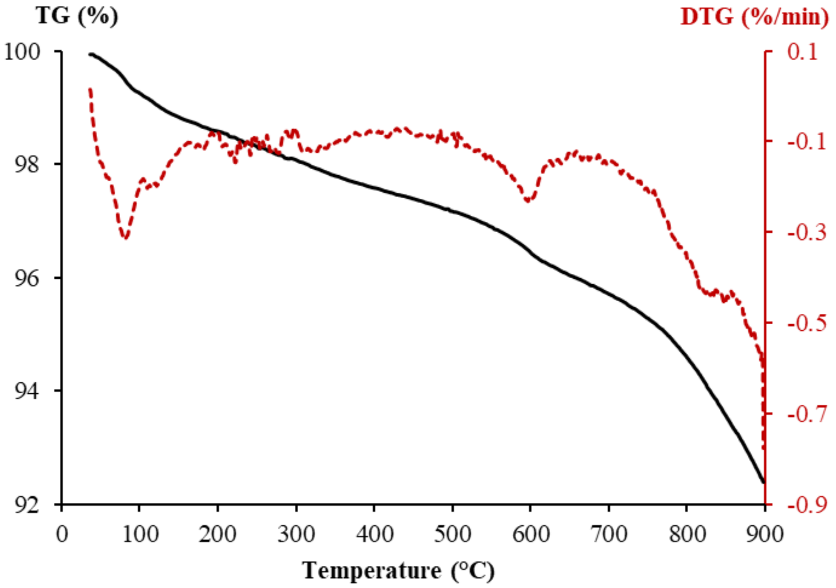

Fig. 5. TG-DTG analysis of TWA.

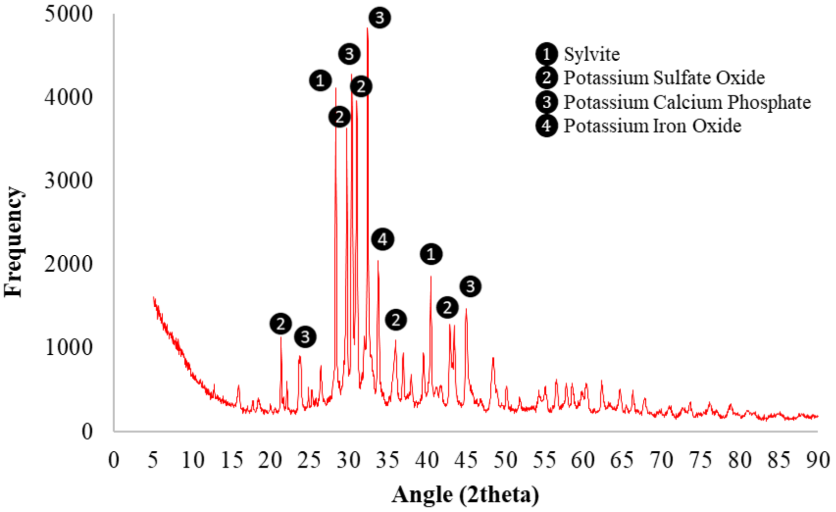

Fig. 6. Diffraction patterns of TWA.

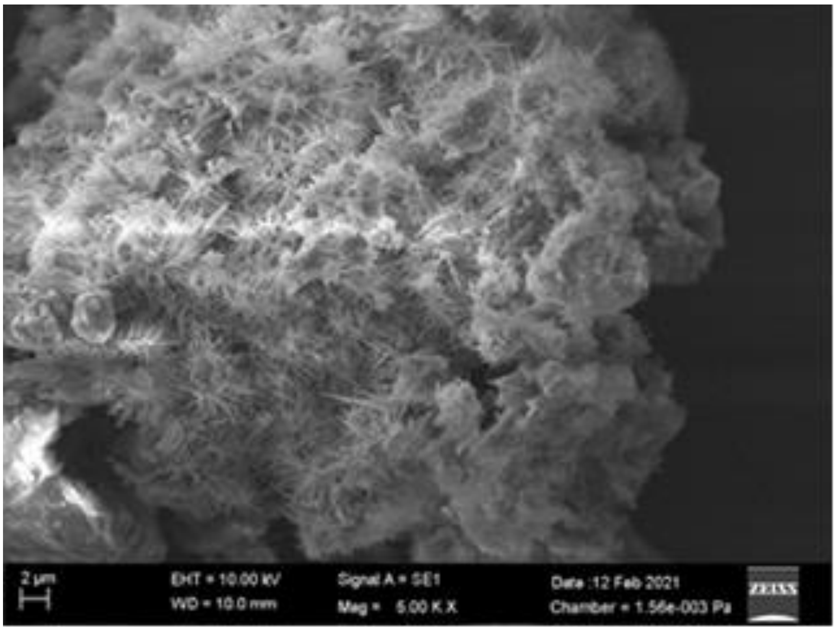

Fig. 7. SEM image of TWA (x5000).

3.2. Pozzolanic activity of TWA

As a result of the pozzolanic activity test, the compressive strength of the TWA substituted mortars was obtained as 2.20 MPa on the 7th day. In this context, the waste ash material does not show pozzolanic properties. This result supports each other with XRD diffraction patterns, which is one of the characterization features.

3.3. Standard consistency water of blended cement pastes

The amount of water determined for the standard consistency of cement pastes produced with TWA is presented in Fig. 8. The amount of water required for standard consistency of blended cement pastes increased significantly with TWA substitution. While 2% TWA substitution increased the consistency water requirement by 14.07%, 10% TWA substitution increased the consistency water requirement by 71.36%. The fact that the specific surface area of TWA is greater than that of cement can be explained as the reason for the increased water requirement with the increase in the replacement ratio. As ashes are hygroscopic in nature (Ganesan et al. 2007) and the specific surface area of TWA is three times higher than cement it needs more water for proper consistency. Tekin et al. (2021) found that the amount of water required for consistency increased as the substitution rate increased in the cement pastes they produced with pistachio shell ash substitution. In another study, an increase in water requirement was observed with the use of hazelnut shell ash (Baran et al. 2020). This situation was explained in the literature by the increase in total surface area after modification with ash particles that are finer than cement. Furthermore, it has been noted that irregular shapes and pores contribute to an increased water requirement (Garcés et al. 2008).

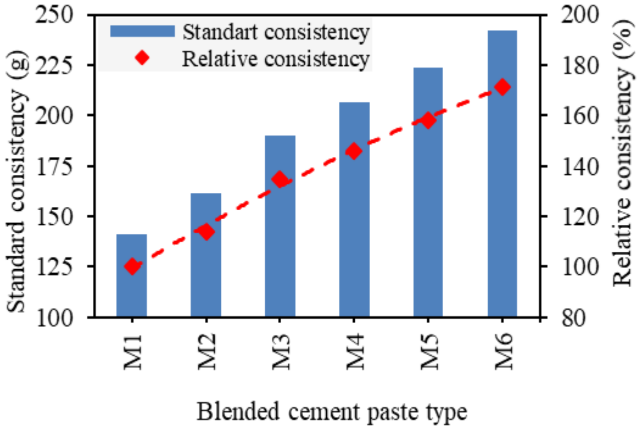

Fig. 8. Standard consistency water of the blended cements.

3.4. Setting time of blended cement pastes

Initial and final setting times of the mixtures are shown in Fig. 9. It is seen that the setting times decrease as the amount of TWA increases. While the initial setting time was 230 min. in the M1, it was measured as 215, 195, 130, 80 and 45 min. with 2, 4, 6, 8 and 10% TWA substitution, respectively. It is observed that the initial setting decreased by 80.43% compared to the reference sample when the TWA substitution was 10%. Therefore, it is thought that TWA can be used as a setting accelerator additive in addition to its other properties explained in more detail in this study. It is known that the alkalis (Na_2O and K_2O) in TWA are higher than cement, which has an effect on the setting time. Because alkalis accelerate the setting of cement-based materials (Jawed and Skalny 1978). It is seen in Table 3 that there is an increase in the K_20 amounts of cement pastes with TWA substitution. While the K_20 amount in the theoretical chemical composition of M1 is 0.79%, the K_20 amount of M6 was calculated as 3.84% with 10% TWA substitution. As a result of the detected changes, the conformity value of the initial setting time is specified as 60 minutes and above in the relevant standard (TS EN 197-1 2012). Except for the M6 mix, all of the mixes were found to have a set onset time above the specified value (Fig. 6).

When the final setting times are examined, the final setting accelerating effect of TWA is again seen. The final setting times of the samples with 0, 2, 4, 6, 8 and 10% TWA substitution were measured as 270, 260, 235, 175, 120 and 75 minutes, respectively. With the use of 10% TWA, the final setting time decreased by 72.22% compared to the reference. There is no value for the final setting time in the relevant standard (TS EN 197-1 2012).

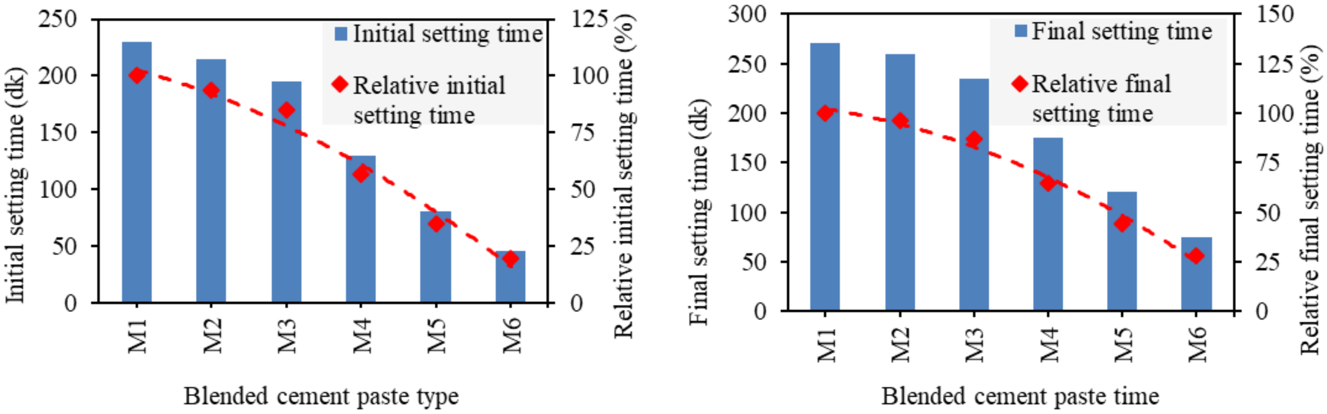

Fig. 9. Initial and final setting time values of the blended cements.

3.5. Volume expansion of blended cement pastes

The amount of possible expansion that may occur as a result of the reaction of free CaO and MgO in TWA-substituted cement samples with water should be below 10 mm according to the TS EN 197–1 (2012) standard.

As a result of the study, it was observed that the expansion values did not exceed the limit value as seen from Table 4. While the expansion amount of the M1 sample is 1 mm, it is seen that the expansion amount is 3 mm in the M6 sample with 10% TWA substitution. The increase in MgO ratios in the theoretically calculated chemical analyzes of the mixtures formed with TWA is given in Table 3.

In the theoretical calculation, the MgO ratio in the M1 mixture is 2.36%, while the MgO ratio in the M6 mixture is 2.67%. Therefore, it is possible to explain the increase in volume expansion with the increase in the MgO ratio that reacts. This circumstance aligns with the existing literature (Bekem Kara 2022).

Table 4. Chemical properties of cement.

Mix ID	M1 (OPC)	M2	M3	M4	M5	M6
Expansion (mm)	1.0	1.0	1.0	1.5	2.0	3.0

4. Conclusions

Studies on the recyclability of agricultural wastes in cementitious systems have attracted attention in recent years. In this study, tea waste ash was characterized in detail and the properties of cement pastes blended with tea waste ash were investigated. In accordance with the experimental findings, the following results were obtained:

- Tea waste ash is of potassium origin, mostly in crystalline form. The specific surface area is quite high due to the needle-like structure obtained in SEM image. The main component of ash in chemical composition is K_2O.
- Tea waste ash substitution has increased standard consistency water of blended cement pastes. 10% tea waste ash reduces the initial setting time by up to 80.43% and the final setting time by up to 72.20%. Ash substitution up to 8% provided the initial setting time included in the standard. It is thought that tea waste ash can be used as a setting accelerator additive in cement systems, even in small amounts, due to its high K_2O content.

Waste tea fibers are one of the agricultural wastes that need to be disposed of in tea production areas. It is thought that the use of these wastes, which is an important issue for the Eastern Black Sea Region where tea farming and tea factories are located in Türkiye, is an important issue. It is recommended to investigate the strength, thermal and durability performance properties of mortars and concretes with tea waste ash substitute. In addition, tea waste ash can be used in geopolymer production due to their high alkali content.

Acknowledgements

None declared.

Funding

This research was supported by the Artvin Çoruh University Scientific Research Projects Fund under grant number 2020.F94F02F01.

Conflict of Interest

The authors declared no potential conflicts of interest with respect to the research, authorship, and/or publication of this manuscript.

Author Contributions

All of the authors made substantial contributions to conception and design, or acquisition of data, or analysis and interpretation of data; were involved in drafting the manuscript or revising it critically for important intellectual content; and gave final approval of the version to be published.

Data Availability

The datasets created and/or analyzed during the current study are not publicly available, but are available from the corresponding author upon reasonable request.

REFERENCES

Anjum F, Naz MY, Ghaffar A, Shukrullah S, AbdEl-Salam NM, Ibrahim KA (2020). Study of thermal and mechanical traits of organic waste incorporated fired clay porous material. *Physica B: Condensed Matter*, 599, 412479.

Baran Y, Gökçe HS, Durmaz M (2020). Physical and mechanical properties of cement containing regional hazelnut shell ash wastes. *Journal of Cleaner Production*, 259, 120965.

Bekem Kara I (2022). Characterization, pozzolanic activity of natural pileki and calcined pileki and effect to mechanic properties of cement mortars. *Journal of the Faculty of Engineering and Architecture of Gazi University*, 37(1), 555–569.

Bekem Kara I (2024). Use of agricultural waste ashes in concrete production. In I. Bekem Kara (Ed.), *Advanced Research in Civil Engineering*, Yaz Yayınları.

BEPA (2024). Directorate General of Energy Affairs. Ankara, Türkiye. https://bepa.enerji.gov.tr/

Bulut H (2024). A different approach for green concrete production: Determination of the effect of e-waste and waste rubber powder on durability properties of concrete. *Challenge Journal of Concrete Research Letters*, 15(3), 69-81.

Canbaz M, Kara İ, Topçu İ (2021). Effect of high temperature on the mechanical behavior of cement-bonded wood composite produced with wood waste. *Challenge Journal of Structural Mechanics*, 7(1), 42-48.

Çelik Z, Turan E, Oltulu M, Öner G (2024). Reinforcement of concrete beams using waste carbon-nanoclay-fiberglass laminate pieces. *Challenge Journal of Concrete Research Letters*, 15(1), 1-6.

Erdem TK, Meral Ç, Tokyay M, Erdoğan TY (2007). Use of perlite as a pozzolanic addition in producing blended cements. *Cement and Concrete Composites*, 29(1), 13–21.

Ganesan K, Rajagopal K, Thangavel K (2007). Evaluation of bagasse ash as supplementary cementitious material. *Cement and Concrete Composites*, 29(6), 515–524.

Garcés P, Pérez Carrión M, García-Alcocel E, Payá J, Monzó J, Borrachero MV (2008). Mechanical and physical properties of cement blended with sewage sludge ash. *Waste Management*, 28(12), 2495–2502.

Gupta P, Attri R, Kumar R (2015). Utilisation of WTP sludge & tea waste in brick manufacturing. *International Journal of Advanced Technology in Engineering and Science*, 3(1), 1663–1670.

Huang L, Yan P (2019). Effect of alkali content in cement on its hydration kinetics and mechanical properties. *Construction and Building Materials*, 228, 116833.

Jakhrani SH, Ryou JS, Atta-ur-Rehman, Jeon IK, Woo BH, Kim HG (2019). Prevention of autogenous shrinkage in high-strength mortars with saturated tea waste particles. *Materials*, 12(17), 2654.

Jawed I, Skalny J (1978). Alkalies in cement: A review: II. Effects of alkalies on hydration and performance of Portland cement. *Cement and Concrete Research*, 8(1), 37–51.

Kara C (2018). Usability of tea waste in concrete as natural fiber. *Journal of Natural Hazards and Environment*, 4(2), 156–165.

Karalar M, Çavuşlu M (2022). Evaluating effects of granulated glass on structural and seismic behavior of tall RC structures using experimental tests and 3D modeling. *Challenge Journal of Structural Mechanics*, 8(2), 63-77.

Khan K, Ullah MF, Shahzada K, Amin MN, Bibi T, Wahab N, Aljaafari A. (2020). Effective use of micro-silica extracted from rice husk ash for the production of high-performance and sustainable cement mortar. *Construction and Building Materials*, 258, 119589.

Mohseni E, Naseri F, Amjadi R, Khotbehsara MM, Ranjbar MM (2016). Microstructure and durability properties of cement mortars containing nano-TiO_2 and rice husk ash. *Construction and Building Materials*, 114, 656–664.

Nasr SS, Hasan ZA, Abed MK (2019). Mechanical properties Of cement mortar made with black tea waste ash as a partial replacement of cement. *Engineering and Technology Journal*, 37(1), 45–48.

Raheem AA, Ikotun BD (2020). Incorporation of agricultural residues as partial substitution for cement in concrete and mortar – A review. *Journal of Building Engineering*, 31, 101428.

RTB (2013). Private Sector Tea Factories General Environmental Assessment Report. Rize Mercantile Exchange, Rize, Türkiye.

Şengel H, Kınık K, Erol H, Canbaz M (2022a). Effect of waste steel tire wired concrete on the mechanical behavior under impact loading. *Challenge Journal of Structural Mechanics*, 8(4), 150-158.

TEBGE (2024). Tea Product Report 2024. Agricultural Economic and Policy Development Institute, Republic of Türkiye Ministry of Agriculture and Forestry, Ankara, Türkiye.

Tekin İ, Dirikolu İ, Gökçe HS (2021). A regional supplementary cementitious material for the cement industry: Pistachio shell ash. *Journal of Cleaner Production*, 285, 124810.

Terzi C, Kutuk S, Kutuk-Sert T (2025). Influence of processed tea waste ash on the hydration products and mechanical property of hybrid cement as an eco-friendly solution. *Waste Management*, 191, 242–252.

TS 25 (2008). Natural pozzolan (trass) for use in cement and concrete - Definitions, requirements and conformity criteria. Turkish Standards Institute, Ankara, Türkiye.

TS EN 196-1 (2016). Methods of testing cement - Part 1: Determination of strength. Turkish Standards Institute, Ankara, Türkiye.

TS EN 196-3 (2017). Methods of testing cement - Part 3: Determination of setting times and soundness. Turkish Standards Institute, Ankara, Türkiye.

TS EN 197-1 (2012). Cement - Part 1: Composition, specifications and conformity criteria for common cements. Turkish Standards Institute, Ankara, Türkiye.

Younes MM, Abdel-Rahman HA, Khattab MM (2018). Utilization of rice husk ash and waste glass in the production of ternary blended cement mortar composites. *Journal of Building Engineering*, 20, 42–50.

Zahedi M, Ramezanianpour AA, Ramezanianpour AM (2015). Evaluation of the mechanical properties and durability of cement mortars containing nanosilica and rice husk ash under chloride ion penetration. *Construction and Building Materials*, 78, 354–361.

Zhang H (2011). Building Materials in Civil Engineering. 1st ed., Woodhead Publishing.

Research Article

Performance evaluation of compressive strength of concrete using different machine learning algorithms

Supriya Siddharth More [a,*], Ajaykumar R. Kambekar [a]

[a] *Department of Civil Engineering, Sardar Patel College of Engineering, Andheri West ,400058 Maharashtra, India*

ABSTRACT

Accurately predicting the compressive strength of concrete is crucial for ensuring structural integrity, optimizing material usage, and reducing construction costs. Conventional experimental methods, though reliable, are often labour-intensive and time-consuming. To address these limitations, this study investigates the effectiveness of machine learning (ML) algorithms as efficient alternatives for predicting concrete compressive strength. Four ML algorithms—Linear Regression (LR), Multilayer Perceptron (MLP), M5 Rule-Based Model, and Support Vector Machines (SVM)—were evaluated based on their predictive performance. A comprehensive dataset comprising 350 concrete samples was prepared, with compressive strength tests conducted in accordance with Indian standard 516. The models were trained on experimental data and were tested using varying data splits of 50%, 40%, 30%, 20%, and 10% to assess their prediction accuracy. Among the evaluated models, the MLP demonstrated superior performance, achieving a correlation coefficient (CC) of 0.98 with a 20% testing split, outperforming the other algorithms. To further validate the predictive capability of the MLP model, multiple linear regression analysis was employed, confirming its robustness and generalization ability. The findings underscore the potential of machine learning techniques, particularly the MLP model, in providing accurate, reliable, and time-efficient predictions of concrete compressive strength. This study contributes to the growing body of research focused on leveraging machine learning for enhanced decision-making in construction material design, ultimately promoting more sustainable and cost-effective construction practices.

ARTICLE INFO

Article history:
Received – January 20, 2025
Revision requested – February 18, 2025
Revision received – March 11, 2025
Accepted – March 22, 2025

Keywords:
Linear regression
Multilayer perceptron
M5 rule-based model
Support vector machines

Citation: More SS, Kambekar A (2025). Performance evaluation of compressive strength of concrete using different machine learning algorithms. *Challenge Journal of Concrete Research Letters*, 16(2), 60–68.

1. Introduction

The field of construction materials research has undergone a significant transformation with the advent of machine learning (ML) techniques, offering novel approaches for analyzing and predicting the properties of materials. Machine learning enables the development of computational models capable of learning from data and identifying complex patterns, thereby offering potentially more efficient and effective solutions to structural engineering challenges (Gürbüz and Kazaz 2024). Among these properties, compressive strength is a critical parameter that defines the quality, safety, and durability of concrete structures (Nalina 2023). The application of advanced ML algorithms to predict the compressive strength of concrete can significantly accelerate labor-intensive experimental processes and reduce associated costs (Harirchian 2024). Traditional methods for determining compressive strength often involve time-consuming laboratory tests and physical experiments. As construction demands grow and evolve, there is a pressing need for efficient, accurate, and cost-effective methods to predict compressive strength during the design phase. While these methods ensure precision, they

---

* *Corresponding author.* Tel.: +91-96231-47149 ; E-mail address: ssmore74@gmail.com (S. S. More)

ISSN: 2548-0928 / DOI: https://doi.org/10.20528/cjcrl.2025.02.002

are limited by high costs, delays, and constraints in real-time adaptability. In the modern era of construction and infrastructure demands, where rapid urbanization and sustainable design practices are paramount, the need for efficient and accurate methods for predicting compressive strength has become increasingly apparent. Machine learning algorithms present an innovative solution to this challenge by leveraging computational models to establish complex relationships between input features and target variables (Yeh 1998). These techniques can effectively model nonlinear relationships and process large datasets, thereby enhancing prediction accuracy and decision-making in concrete mix design. This study focuses on evaluating the performance of various machine learning algorithms for predicting the compressive strength of concrete.

2. Literature Review

The use of machine learning (ML) algorithms to predict the compressive strength of concrete has gained significant attention in recent years due to their capability to process large datasets and capture nonlinear relationships between multiple input variables. Yeh (1998) was one of the first researchers to model the strength of high-performance concrete using Artificial Neural Networks (ANNs). The study demonstrated that ANNs outperform traditional regression techniques in capturing nonlinear relationships between variables such as water-cement ratio, cement content, and curing time. Chou and Tsai (2012) investigated a combined classifier approach using support vector machines (SVM) and decision trees for concrete compressive strength prediction. The hybrid model was shown to provide enhanced accuracy compared to standalone ML algorithms. Huang et al. (2025) applied deep learning techniques such as convolutional neural networks (CNN) to predict the strength of concrete containing waste materials like glass. Their findings emphasized the importance of dataset size and preprocessing in deep learning applications. Tiep et al. (2024) introduced a novel hyperparameter tuning framework for regression tasks. Their study combined sampling algorithms with neural networks to optimize model performance, achieving higher prediction accuracy for concrete strength. Khan et al. (2025) used Optuna for automated hyperparameter tuning in predicting high-performance concrete strength. By leveraging tools like SHAP for interpretability, they provided insights into influential variables such as cement content and water-cement ratio. Ullah et al. (2025) demonstrated the effectiveness of hybrid ML models combining traditional methods with advanced optimization algorithms to estimate the tensile and compressive strength of basalt fiber-reinforced concrete.

Oyebisi et al. (2024) incorporated optimization techniques in ML models to enhance the prediction accuracy for slurry infiltrated fiber concrete. The study highlighted the need for domain-specific customization in ML applications. Salami et al. (2024) focused on the influence of feature selection in ML models for predicting the compressive strength of concrete. The study demonstrated that proper feature engineering could significantly enhance prediction accuracy. Feature engineering refers to the process of selecting, modifying, or creating relevant input variables (features) that help machine learning (ML) models make accurate predictions. Pan et al. (2025) applied ensemble learning to predict recycled concrete's compressive strength, emphasizing the importance of cleaning datasets and identifying key predictors. Ghoniem and Nour (2025) applied ML models to predict the mechanical properties of sandstone concrete with varying compaction levels and silica fume ratios. Their results demonstrated the adaptability of ML for diverse concrete compositions. Li et al. (2025) investigated the performance of circular concrete-filled steel tubular columns using ML-based strength prediction models, combining traditional mechanics and advanced ML techniques. In this study, Linear Regression serves as a fundamental baseline model for regression tasks. It establishes a linear relationship between input variable and the target variable, which, in this case, is the compressive strength of concrete. Despite its simplicity, LR offers interpretability and provides insights into how individual variable affect strength predictions. Its inclusion ensures a comparative understanding of how more complex models improve upon this baseline. MLP, a type of artificial neural network, is capable of capturing complex, nonlinear relationships within data. Since concrete compressive strength is influenced by multiple interacting factors (e.g., material composition, curing time), MLP can model these nonlinearities effectively. Its robust learning ability allows it to generalize well across different datasets, making it ideal for predicting material properties with inherent variability. The M5 Rule-based model combines decision trees with linear regression, providing both interpretability and predictive power. It creates piecewise linear models that adapt to local patterns in the data, offering a balance between accuracy and explainability. This makes it suitable for complex engineering datasets where relationships between variables may vary across different ranges. SVM is known for its ability to handle high-dimensional data and model nonlinear relationships using kernel functions. For predicting concrete compressive strength, SVM can manage complex interactions between variables with high precision. It is also less prone to overfitting, especially in scenarios where the dataset is not large, ensuring robust predictions.

This study contributes to the existing body of work on concrete strength prediction by providing a comprehensive comparison of different machine learning models, including MLP, SVR, M5 Rule, and Linear Regression. Unlike previous studies that focused on single-model applications, this research highlights the strengths and limitations of each model under varying training-to-testing data splits. The findings emphasize the importance of selecting an appropriate ML model and training percentage to achieve reliable predictions, reducing the reliance on extensive laboratory testing. Furthermore, this study demonstrates that MLP outperforms traditional and rule-based models, reinforcing the need for advanced ML techniques in concrete durability assessment and predictive analytics.

2.1. Linear regression model

Linear regression is a fundamental statistical and machine learning algorithm used to model the relationship between one dependent variable (y) and one or more independent variables ($x_1, x_2, .., x_n$) (Aydın et al. 2024; Öztaş et al. 2005). The model assumes a linear relationship between the variables and predicts the value of (y) based on the given inputs. In simple linear regression, there is only one independent variable (x). The relationship is modeled in Eq. (1) as:

$$y = \beta_0 + \beta_{1x} + \epsilon \tag{1}$$

where:
y is the dependent variable (target);
x is the independent variable (predictor);
β_0 is the intercept (value of y when x=0);
β_1 is the slope coefficient (rate of change of y with respect to x);
ϵ is the error term (accounts for deviations of actual y from predicted y).

While in multiple linear regression, there are n independent variables ($x_1, x_2, .., x_n$). The relationship is modeled as in Eq. (2).

$$y = \beta_0 + \beta_{1x_1} + \beta_{2x_2} + \cdots + \beta_{nx_n} + \epsilon \tag{2}$$

2.2. Multi-layer perceptron model

A Multilayer Perceptron (MLP) is a class of artificial neural networks (ANN) designed for supervised learning tasks such as classification and regression. MLPs are capable of learning complex nonlinear relationships between inputs and outputs, making them highly versatile in a variety of applications, including image recognition, language processing, and predictive modeling. It consists of three main layers: the input layer, hidden layers, and the output layer. The input layer received the input feature while the hidden layer apply transformation using weighted sums and activation functions and the output layer produces the predictions. Forward propagation and backpropagation are two key processes in training artificial neural networks like the Multilayer Perceptron (MLP). They work together to ensure that the network learns from data, minimizes errors, and adjusts its weights and biases effectively. Forward propagation computes the output of the network given the inputs, by passing data through each layer (Topçu and Sarıdemir 2008). The input feature ($x_1, x_2, .., x_n$) are fed into the network. Each neuron computes a weighted sum of its inputs, adds a bias, and applies an activation function as mentioned in Eq. (3).

$$z_j = \sum_{i=1}^{n} w_{ij}\, x_i\, b_j \qquad a_j = f(z_j) \tag{3}$$

where:
w_{ij} is the weight connecting input i to neuron j;
b_j is the bias for neuron j;
$f(z_j)$ is the activation function (e.g., ReLU, Sigmoid, Tanh).

The output layer applies the same process and generates predictions ($\hat{y}$) based on the activations of the previous layer. Backpropagation updates the weights and biases of the network to minimize the error between predicted ($\hat{y}$) and actual (y) values. Use a loss function (e.g., Mean Squared Error or Cross-Entropy Loss) to calculate the error as mentioned in Eq. (4).

$$\text{Loss} = \frac{1}{n} \sum_{i=1}^{n} (y_i - \hat{y}_i)^2 \tag{4}$$

Backpropagation calculates the gradient of the loss function with respect to each weight and bias using the chain rule of calculus as mentioned in Eq. (5).

$$\frac{\partial \text{Loss}}{\partial w_{ij}} \tag{5}$$

Gradients represent how much the weights/biases need to change to reduce the loss. Using gradient descent, update the parameters to minimize the loss as mentioned in Eq. (6).

$$w_{ij} \leftarrow w_{ij} - \eta \frac{\partial \text{Loss}}{\partial w_{ij}} \tag{6}$$

where:
η is the learning rate (step size for updates).

Gradients are propagated backward through the network, layer by layer, starting from the output layer and moving toward the input layer.

2.3. M5 rule model

The M5 Rule Model is a decision-tree-based algorithm used for regression tasks (Quinlan 1992). It combines aspects of decision trees with linear regression models to create a hybrid approach. Developed by Quinlan in 1992, the M5 algorithm is particularly effective for modeling nonlinear relationships and handling large datasets with continuous target variables. M5 constructs a decision tree by recursively splitting the data based on feature values to minimize error. Unlike traditional decision trees that predict constant values at the leaves, M5 associates each leaf node with a linear regression model, allowing for better predictions. The algorithm selects the feature and split point that minimizes the variance of the target variable within each subset. Variance reduction is calculated as mentioned in Eq. (7).

$$\Delta T = \text{var}(T) - \left(\frac{|T_1|}{|T|}\text{var}(T_1) + \frac{|T_2|}{|T|}\text{var}(T_2)\right) \tag{7}$$

where:
T is the original dataset;
T_1, T_2 are the subsets after split;
$|T|$ is the number of samples in T.

At each leaf node, M5 fits a linear regression model as mentioned in Eq. (8).

$$y = \beta_0 + \beta_{1x_1} + \beta_{2x_2} + \cdots + \beta_{nx_n} + \epsilon \tag{8}$$

This allows the model to generalize better and capture trends in the data (Witten and Frank 2005).

2.4. Support vector machine model

Support Vector Machine (SVM) is a powerful supervised learning algorithm used for classification, regression, and outlier detection tasks. It works by finding the optimal hyperplane that separates data points into distinct classes or predicts continuous values in the case of regression (Vapnik 1995).

The hyperplane is expressed as mentioned in Eq. (9).

$$w^T x + b = 0 \tag{9}$$

where:
w is the weight vector;
x is the input feature vector;
b is the bias term.

SVM maximizes the margin (M) between support vectors while ensuring correct classification as mentioned in Eq. (10).

$$M = \frac{2}{\|w\|} \tag{10}$$

The optimization problem is to maximize this margin, which is equivalent to minimizing $\|w\|$ subject to the condition that all data points are correctly classified as mentioned in Eq. (11).

Constraints:

$$y_i(w^T x_i + b) \geq 1, \forall i \tag{11}$$

where:
y_i is the class label of the i-th data point (+1 or −1);
x_i is the feature vector of the i-th data point.

To solve the optimization problem, SVM uses Lagrange multipliers (Smola and Schölkopf 2004).

The Lagrangian formulation for the primal problem as mentioned in Eq. (12).

$$L(w, b, \alpha) = 21\|w\|2 - i = 1\sum n\alpha_i \quad [y_i(w^T x_i + b) - 1] \tag{12}$$

3. Methodology

In this study, concrete mix was prepared using IS 10262 (2019) code. Total 350 number of cubes of dimension 150mm×150mm×150 mm were casted with different mix design and were cured at 27±2 °C for 28 days. The specimens were tested at 7 and 28 days for compressive strength of concrete. The mix ingredients consist of cement, flyash, Alco-fine, ground granulated blast furnace slag, water, fine aggregates and coarse aggregates and admixture as mentioned in Table 1.

Table 1. Mix design proportions.

Component	Dataset of concrete mix		
	min (kg/m^3)	max (kg/m^3)	average (kg/m^3)
Cement	130	650	330
GGBS	0	325	74
Flyash	0	360	59
Alco- fine	0	65	5
20mm	438	745	663
10mm	220	510	349
CRF	530	1100	836
Water	140	180	155
Admixture	1.017	8.45	5.24
Compressive strength (MPa)	12.99	96.73	48.34

For machine learning, WEKA software version 3.8.6 was used. A total of 350 datasets were taken as input. The input dataset consists of cement, GGBS, flyash, Alcofine, 20mm, 10mm Crush sand, admixture. While the output dataset consists of compressive strength .The input and output dataset was normalized and then the dataset was trained and tested with different percentages as 50%, 40%, 30% 20% and 10% with different machine learning algorithms using WEKA software version 3.8.6. The denormalization of output dataset was done to revert back the predictions to their original scale. Statistical parameters such as coefficients of correlation (CC), coefficients of determinations (R^2), mean square error (MSE), mean absolute error (MAE) and root mean square error (RMSE) are evaluated for each machine learning model. Later Multi-linear regression equation for parameters compressive strength was developed from origin software. The statistical parameters developed were compared with multi linear regression and machine learning model statistics.

For MLP model, Sigmoid function was used with epoch 500, learning rate 0.25 and hidden layer 8. The training algorithm used is backward propagation. In Support Vector Regression (SVR), the key hyperparameters include epsilon range 0.001 while alpha ranges from 0.25 and kernel parameters.

4. Results and Discussion

This section presents the performance of the different machine learning model for predicting compressive strength, evaluated across varying training-to-testing data splits. Metrics such as Correlation Coefficient (CC), Coefficient of Determination (R^2), Mean Absolute Error (MAE), Mean Squared Error (MSE), and Root Mean Squared Error (RMSE) were analyzed to assess the model's accuracy and reliability. The compressive strength of concrete is influenced by various factors, such as water-cement ratio, cement content, aggregate properties, and curing conditions. These factors introduce inherent variability in the dataset, which the model attempts to capture.

4.1. Linear regression model

The CC values ranged from 0.95 to 0.97, indicating a strong linear relationship between predicted and actual compressive strengths as mentioned in Table 2. The predicted values of compressive strength and actual values of compressive strength using linear regression model are mentioned in Fig. 1.

Table 2. Linear regression model performance.

Strength	Testing				
	50%	40%	30%	20%	10%
CC	0.95	0.95	0.95	0.96	0.97
R^2	0.91	0.90	0.90	0.92	0.93
MAE (MPa)	4.98	5.08	4.96	4.26	3.86
MSE (MPa)	39.04	41.94	42.53	29.05	24.63
RMSE (MPa)	6.25	6.48	6.52	5.39	4.96

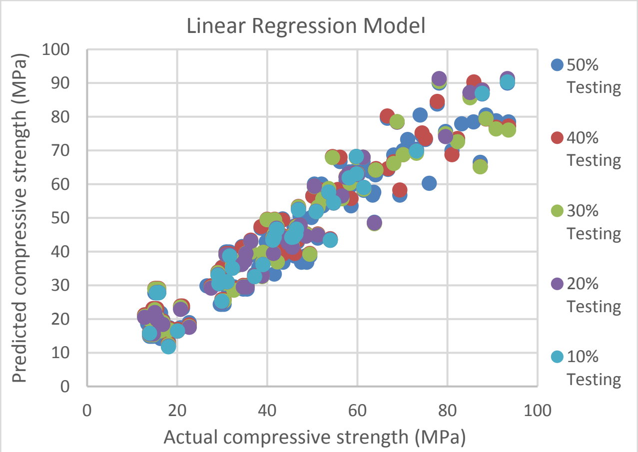

Fig. 1. Linear model prediction efficiency.

Higher training percentages led to slight improvements in CC, with the highest value (0.97), observed at 90% training data. This suggests that linear regression effectively captures the dominant linear trends in the dataset. The reduction in MAE and RMSE as training data increases reflects the model's improved ability to minimize absolute and squared errors in predicting compressive strength. At 50% training data, RMSE is 6.25 MPa, indicating larger deviations from actual compressive strength. At 90% training data, RMSE drops to 4.96 MPa, showing improved precision in predictions. The R^2 values ranged from 0.90 to 0.93, showing the proportion of variance in the compressive strength explained by the model. Then improved as training data increased, with the best value (0.93) achieved at 90% training data. The higher errors RMSE of 6.25 MPa at 50% training may be linked to insufficient training data capturing the variability of compressive strength. Higher RMSE values at lower training percentages (e.g., 6.25 MPa at 50% training) may be attributed to insufficient training data, limiting the model's ability to capture the full variability of compressive strength. This variability stems from differences in concrete composition, such as water-cement ratios and aggregate quality, as well as experimental inconsistencies in compressive strength measurement.

4.2. Multi-layer perceptron model

The CC values range from 0.96 to 0.98, indicating a very strong relationship between the predicted and actual compressive strength values as mentioned in Table 3. The highest CC 0.98 was observed with 80% training data, demonstrating the model's ability to learn complex relationships with sufficient training data. The predicted values of compressive strength and actual values of compressive strength using MLP model are mentioned in Fig. 2. The R^2 values are consistently around 0.91–0.92, indicating that approximately 91–92% of the variance in compressive strength is explained by the model. While R^2 values are stable, the slight dip to 0.90 at 70% training suggests some variability in performance. MAE values range from 4.17 MPa to 5.20 MPa, reflecting the average prediction error in compressive strength. The best MAE 4.17 MPa was observed at 90% training, indicating the model’s improved accuracy with more training data indicating better alignment with actual compressive strength.

Both MSE and RMSE metrics decrease as training data increases, except for a slight rise at 70% training, indicating variability in the model's learning process. MSE dropped from 35.60 MPa 50% training to 31.46 MPa 90% training. RMSE improved from 5.97 MPa 50% training to 5.61 MPa at 90% training. The small deviations in performance at 70% training with R^2 0.90 and RMSE 6.66 MPa suggest that MLP may be sensitive to data distribution and hyperparameter settings. MLP relies heavily on hyperparameter tuning (e.g., number of layers, neurons, learning rate, batch size).The observed variability at 70% training suggests that the model is somewhat sensitive to the specific data distribution in that training split. If the data distribution changes, the model may struggle to generalize, leading to fluctuations in R^2 and RMSE. MLP performance is influenced by learning rate, activation functions, and weight initialization. The training process might have settled into a suboptimal local minimum, leading to slightly worse predictions.

Table 3. Multi-layer perceptron model performance.

Strength	Testing				
	50%	40%	30%	20%	10%
CC	0.96	0.96	0.97	0.98	0.96
R^2	0.91	0.92	0.90	0.91	0.91
MAE (MPa)	4.71	4.59	5.20	4.60	4.17
MSE (MPa)	35.6	33.78	44.37	33.14	31.46
RMSE (MPa)	5.97	5.81	6.66	5.76	5.61

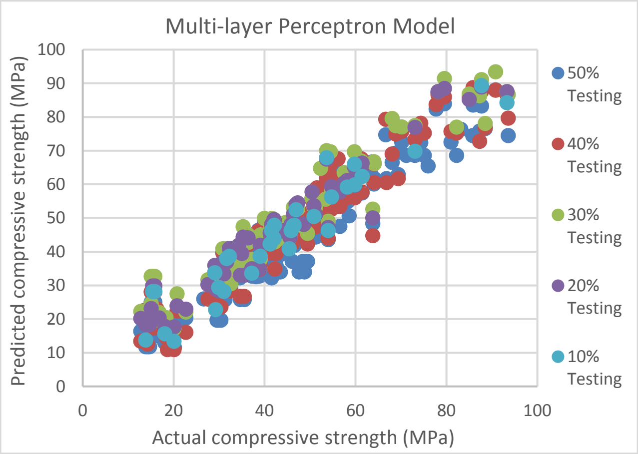

Fig. 2. Multi-layer perceptron model prediction efficiency.

Both MSE and RMSE metrics decrease as training data increases, except for a slight rise at 70% training, indicating variability in the model's learning process. MSE dropped from 35.60 MPa 50% training to 31.46 MPa 90% training. RMSE improved from 5.97 MPa 50% training to 5.61 MPa at 90% training. The small deviations in performance at 70% training with R^2 0.90 and RMSE 6.66 MPa suggest that MLP may be sensitive to data distribution and hyperparameter settings. MLP relies heavily on hyperparameter tuning (e.g., number of layers, neurons, learning rate, batch size).The observed variability at 70% training suggests that the model is somewhat sensitive to the specific data distribution in that training split. If the data distribution changes, the model may struggle to generalize, leading to fluctuations in R^2 and RMSE. MLP performance is influenced by learning rate, activation functions, and weight initialization. The training process might have settled into a suboptimal local minimum, leading to slightly worse predictions.

4.3. M5 rule model

The M5 Rule-Based Model was evaluated for predicting the compressive strength of concrete using different training-to-testing splits as mentioned in Table 4. The CC values range from 0.86 to 0.92, indicating a moderate to strong relationship between predicted and actual compressive strength values. The highest CC 0.92 is observed at both 50% and 90% training data splits, suggesting better predictions with these configurations. The M5 Rule Model leverages these relationships by combining decision trees and linear regression at leaf nodes. The predicted values of compressive strength and actual values are mentioned in Fig. 3. The moderate CC 0.86 −0.92 suggests the model captures the dominant trends but struggles with complex nonlinear dependencies compared to models like MLP. The MAE and RMSE values indicate that the model can provide quick and moderately accurate estimates of compressive strength, reducing the need for extensive laboratory testing. The R^2 values range from 0.74 to 0.87, indicating that the model explains up to 87% of the variability in compressive strength. The R^2 values drop significantly at 70% training 0.74, suggesting potential overfitting or underfitting issues. The MAE values range from 3.00 MPa to 5.28 MPa, reflecting the average prediction error. The best MAE 3.00MPa is achieved at 90% training, while the largest error occurs at 60% training 5.28MPa. MSE values drop significantly from 39.04 MPa for 50% training to 15.34 MPa for 90% training, demonstrating improved predictions with more training data. RMSE follows a similar trend, reducing from 6.25 MPa to 3.92 MPa at 90% training. Higher training data (90%) leads to better generalization, with the best performance in terms of CC, R^2, and MAE. Lower training splits (50–70%) show inconsistent performance, possibly due to overfitting or underfitting. The M5 Rule-Based Model works well for capturing dominant trends but struggles with complex nonlinear relationships, where neural networks like MLP might perform better. Errors decrease as training data increases, indicating the model benefits from more training examples.

Table 4. M5 rule model performance.

Strength	Testing				
	50%	40%	30%	20%	10%
CC	0.92	0.89	0.86	0.89	0.92
R^2	0.87	0.79	0.74	0.79	0.87
MAE (MPa)	4.19	5.28	4.99	4.21	3.00
MSE (MPa)	39.04	41.94	42.53	39.05	15.34
RMSE (MPa)	6.25	6.55	6.79	6.23	3.92

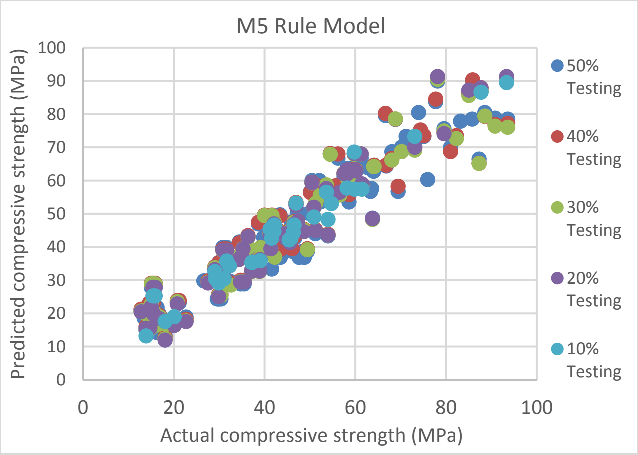

Fig. 3. M5 rule model prediction efficiency.

4.4. Support vector machine model

The analysis uses metrics such as Correlation Coefficient (CC), Coefficient of Determination (R^2), Mean Absolute Error (MAE), Mean Squared Error (MSE), and Root Mean Squared Error (RMSE) to assess the model's performance and reliability as mentioned in Table 5. The CC values range from 0.95 to 0.97, indicating a very strong relationship between predicted and actual compressive strength values. As the testing percentage decreases, CC improves slightly, reaching its peak 0.97 at 10% testing, demonstrating the model's ability to generalize well with sufficient training data. The R^2 values range from 0.90 to 0.94, indicating that up to 94% of the variance in compressive strength is explained by the model. R^2 improves as the testing percentage decreases, reflecting better predictions with more training data. The compressive strength of concrete is influenced by a complex interplay of factors such as water-cement ratio, curing conditions, and aggregate properties. The SVM model, with its capacity to handle nonlinear relationships via kernel functions, effectively captures these interactions as mentioned in Fig. 4. The high CC and R^2 values suggest that SVM models are well-suited for predicting compressive strength, especially in datasets with complex dependencies.

Table 5. Support vector machine model performance.

Strength	Testing				
	50%	40%	30%	20%	10%
CC	0.95	0.95	0.95	0.96	0.97
R^2	0.91	0.91	0.90	0.92	0.94
MAE (MPa)	4.80	4.80	4.80	4.00	3.70
MSE (MPa)	39.68	40.20	41.69	26.91	22.65
RMSE (MPa)	6.30	6.34	6.46	5.19	4.76

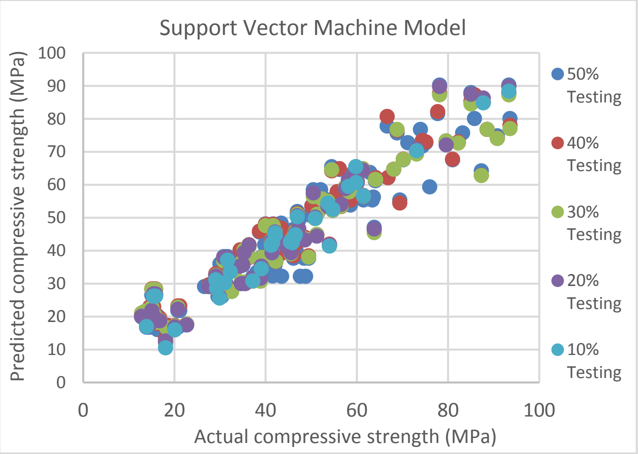

Fig. 4. Support vector machine model prediction efficiency.

The MAE values range from 4.80 MPa (at 50–30% testing) to 3.70 MPa (at 10% testing). The consistent improvement in MAE at lower testing percentages highlights the model's increasing accuracy as more data is used for training. MSE decreases significantly from 39.68 MPa at 50% testing to 22.65 MPa at 10% testing, reflecting reduced prediction errors with larger training datasets. RMSE also follows a downward trend, dropping from 6.30 MPa to 4.76 MPa, further confirming improved precision in predictions. MAE improves from 4.80 MPa (at 50% testing) to 3.70 MPa (at 10% testing), demonstrating that more training data allows the SVM model to better generalize the relationships between features and compressive strength.

The low RMSE values, particularly 4.76 MPa at 10% testing, indicate that the model delivers predictions with minimal deviation from actual compressive strength values. The SVM model's ability to handle nonlinear data (via kernel functions) makes it particularly suitable for datasets where compressive strength exhibits complex dependencies on mix proportions and curing condition.

4.5. Multi-linear regression

To validate the predictive capability of the machine learning-based approach, the Multiple Linear Regression (MLR) model was evaluated using a dataset containing concrete mix properties. The model was constructed to predict compressive strength based on key mix components. The derived regression equation is:

CompressiveStrength = − 1495.02827 + 0.58745 × Cement + 0.57517 × GGBS + 0.77427 × Flyash + 0.74902 × Alcofine + 0.5704 × 20mm + 0.55811 × 10mm + 0.5276 × CRF + 1.51772 × Water + 3.95817 × Admix

The coefficients in the regression equation represent the impact of each component on the compressive strength of concrete. Cement (+0.58745) has a positive and significant impact, reflecting its role as a primary binder. Ground Granulated Blast Furnace Slag (+0.57517) indicates that (GGBS) contributes to strength by enhancing hydration and reducing voids. Flyash (+0.77427) positively influences strength through pozzolanic reactions. Alcofine (+0.74902) indicates that the high coefficient for Alcofine indicates its effectiveness in improving strength, likely due to its ultra-fineness and high reactivity.

- 20mm Aggregate (+0.5704) and 10mm Aggregate (+0.55811) indicate that the coarse aggregates enhance strength by providing a solid framework for the concrete matrix.
- CRF (Crusher Rock Fines) (+0.5276) indicates that fines contribute to improved packing density, enhancing compressive strength.
- Water (+1.51772) indicates that the positive coefficient suggests that water is a key activator for hydration, but excessive water can reduce strength.
- Admixture (+3.95817) indicates that the admixtures significantly enhance strength by improving workability and reducing water demand.
- The negative intercept (−1495.02827) reflects the combined effect of unmeasured factors and baseline mix properties, serving as a constant offset for the regression equation. The CC value obtained was 0.96, R^2 0.92 and MAE 4.18 MPa with RMSE 6.31 MPa were calculated and compared with different machine learning models.

5. Limitations of the Machine Learning Models

While the machine learning models used in this study demonstrate strong predictive capabilities, several limitations must be considered:

- Data Dependency: The performance of ML models is highly dependent on the quality and quantity of training data. Insufficient or biased data can lead to overfitting or underfitting, affecting prediction accuracy.
- Hyperparameter Sensitivity: Models like MLP and SVR require careful tuning of hyperparameters, which can significantly impact their performance. Suboptimal hyperparameters may lead to higher errors.
- Computational Complexity: Advanced models such as MLP and SVR require more computational resources compared to simpler models like linear regression or M5 rule-based models. This can limit their practical application in resource-constrained environments.
- Generalization Issues: While ML models perform well on the training dataset, their ability to generalize to new, unseen data may be limited, especially if the training data does not sufficiently represent all possible variations in concrete mix properties.
- Interpretability: Some ML models, particularly neural networks, act as black boxes, making it difficult to interpret their decision-making process. This can be a drawback for practical applications where explainability is crucial.

Future research should focus on improving model generalization by incorporating more diverse datasets, optimizing hyperparameter selection, and exploring hybrid modeling approaches that combine ML techniques with domain knowledge in concrete materials science.

6. Conclusions

This study evaluated the performance of four machine learning models—Linear Regression (LR), Multi-Layer Perceptron (MLP), M5 Rule-Based Model, and Support Vector Machine (SVM)—in predicting the compressive strength of concrete. The models were assessed based on key metrics such as Correlation Coefficient (CC), Coefficient of Determination (R^2) Mean Absolute Error (MAE), Mean Squared Error (MSE), and Root Mean Squared Error (RMSE) across varying training-to-testing data splits.

The following conclusions summarize the findings:

The selection of machine learning models for this study was based on their ability to capture both linear and nonlinear relationships in the dataset, their predictive accuracy, and their computational efficiency. MLP Model was selected for its ability to model complex nonlinear dependencies in the dataset. It demonstrated superior performance, with the highest CC and R^2 values, making it the most accurate model for compressive strength prediction. Support Vector Machine was selected due to its strong performance in handling high-dimensional data and its robustness in capturing nonlinear patterns. Although slightly less accurate than MLP, it performed well in reducing prediction errors. M5 Rule-Based Model was selected which included as it combines decision trees with linear regression, offering interpretability and reasonable predictive capability. While it struggled with complex nonlinear relationships, it provided quick estimations with moderate accuracy. While Linear Regression was used as a baseline model to evaluate how well simple linear relationships explain compressive strength variations. Though computationally efficient, its performance was lower than that of advanced ML models, justifying the need for more complex algorithms

In linear regression model, achieved a high CC of 0.97 and R^2 of 0.93 at 90% training, indicating a strong ability to explain the variance in compressive strength. While the model performed well, its assumption of linear relationships limits its ability to capture complex nonlinear dependencies, leading to relatively higher error metrics MAE=3.86 MPa and RMSE=4.96 MPa. Suitable for applications where linear trends dominate and simplicity is preferred. The MLP model demonstrated excellent predictive performance, with the highest CC of 0.98 and consistent R^2 values around 0.92. Its ability to model nonlinear relationships resulted in competitive error metrics MAE=4.17 MPa and RMSE=5.61 MPa at 90% training. The MLP model is ideal for capturing complex patterns in datasets, making it a powerful tool for predictive modeling in concrete mix design. The M5 model achieved a maximum CC of 0.92 and R2 of 0.87, with the best error metrics MAE=3.00 MPa and RMSE=3.92 MPa observed at 90% training. While its hybrid approach combining decision trees and linear regression makes it interpretable, its performance was less consistent across all splits, especially for datasets with complex nonlinear dependencies. Suitable for scenarios where simplicity and interpretability are prioritized over absolute accuracy. The SVM model showed strong predictive capabilities, with a CC of 0.97 and the highest R^2 of 0.94, demonstrating its ability to explain up to 94% of the variability in compressive strength. Error metrics MAE=3.70 MPa and RMSE=4.76 MPa at 10% testing highlighted its robustness and accuracy, particularly for datasets with nonlinear relationships. SVM's flexibility through kernel functions makes it an excellent choice for modeling compressive strength with complex dependencies. All four models demonstrated high accuracy in predicting compressive strength, with SVM and MLP excelling in capturing nonlinear relationships, and M5 Rule providing the lowest errors under specific conditions. Among the four model, MLP model exhibited excellent and higher cc values as compared with other machine learning models. The MLP model demonstrated the highest CC value of 0.98 with a 20% testing split, indicating a very strong correlation between predicted and actual values. It also achieved an R^2 value of 0.92, suggesting that it explains approximately 92% of the variance in compressive strength. The MLP model showed superior performance in capturing nonlinear relationships in the dataset, reducing RMSE and MAE values across various training-testing splits. SVM also performed well, achieving CC values between 0.96 and 0.98 and R^2 values around 0.91. The model was able to capture complex patterns in the data but exhibited slightly higher errors than MLP, particularly in MAE and RMSE, suggesting sensitivity to hyperparameter tuning. The M5 model showed moderate performance, with CC values ranging from 0.86 to 0.92 and R^2 values between 0.74 and 0.87. While it effectively combined decision trees with linear regression, it struggled with capturing highly nonlinear relationships, resulting in higher MAE and RMSE values compared to MLP and SVM. While linear regression provided reasonable estimates with CC values of 0.95 to 0.97 and R^2 values of 0.90 to 0.93, it was outperformed by the more complex ML models. The relatively higher RMSE values indicate that linear regression may not fully capture the nonlinear effects influencing compressive strength. Overall, the MLP model outperformed other approaches in terms of correlation and error reduction, making it the most suitable technique for predicting compressive strength in this study. Even when compared with multi linear regression model statistics the MLP model performance showed excellent results.

The performance of all models improved significantly as the training data increased, highlighting the importance of sufficient and high-quality data for model training. Based on the comparative analysis, an 80% training and 20% testing split is recommended for developing a robust model. This split consistently demonstrated strong correlation values (CC∼0.98), high explanatory power (R^2∼0.92), and minimized errors (MAE and RMSE). While 90% training also showed strong results, it may reduce the model's generalizability due to limited testing data. On the other hand, lower training percentages (e.g., 50–60%) exhibited higher errors, likely due to insufficient training data. Therefore, an 80–20 split balances training effectiveness and model validation, ensuring reliable compressive strength predictions. The results suggest that incorporating nonlinearity and advanced learning mechanisms significantly enhances prediction accuracy.

Acknowledgements

None declared.

Funding

The authors received no financial support for the research, authorship, and/or publication of this manuscript.

Conflict of Interest

The authors declared no potential conflicts of interest with respect to the research, authorship, and/or publication of this manuscript.

Author Contributions

All of the authors made substantial contributions to conception and design, or acquisition of data, or analysis and interpretation of data; were involved in drafting the manuscript or revising it critically for important intellectual content; and gave final approval of the version to be published.

Data Availability

The datasets created and/or analyzed during the current study are not publicly available, but are available from the corresponding author upon reasonable request.

REFERENCES

Aydın Y, Ahadian F, Bekdaş G, Nigdeli S (2024). Prediction of optimum design of welded beam design via machine learning. *Challenge Journal of Structural Mechanics*, 10(3), 86-94.

Chou JS, Tsai CF (2012). Concrete compressive strength analysis using a combined classification and regression technique. *Automation in Construction*, 24, 52–60.

Ghoniem AG, Nour LAA (2025). Mechanical properties prediction of sandstone concrete with varying compaction levels and silica fume ratios using machine learning approaches. *Construction and Building Materials*, 460, 139817.

Gürbüz M, Kazaz İ (2024). Ultimate drift ratio prediction of steel plate shear wall systems: a machine learning approach. *Challenge Journal of Structural Mechanics*, 10(2), 34-46.

Harirchian E (2024). Predicting compressive strength of AAC blocks through machine learning advancements. *Challenge Journal of Concrete Research Letters*, 15(2), 56-68.

Huang X, Huang J, Kaewunruen S (2025). An explainable machine learning system for efficient use of waste glasses in durable concrete to maximize carbon credits towards net zero emissions. *Waste Management*, 193, 539–550.

IS 10262 (2019) Concrete Mix Proportioning – Guidelines (Second Revision). Bureau of Indian Standards, New Delhi, India.

Khan MS, Peng T, Khan MA, Khan A, Ahmad M, Aziz K, Sabri MMS, Abd El-Gawaad NS (2025). Explainable AutoML models for predicting the strength of high-performance concrete using Optuna, SHAP and ensemble learning. *Frontiers in Materials*, 12, 1542655.

Li SZ, Wang JJ, Jiang L, Deng R, Wang YH (2025). Machine learning-based strength prediction for circular concrete-filled double-skin steel tubular columns under axial compression. *Engineering Structures*, 325, 119460.

Nalina M (2023). Efficacies of suggested strength-based prediction models for estimation of compressive and tensile properties of normal concrete. *Challenge Journal of Concrete Research Letters*, 14(2), 47-58.

Oyebisi S, Shammas MI, Sani R, Oyewola MO, Olutoge F (2024). Artificial intelligence-based modeling of compressive strength of slurry-infiltrated fiber concrete. *World Journal of Engineering*, ahead-of-print.

Öztaş A, Pala M, Özbay E, Kanca E, Çağlar N, Bhatti MA (2005). Predicting the compressive strength and slump of high strength concrete using neural network. *Construction and Building Materials*, 20(9), 769–775.

Pan B, Liu W, Zhou P, Wu DO (2025). Predicting the compressive strength of recycled concrete using ensemble learning model. *IEEE Access*, 13, 2958-2969.

Quinlan JR (1992). Learning with continuous classes. *Proceedings of the 5th Australian Joint Conference on Artificial Intelligence*, 343–348.

Salami BA, Usman J, Gbadamosi A, Malami SI, Abba SI (2024). Global big data laboratory experiment integrated with kernel-based algorithms for compressive strength modeling. *Scientific Reports*, 14, 30646.

Smola AJ, Schölkopf B (2004). A tutorial on support vector regression. *Statistics and Computing*, 14(3), 199–222.

Tiep NH, Jeong HY, Kim KD, Mung NX, Dao NN, et al. (2024). A new hyperparameter tuning framework for regression tasks in deep neural networks. *Mathematics*, 12(24), 3892.

Topçu IB, Sarıdemir M (2008). Prediction of compressive strength of concrete containing fly ash using artificial neural networks and fuzzy logic. *Computational Materials Science*, 41(3), 305–311.

Ullah I, Javed MF, Alabduljabbar H, Ullah H (2025). Estimating the compressive and tensile strength of basalt fiber-reinforced concrete using advanced hybrid machine learning models. *Structures*, 71, 108138.

Vapnik VN (1995). The Nature of Statistical Learning Theory. Springer.

Witten IH, Frank E (2005). Data Mining: Practical Machine Learning Tools and Techniques. Morgan Kaufmann Publishers.

Yeh IC (1998). Modeling of strength of high-performance concrete using artificial neural networks. *Cement and Concrete Research*, 28(12), 1797–1808.

Challenge Journal of Concrete Research Letters

Research Article

The engineering properties of silica fume and GGBS-based geopolymer mortars cured in elevated temperature

Fuad Abutaha [a,*], Asude İrem Çelik [a]

[a] *Department of Civil Engineering, Antalya Bilim University, 07190 Antalya, Türkiye*

ABSTRACT

Geopolymer, a promising alternative to traditional portland cement, offers a wide range of sustainable applications in the construction industry. Geopolymer mortar presents a sustainable future by mitigating carbon dioxide emissions associated with cement production. This study aims to investigate the effect of using different minerals admixtures and different curing methods on the engineering properties of geopolymer mortar. The study also investigates the possibility of incorporating geopolymer concrete to develop construction with sustainability features. Five different mixes were prepared by utilizing various mineral admixtures in different ratios of silica fume (SF) and granulated blast furnace slag (GGBS), M20-80 (20% SF and 80% GGBS), M80-20 (80% SF and 20% GGBS), M50-50 (50% SF and 50% GGBS), MS100 (100% GGBS), MSF100 (100% SF). The curing methods for each sample were investigated separately under ambient and oven temperatures (65 °C) for 7 and 28 days to determine the compressive and flexural strength of the samples. The results revealed that the compressive strength value of the mixes MS100, M50-50 and M80-20 in which the curing of ambient method is used show significant increment compared to the same mixes cured in oven temperature. The increment in compressive strength of the ambient curing method was 14.4%, 25.8% and 46.4% for the mixes of MS100, M50-50 and M80-20, compared to the oved curing method, respectively. However, the compressive strength value of the mix of M20-80 and MSF100 cured in oven temperature shows similar compressive strength compared to the ambient temperature curing method.

ARTICLE INFO

Article history:

Received	– January 24, 2025
Revision requested	– February 25, 2025
Revision received	– March 10, 2025
Accepted	– March 22, 2025

Keywords:

Engineering properties
Geopolymer concrete
Mineral admixtures
Sustainability

Citation: Abutaha F, Çelik Aİ (2025). The engineering properties of silica fume and GGBS-based geopolymer mortars cured in elevated temperature. *Challenge Journal of Concrete Research Letters*, 16(2), 69–84.

1. Introduction

Geopolymer concrete, initially developed by French Professor Davidovits in 1978, represents a cement-free type of concrete with mechanical and high-temperature resistances (Aleem and Arumairaj 2012). These alternatives gain prominence for its potential to mitigate environmental harm associated with traditional cement sources, particularly the pollutants found in fly ash (FA) and granulated blast furnace slag (GGBS) (Alcan et al. 2023; Alnahhal et al. 2018). The primary source of fly ash, a key component of geopolymer materials, contains alumina, ferric oxide, and silica, which, due to their structural behavior, pose environmental concerns (Khan et al. 2021). Notably, aluminosilicate materials like fly ash and GGBS, when properly harnessed, can serve as sustainable alternatives. The preference for F type fly ash over C type is attributed to its lower contamination and higher alumina oxide content (Fernández-Jiménez and Palomo 2003).

Utilizing FA as a binder in mortar enhances its eco-friendliness, reducing the need for Ordinary Portland Cement (OPC) and contributing to a more sustainable construction industry. The use of solid waste and by-prod-

---

* *Corresponding author*. Tel.: +90-242-245-0000 ; E-mail address: fuad.abutaha@antalya.edu.tr (F. Abutaha)

ISSN: 2548-0928 / DOI: https://doi.org/10.20528/cjcrl.2025.02.003

ucts in construction has gained the attention of many researchers (Abutaha et al. 2016, 2017; Ibrahim et al. 2017). Geopolymer mortar is a blend of source materials and alkaline liquids, with Si and Al serving as the main activators. Notably, the absence of additional water during manufacturing eliminates the hydration process, differentiating it from traditional mortar (Al-Bakri et al. 2012). The ecological balance benefits from reducing OPC production, making geopolymer mortar a crucial player in promoting sustainability. Approximately 600,000 tons of fly ash are produced, but only a fraction is utilized for concrete production, highlighting the underutilized potential of geopolymer materials (Van Chanh et al. 2008).

Geopolymer concrete, utilizing sodium hydroxide and sodium silicate as alkali activators, offers an eco-friendly alternative to OPC. The absence of a hydration process in geopolymer concrete eliminates the need for curing, contributing to its sustainability. Geopolymer mortar's suitability and sustainability in the compatibility of silica and alumina content, fostering reactions without the need for additional water (Mucsi et al. 2018). Geopolymers, being amenable to low-tech and high-tech applications, present a viable replacement for conventional materials in the building sector. Their ease of use, energy efficiency, eco friendliness, high durability, and good mechanical qualities position geopolymers as an environmentally conscious choice.

Geopolymer stands out as a promising candidate for replacing traditional Portland cement, offering a range of applications in sustainable construction, including concrete materials, fire-retardant coatings, fiber-reinforced composites, and waste-immobilization solutions for chemical and nuclear sectors. Extensive research has pointed out that Geopolymer (GP) concrete shares comparable properties with OPC concrete, indicating its suitability for civil engineering applications (Singh et al. 2015). Notably, the ceramic-like characteristics inherent in GP enable it to withstand high temperatures and fire, adding to its versatility (Kong and Sanjayan 2010).

Low-calcium (ASTM Class F) fly ash obtained from coal burning power stations, was successfully used in the production of geopolymer concrete (GPC) (Rangan 2014). However, the compressive strength of fly ash based geopolymer concrete can be also improved when FA is partially replaced with OPC. Among different replacement level of FA with OPC, the maximum strength was achieved at 20% replacement at all ages (Mehta and Siddique 2017). Superior durability was demonstrated with FA-based geopolymer. However, GGBS-based geopolymers are more acid resistant and have higher initial strengths (Duxson et al. 2007a).

After thermal curing, alkali-activated fly ash concrete reaches a compressive strength of 60 MPa as well as superior resistance to sulfate attack, aggressive acids, chlorides, and aggregate-alkali reaction, all of which make it a great alternative to OPC mortars in hazardous waste treatment and reinforcing steel bonding (Boonserm et al. 2012; Deb et al. 2016; Rashad and Zeedan 2011). Fly ash and GGBS work well together to provide strength and stability because the alumina silicate components dissolve, polymerize with alkali, condense, and solidify (Nagajothi and Elavenil 2021). Due to its nearly comparable compressive strength to conventional concrete, GGBS-fly ash-based geopolymer concrete can be used in place of traditional concrete (Nagajothi and Elavenil 2021).

Geopolymers' ceramic-like properties provide them with good fire resistance. As a result, geopolymer-based concrete is considered more fire resistant than traditional OPC-based concretes (Hussin et al. 2015). Recent developments in geopolymer concrete have made it popular because of its simplicity of use, better performance, and lower carbon footprint than traditional OPC concrete (Mathew and Joseph 2018).

Despite these promising attributes, there is a notable gap in the existing literature, particularly concerning the combined effects of silica fume (SF) and GGBS under different ambient and oven temperatures. The optimization of results in this context is essential for understanding the intricate correlation between temperature variations and the presence of mineral admixtures. Bridging this gap in knowledge will not only contribute to the comprehensive understanding of geopolymer materials but also offer insights into their optimal performance in diverse environmental conditions.

This study focuses on addressing this research gap, shedding light on the specific interactions and outcomes resulting from the combination of silica fume and GGBS at varying temperatures. By doing so, the study aims to provide valuable information for optimizing geopolymer formulations, considering both temperature effects and the presence of mineral admixtures. The study is designed to investigate the effect of using different minerals admixtures, and the effect of curing methods on the engineering properties of geopolymer mortar and investigate the possibility of incorporating geopolymer concrete to developed construction areas with sustainability features. This optimization is crucial for advancing the practical application of geopolymer materials and fostering their role in sustainable construction practices.

2. Sustainability of Geopolymer Concrete

Previously, concrete was considered as one of the most important construction materials with the best engineering properties, cost-efficiency and good durability, compared to the other construction materials (Srivastava et al. 2025; Urtekin and Çelik 2025; Narwade and Jadhav 2025). However, the production process of cement-based concrete causes harmful effects on the environment (Al-Safi et al. 2025; Shehata et al. 2022). Cement-based concrete such as OPC which is widely used construction material, significantly contribute to the greenhouse gases emission (Wasim et al. 2021). The production of cement contributes to almost 7% of the global emission of CO_2 (Mathew and Joseph 2018).

Recently, the adoption of geopolymer concrete as a construction material is showing promise option; as a sustainable replacement to the traditional cement-based concrete for green environment and reduce greenhouse gas emission by using raw materials like industrial wastes (Shehata et al. 2022). Geopolymer concrete (GPC) is becoming widely used in different industries due to the special properties of GPC like the significant mechanical properties and the improvement in chemical and thermal resistance.

The demand for concrete will increase in the future, indicating that the consumption of GPC using industrial by-product will provide an alternative solution to the increment of concrete demand (Sumajouw et al. 2007). More than 50% of the greenhouse gas emission resulted from the production of cement. Thereby, GPC is considered as an alternative sustainable construction materials compared to the traditional cement-based concrete (Danish et al. 2022). Furthermore, incorporating GGBS which is a waste by-product of steel fabrication, in the production of GPC contributes to reduce the carbon dioxide emission and the energy levels can be assumed to be zero (Qaidi et al. 2022).

3. Experimental Procedure

The properties of geopolymer mortar (GM) exhibit a correct correlation with the material properties involved. Each property plays a vital role in the strength of GM. Fig. 1 illustrates some of the factors affecting geopolymer mortar, emphasizing their significance in determining strength of the geopolymer concrete. Geopolymer is a type of aluminosilicate binder material formed through the activation of solid aluminosilicate-based materials, such as silica fume, ground granulated blast slag, and alkaline solutions like sodium hydroxide and silicate solutions. Geopolymers are produced by blending mineral admixtures with an alkaline activator solution, resulting in a substance referred to as geopolymer paste. This mixture typically forms a homogeneous slurry with a dark green color.

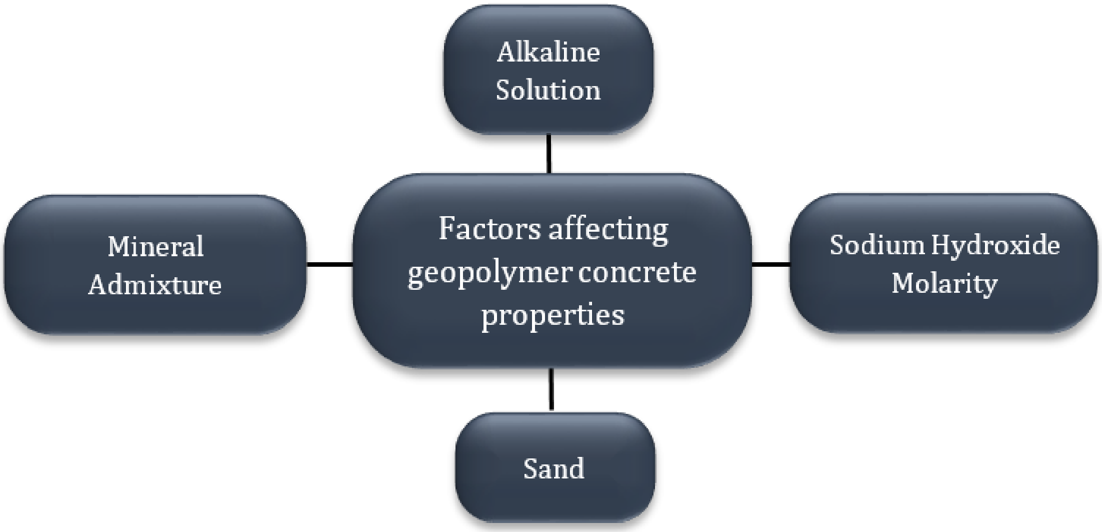

Fig. 1. Factors affecting geopolymer mortar properties.

4. Materials and Method

4.1. Mineral admixtures

Considering the alarming one-to-one carbon dioxide emission ratio associated with cement production (Akbar and Liew 2021), geopolymer mortar, often referred to as "green mortar" (Zhao et al. 2021), emerges as a promising solution due to its cement-free composition and reliance on mineral admixtures. Inorganic polymers derived from aluminosilicates are referred to as geopolymers. These can be created by synthesising pozzolanic chemicals or aluminosilicate source materials with very alkaline solutions. Aluminosilicate materials like fly ash and GGBS, when properly harnessed, can serve as sustainable alternatives. These amorphous alumina silicates, produced through the reaction between silica and alumina silicate, exemplify eco-friendly features (Mucsi et al. 2018).

In the preparation of geopolymer mixes, this study demonstrates specific synthesizing parameters to highlight the effect of mineral admixtures on the engineering properties of GM. The inclusion of mineral admixtures significantly impacts the compressive strength and flexural strength of geopolymer mortar. Due to a lack of studies on the combination of SF and GGBS at both ambient and oven temperatures, this research was conducted to investigate their engineering properties cured at elevated temperatures. Their effect on the geopolymer mortar has been examined independently under the categories of mineral admixtures and alkaline activators.

Silica fume is a micro-sized material that can be utilized in concrete as a mineral additive due to its high Si and Al content and pozzolanic features. It improves granulometry by filling the spaces between cement grains. GGBS is a by-product of iron production in blast furnaces in iron and steel plants. The blast furnace slag is granulated through abrupt cooling and subsequently ground.

This study examines the impact of different additives, such as silica fume and ground granulated blast slag, on the mechanical properties of geopolymer mortar. Each sample exhibits distinct properties based on the materials used. These properties are a result of the mineral admixture content utilized in geopolymer mortar. The general materials used in the production of geopolymer mortar in this study are shown in Fig. 2.

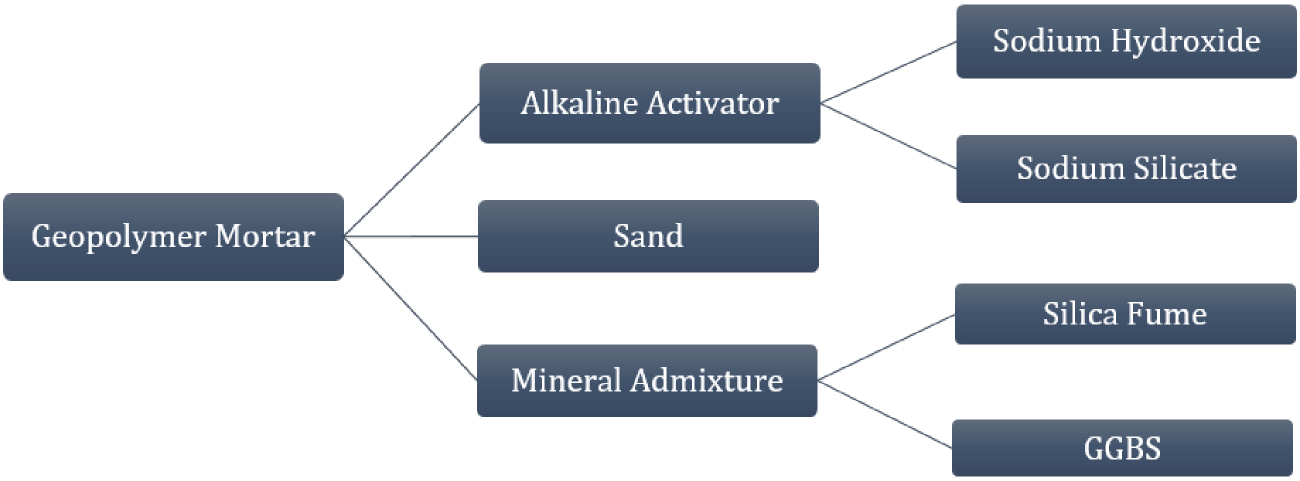

Fig. 2. Geopolymer mortar mixture demonstration.

4.2. Alkaline solutions

A mixture of sodium silicate and sodium hydroxide were used as the alkaline solution in the production of GM. The ratio of sodium hydroxide to sodium silicate was maintained throughout the entire study. Alkaline solution ratio for each sample was also maintained constantly to observe only the effect of mineral admixtures on the engineering properties of GM.

Sodium silicate (Na_2SiO_3), also known as waterglass, is available in the market in both gel and solid forms. Sodium hydroxide (NaOH) is also commonly available in the market in pellet or flake form, and the cost of the product is dependent on the purity of its ingredients. In this study, sodium hydroxide (NaOH) solution with a molarity of 8M was prepared by dissolving it in pure water.

NaOH with 8M molarity was consistent for each specimen to determine only the effect of different mineral admixture on the engineering properties of geopolymer mortar samples. The concentration of 8M denotes that the amount of sodium hydroxide (NaOH) in one liter of water is 8×40=320g, where 40 is the molecular weight of NaOH. Dissolved sodium hydroxide (NaOH) pellets were used to achieve this concentration.

The NaOH solution was prepared at the planned concentrations and allowed to stand at room temperature for 24 hours, covered with nylon to prevent heat dissipation and water evaporation as shown in Fig. 3.

4.3. Preparation of geopolymer mortars

The mix proportion used in the preparation of the geopolymer mortar specimens are shown in Table 1. Five different mixes were prepared by using various mineral admixtures in different ratios of silica fume (SF) and granulated blast furnace slag (GGBS), M20-80 (20% SF and 80% GGBS), M80-20 (80% SF and 20% GGBS), M50-50 (50% SF and 50% GGBS), MS100 (100% GGBS), MSF100 (100% SF).

Fig. 3. Preparation of 8M sodium hydroxide solution.

Table 1. Mixture proportion of geopolymer mortars.

Mixture proportions	Mix code	Silica fume (g)	GGBS (g)	Sodium silicate (ml)	Sodium hydroxide (ml)	Sand (g)	Liquid/Powder ratio
1th mix	M20-80	90 (20%)	360 (80%)	66	134 (8M)	1350	0.44
2nd mix	M80-20	360 (80%)	90 (20%)				
3rd mix	M50-50	225 (50%)	225 (50%)				
4th mix	MS100	NA	450 (100%)				
5th mix	MSF100	450 (100%)	NA				

The fundamental step involves preparing materials properly to obtain the most effective final test results. A programmable mortar mixer (Fig. 4) is used with properties designed to meet standard requirements for mixing mortars and cement pastes. The mixing paddle employs a planetary motion and is driven by a motor with a microprocessor-based speed. The mixer features preset programs complying with (EN 196-1, 2016) standards. The mixer includes an automated sand dispenser for automatic sand discharge. The user can monitor the mixed time on the display, and a lamp signals critical time.

Fig. 4. Automatic programmable mortar mixer.

The alkaline solution was prepared by converting milliliters into grams using density. Sodium silicate has a density of 1.38 kg/m^3, and sodium hydroxide has a density of 1.28 kg/m^3. The conversion results in 91 grams of sodium silicate and 171 grams of sodium hydroxide used in this study.

Silica fume, ground granulated blast slag, and sand were mixed for 5 minutes to prepare geopolymer specimens. Afterward, the activating solution was added and mixed sequentially. The mortar was then cast into prismatic molds of 40 mm × 40 mm × 160 mm (Fig. 5). Subsequently, the samples were then vibrated for 1 minute to remove entrained air, the samples were then sealed with a film to prevent moisture loss from the surface. After proper casting, the specimens were left at ambient temperature for 24 hours and demolded the next day then placed in the laboratory until the day of testing.

Fig. 5. Prism mold demonstration.

The geopolymer mortar samples were tested at the age of seven (7) and twenty-eight (28) days cured in ambient and elevated temperature (Figs. 6 and 7), representing early and final strength, respectively. Part of the specimens were cured in oven temperature at 65C until the age of testing (Fig. 8).

Three samples were taken from each sample group, and the results were determined by taking the average of three samples in the flexural strength test and an average of 6 samples in the compressive strength test. This methodology, employing 5 different ratios of raw materials with the same alkaline activator and sand content, elucidates the impact on compressive and flexural strength.

It also highlights the fundamental role of mineral admixtures in the geopolymer mortar structure. The testing age along with the corresponding number of samples are shown in Table 2. A total of 60 samples were utilized in the experimental phase, enabling a comprehensive comparison of results across various mineral admixtures cured in ambient and elevated temperatures.

4.4. Experimental investigation

The flexural test measures the force presupposed to bend a beam under three-point loading conditions. The data is generally utilized to distinguish the materials for parts that will support loads without flexing. Flexural modulus is used as an indication of a material's stiffness when flexed. Typically, a prism-shaped specimen is placed between the plates of a compression-testing machine (Fig. 9), applying a gradually increasing load until fracture occurs. After the flexural strength test, each sample was splitter into two pieces due to the fracture. The samples were then used for compressive strength tests. The compressive strength test measures the maximum compressive load a material can withstand before fracture. Each test requires three samples, and the average of the three samples determines the compressive and flexural strength.

In this study, each geopolymer mortar sample undergoes compressive and flexural strength testing at 7 and

28 days. The results illustrate the impact of mineral admixture content on the mortar. Both compressive and flexural strength tests were conducted on the formulated geopolymer mortar. In the flexural testing, samples were positioned in the compression machines with one side facing the supporting rollers, and the longitudinal axis parallel to the supports. Vertical loads were applied by the loading rollers on the opposite side of the prism/sample's face, with a uniform load increase. After specimens' failure, half of the prism/sample were then used for compressive strength testing was laterally centered on the machine's platen. The maximum force applied was recorded, along with the specimen's dimensions, the compressive strength was then calculated. The final compressive strength value represents the average of six individual test samples. For early strength, each specimen underwent separate testing. The final strength at 28 days was obtained for this testing phase. Additionally, the impact of heat was observed separately for 7 and 28 days.

Fig. 6. 7-day ambient temperature specimen samples.

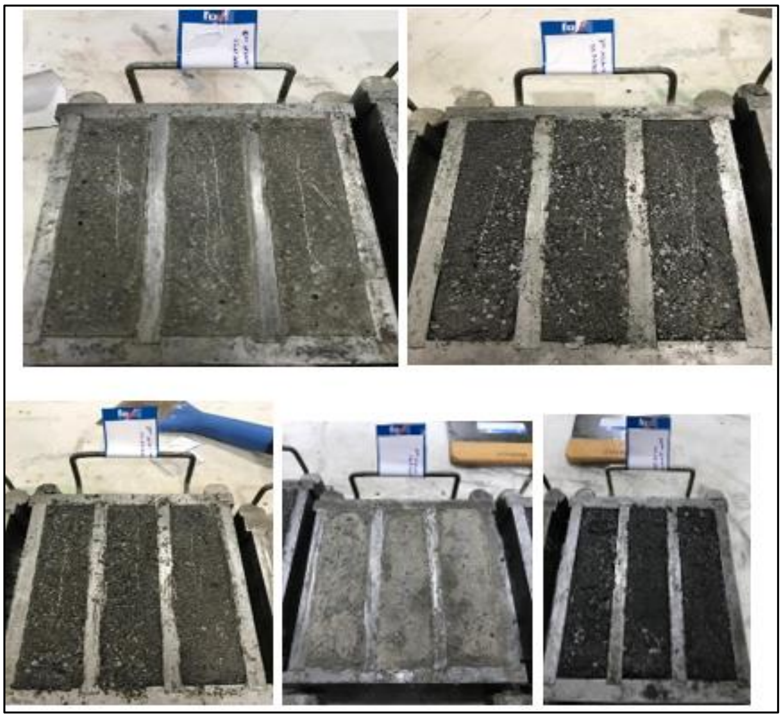

Fig. 7. 28-day ambient temperature specimen samples.

Fig. 8. 7-day specimen samples cured in 65 °C oven temperature.

Table 2. Number of samples required for compressive and flexural strength tests.

Age	Curing method	Compressive strength/Flexural strength				
		M20-.80	M80-20	M50-50	MS100	MSF100
7 days	Ambient	3	3	3	3	3
	Oven temp.	3	3	3	3	3
28 days	Ambient	3	3	3	3	3
	Oven temp.	3	3	3	3	3

Fig. 9. Flexural and compressive strength test setup.

5. Results and Discussion

This section presents and discusses experimental results, specifically focusing on the strength development of geopolymer mortar under ambient and oven curing methods. The factors determined in the previous methodology section are considered. For all specimens, the liquid/powder ratio remained constant at 0.44, with only the percentages of mineral admixtures varying. Results for each test are presented separately based on their mineral admixture content and curing method.

5.1. Compressive strength results

The mixtures were prepared to study the effect of various parameters on compressive strength. Part of the mixtures were prepared to study the effect of curing temperature on the compressive strength of geopolymer mortar. Each mixture is separately discussed below.

Table 3 shows the compressive strength values of the 7 days' samples cured at ambient and oven temperatures. The 7-day compressive strength results of the samples cured in ambient temperature ranged between

14.67 to 58.79 MPa as shown in Fig. 10. The maximum compressive strength was for the mix of MS100, and the minimum compressive strength value was for the mix of MSF100.

The compressive strength of MS100 was 4.7%, 40.3%, 41.5% and 75% higher than M20-80, M80-20, M50-50 and MSF100, respectively. However, the 7-day compressive strength results of the samples cured in oven temperature were in the range between 18.4–70.8 MPa. The results revealed that the maximum compressive strength was for the mix of M20-80 and the minimum compressive strength value was for the mix of MSF100. The compressive strength of M20-80 was 66.6%, 65.2%, 41.6% and 73.9% higher than M80-20, M50-50, MS100 and MSF100, respectively. The comparison between the Seven-day compressive strength results of oven and ambient curing methods is shown in Fig. 12. The compressive strength values of the mixes of MS100, M50-50 and M80-20 in which the curing of ambient method is used show significant increment compared to the same mixes cured in oven temperature. The increment in compressive strength of the ambient curing method was 29.6%, 28.2% and 32.5% higher for the mixes of MS100, M50-50 and M80-20, compared to the oved curing method, respectively. However, the compressive strength value of the mix of M20-80 cured in oven temperature shows higher compressive strength compared to the ambient temperature curing method.

Table 3. 7-day compressive strength values.

Curing method	7-day compressive strength (MPa)				
	M20-80	M80-20	M50-50	MS100	MSF100
Ambient temperature	52.85	30.01	31.22	58.02	17.36
	63.89	39.98	37.75	59.08	11.18
	51.82	31.05	37.01	57.68	17.98
	61.28	40.02	30.15	59.02	11.28
	50.05	29.87	31.98	58.88	18.05
	59.98	39.50	37.98	59.35	12.22
Average	56.65	35.07	34.33	58.67	14.67
Oven temperature (65 °C)	62.95	18.12	23.83	42.73	17.06
	65.86	23.28	25.51	42.31	18.93
	74.88	22.45	25.31	39.75	18.76
	75.89	24.59	24.89	40.09	19.34
	71.45	29.95	23.88	39.98	17.98
	69.67	23.56	24.5	43.21	18.55
Average	70.11	23.66	24.65	41.35	18.44

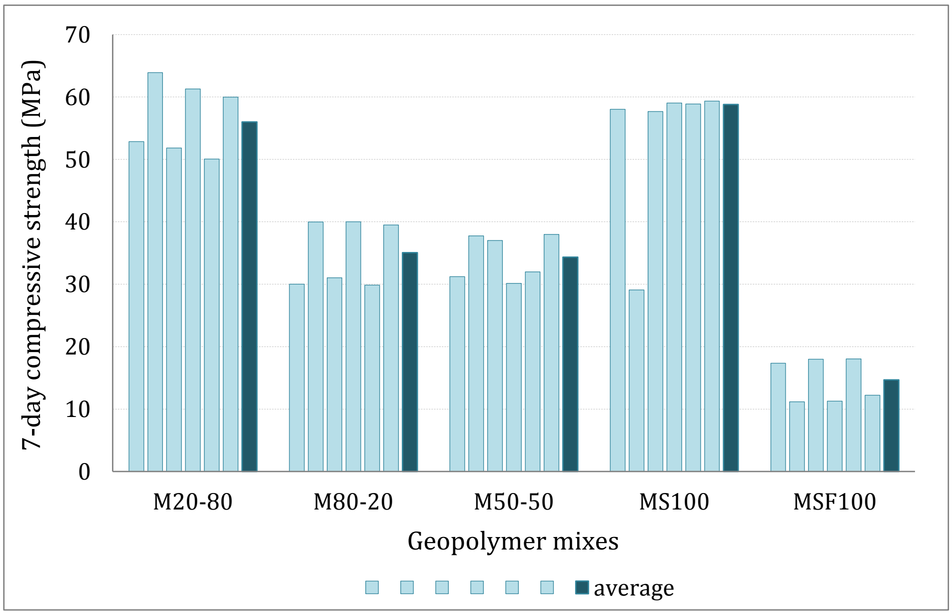

Fig. 10. 7-day compressive strength for ambient temperature.

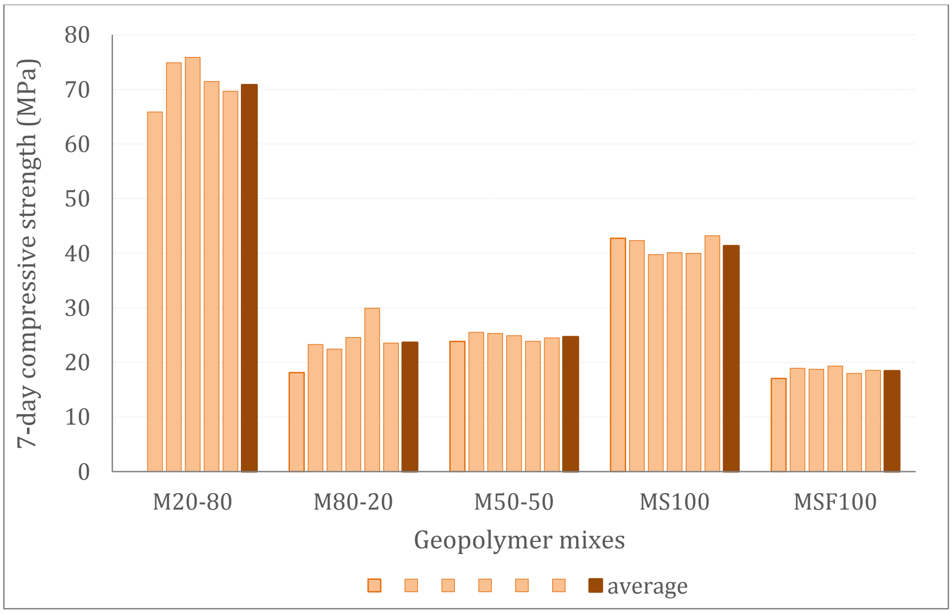

Fig. 11. 7-day compressive strength for oven temperature.

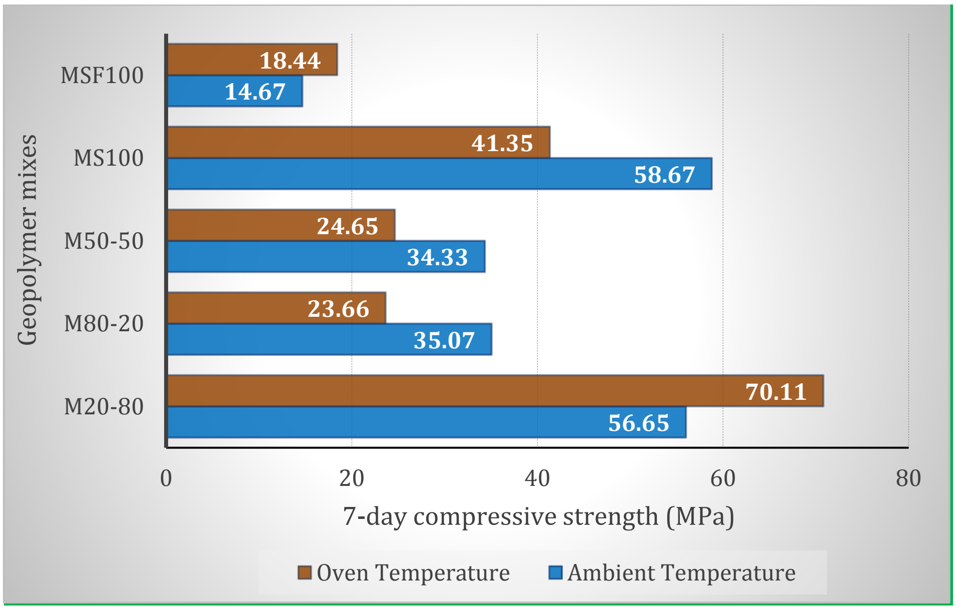

Fig. 12. 7-day compressive strength comparison.

Fig. 13 shows the 28-day compressive strength results of the samples cured in ambient temperature. The compressive strength values ranged between 19.2 to 70.7 MPa. The results revealed that the maximum strength was for the mix of M20-80 and the minimum compressive strength value was for the mix of MSF100. The compressive strength of M20-80 was 27.9%, 26.5%, 14.5% and 72.8% higher than M80-20, M50-50, MS100 and MSF100, respectively. Fig. 14 shows the 28-day compressive strength results of the samples cured in oven temperature. The compressive strength values of the mixes were in the range between 21.1–70.6 MPa. The maximum compressive strength was for the mix of M20-80 and the minimum compressive strength value was for the mix of MSF100. The maximum compressive strength of M20-80 was 61.3%, 44.3%, 26.75% and 70.2% higher than M80-20, M50-50, MS100 and MSF100, respectively.

The comparison between the 28-day compressive strength results of oven and ambient curing methods is shown on Fig. 15. The compressive strength values of the mixes of MS100, M50-50 and M80-20 in which the curing of ambient method is used show significant increment compared to the same mixes cured in oven temperature. The increment in compressive strength of the ambient curing method was 14.4%, 25.8% and 46.4% for the mixes of MS100, M50-50 and M80-20, compared to the oved curing method, respectively. However, the compressive strength value of the mix of M20-80 and MSF100 cured in oven temperature shows similar compressive strength compared to the ambient temperature curing method. Thus, there is no significant change that was observed in compressive strength values of the oven temperature and the ambient temperature curing method.

According to Shukor Lim et al. (2018), geopolymer mortar samples were immediately placed in an oven at 90 °C after casting, the compressive strength was decreasing as the heat curing duration increased. Rapid strength was observed up to 24 hours, then the strength became moderate or weak. For 24 hours of heat curing, the compressive strength was 31.46 MPa, slightly increasing to 32.1 MPa for 48 hours. Prolonged heat curing may weaken the mineral structure, and it is suggested not to exceed 24 hours in practical applications. The general assumption is that GGBS content is more effective, while SF results in lower workability and lower strength values. The study indicates that oven and room temperatures do not directly correlate with results. GGBS content penetrates alkaline solutions more than SF, providing durability to geopolymer mortar. The result of this study are with agreement of previous studies, geopolymers demonstrated a high degree of chemical stability when exposed to high temperatures (Duxson et al. 2006; Duxson et al. 2007b; Krivenko and Kovalchuk 2007). When exposed to high temperatures, geopolymer concrete exhibits remarkable stability, low shrinkage, and good resistance to freeze/thaw (Hussin et al. 2015; Rashad and Zeedan 2011). Further, the properties of GPC including the compressive strength and workability are affected by the properties of the ingredients that make the GP paste (Rangan 2014). Heat-cured geopolymer concrete based on Metakaolin and low calcium fly ash is thought to be a model building material (Luhar et al. 2021). Geopolymer specimens demonstrated lower compressive strength after high-temperature exposure to 900 °C (Mathew and Joseph 2018). Referring to the study by Narayanan and Shanmugasundaram (2017), geopolymer mortar develops sufficient strength even under ambient temperature conditions without conventional curing. Industrial by-products like GGBS and silica fume can be advantageously used in producing ambient-cured geopolymer composites. In general, the strength of ambient-cured geopolymer mortar increases with the rise in GGBS content. Parameters such as alkaline activator molarity, liquid/powder ratio, and binder/aggregate ratio influence the strength development of ambient-cured geopolymer mortar. Rangan (2014) investigated the effect of curing method on the properties of GPC, the study demonstrated that GPC cured in elevated temperature significantly assists the chemical process that takes place within the geopolymer paste. The improvement of compressive strength of the geopolymer concrete mixes cured in high temperature is attributed to the geopolymer mechanism of the polymerization reaction of the silica and the alumina released form the alkaline activation solution with FA (Mehta and Siddique 2017). Furthermore, GGBS may be added to the mixture of FA GPC to promote room-temperature curing and accelerate the setting time of fresh geopolymer concrete (Rangan 2014). Therefore, geopolymer mortar holds promise as an eco-friendly and sustainable construction material to produce new-generation mortar or concrete.

Table 4. 28-day compressive strength values.

Curing method	28-day compressive strength (MPa)				
	M20-80	M80-20	M50-50	MS100	MSF100
Ambient temperature	70.94	52.85	45.80	62.44	19.52
	68.55	51.41	51.09	56.78	18.77
	68.60	50.96	52.57	57.98	18.56
	72.77	51.95	68.75	63.35	18.98
	73.85	49.85	46.85	60.43	19.56
	69.97	48.79	46.89	61.85	20.02
Average	70.78	50.97	51.99	60.47	19.23
Oven temperature (65 °C)	69.92	26.85	38.48	55.56	23.44
	72.85	26.98	37.65	53.45	18.75
	69.55	27.78	39.79	52.12	19.87
	71.95	27.21	39.92	50.43	22.45
	68.44	25.95	38.44	49.65	21.77
	70.98	28.99	39.65	49.12	20.19
Average	70.61	27.29	39.32	51.72	21.08

5.2. Flexural strength results

The 7-day flexural strength results of the samples cured in ambient temperature is shown on Fig. 16. The flexural strength values ranged between 1.7 to 5.8 MPa. The maximum flexural strength was for the mix of MS100, and the minimum flexural strength value was for the mix of MSF100.

The flexural strength of MS100 was 12.7%, 60.5%, 37.9% and 70.2% higher than M20-80, M80-20, M50-50 and MSF100, respectively. However, the 7-day flexural strength results of the samples cured in oven temperature were in the range between 1.8–6.8 MPa as shown in Fig. 17. The maximum flexural strength was for the mix of M20-80 and the minimum flexural strength value was for the mix of MSF100. The flexural strength value of M20-80 was 70%, 47.8%, 35.7% and 72.5% higher than M80-20, M50-50, MS100 and MSF100, respectively. The comparison between the 7-day flexural strength results of oven and ambient curing methods is shown in Table 5. The flexural strength values of the mixes MS100, M50-50 and M80-20 in which the curing of ambient method is used show significant increment compared to the same mixes cured in oven temperature. The increment in flexural strength of the ambient curing method was 25.6%, 2.7% and 12% for the mixes of MS100, M50-50 and M80-20, compared to the oved curing method, respectively. However, the flexural strength value of the mix of M20-80 and MSF100 cured in oven temperature shows increment compared to the ambient temperature curing method. The increment in flexural strength of the oven curing method was 32.5% and 6.8% higher for the mixes of M20-80 and MSF100, compared to the oven curing method, respectively.

Fig. 13. 28-day compressive strength for ambient temperature.

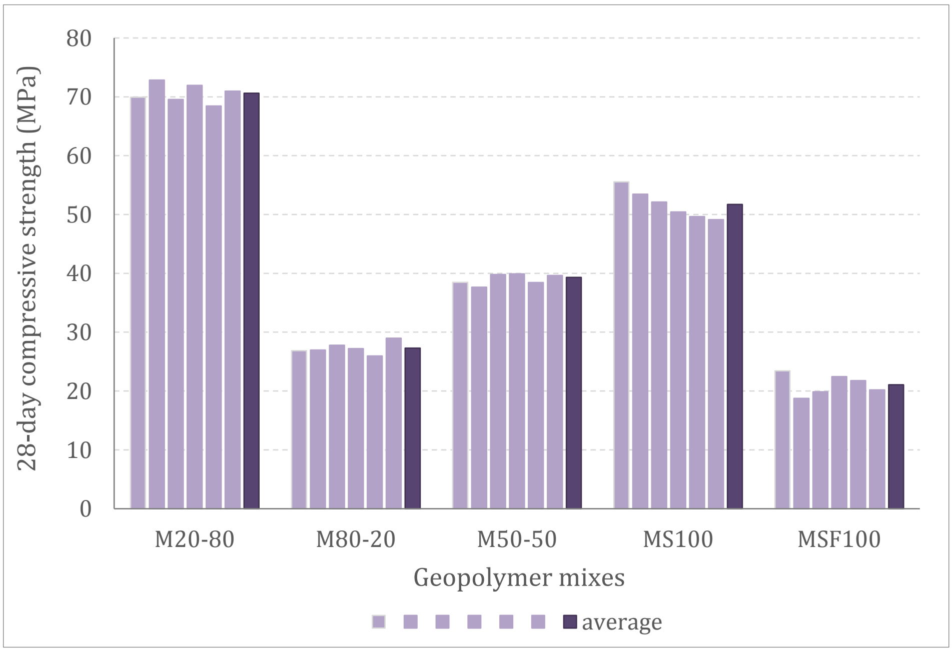

Fig. 14. 28-day compressive strength for oven temperature.

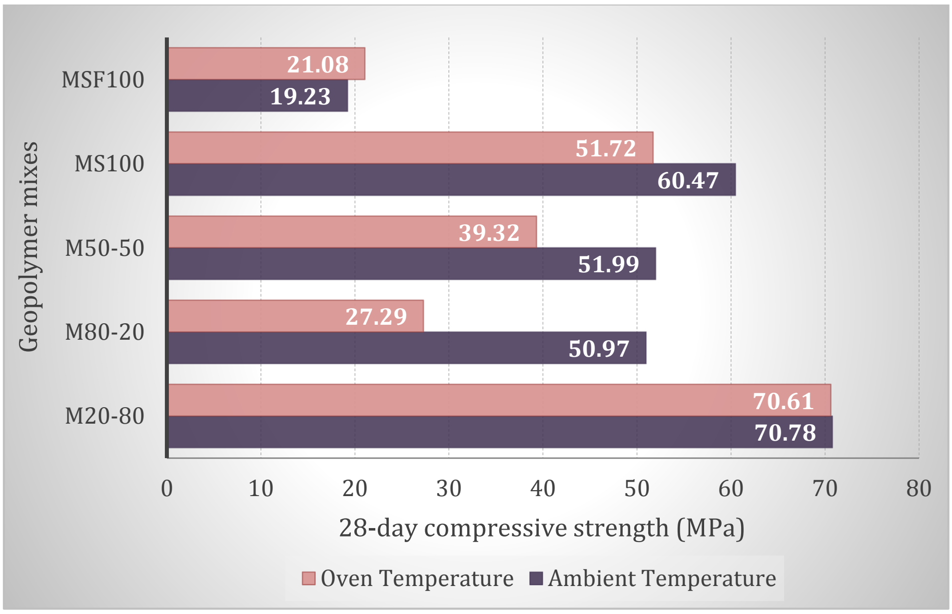

Fig. 15. 28-day compressive strength comparison.

Table 5. 7-day flexural strength values.

Curing method	7-day flexural strength (MPa)				
	M20-80	M80-20	M50-50	MS100	MSF100
Ambient temperature	5.13	2.32	3.65	5.88	1.73
	5.18	2.3	3.67	5.85	1.75
	5.10	2.35	3.64	5.89	1.77
Average	5.14	2.32	3.65	5.87	1.75
Oven temperature (65 °C)	6.78	2.08	3.5	4.33	1.82
	6.82	2.10	3.5	4.38	1.93
	6.79	1.95	3.59	4.41	1.88
Average	6.80	2.04	3.53	4.37	1.88

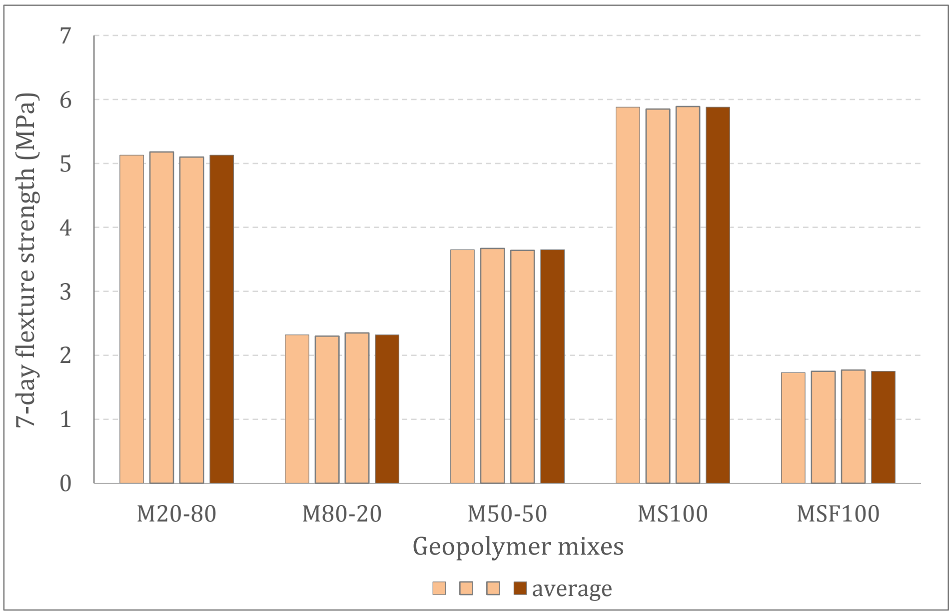

Fig. 16. 7-day flexural strength for ambient temperature.

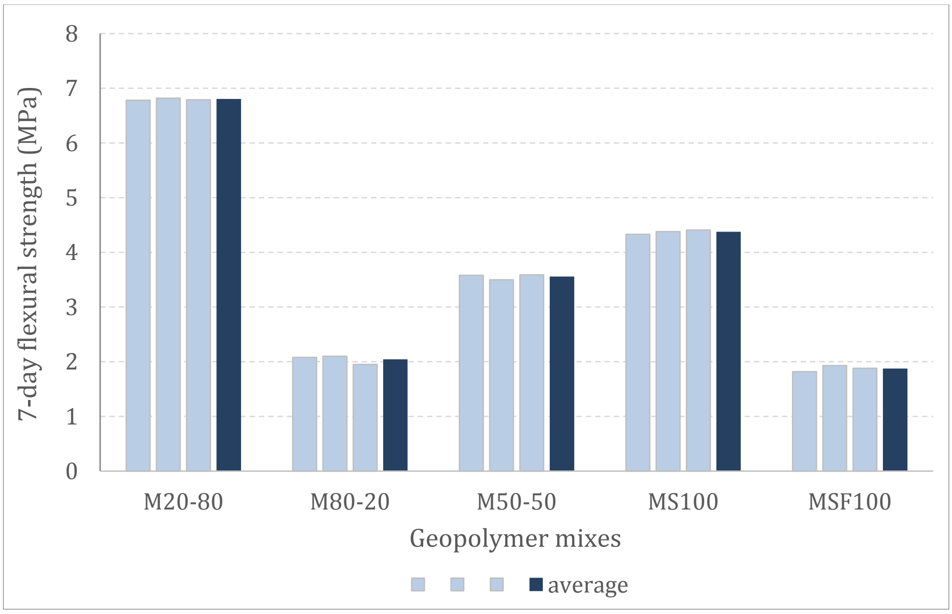

Fig. 17. 7-day flexural strength for oven temperature.

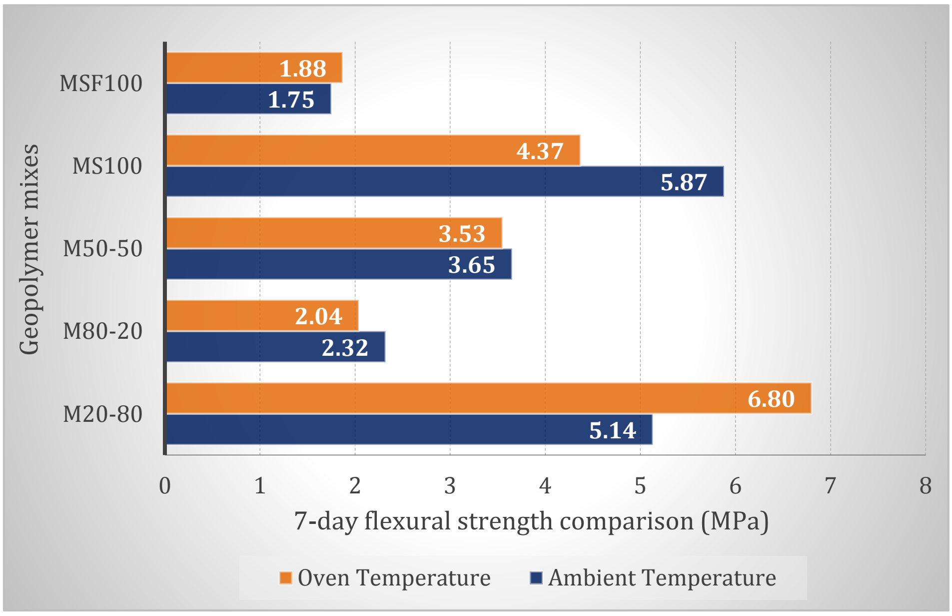

Fig. 18. 7-day flexural strength comparison.

The 28-day flexural strength results of the samples cured in ambient temperature are shown in Fig. 19. The flexural strength values ranged between 1.78 to 6.63 MPa. The maximum flexural strength value was recorded for the mix of M20-80 that considered 49.2%, 33.4%, 8.14% and 73.15% higher than M80-20, M50-50, MS100 and MSF100, respectively. However, the 28-day flexural strength results of the samples cured in oven temperature were in the range between 2.14–6.85 MPa. The maximum flexural strength was for the mix of M20-80 and the minimum flexural strength value was for the mix of MSF100. The maximum flexural strength of M20-80 was 68.3%, 38.2%, 18.4% and 68.7% higher than M80-20, M50-50, MS100 and MSF100, respectively.

The comparison between the 28-day flexural strength results of oven and ambient curing methods are shown on Fig. 21. The flexural strength values of the mixes MS100, M50-50 and M80-20 in which the curing of ambient method is used show significant increment in the flexural strength compared to the same mixes cured in oven temperature. The increment in flexural strength of the ambient curing method was 8.2%, 4% and 35.6% higher for the mixes of MS100, M50-50 and M80-20, compared to the oved curing method, respectively. However, the flexural strength value of the mix of M20-80 and MSF100 cured in oven temperature shows increment compared to the ambient temperature curing method. The increment in flexural strength of the oven curing method was 3.3% and 20.2% higher for the mixes of M20-80 and MSF100, compared to the oved curing method, respectively.

Table 6. 28-day flexural strength values.

Curing method	28-day flexural strength (MPa)				
	M20-80	M80-20	M50-50	MS100	MSF100
Ambient temperature	6.65	3.37	4.39	6.05	1.78
	6.62	3.40	4.41	6.12	1.82
	6.64	3.36	4.43	6.10	1.79
Average	6.64	3.38	4.41	6.09	1.80
Oven temperature (65 °C)	6.85	2.15	4.23	5.62	2.10
	6.87	2.18	4.18	5.58	2.18
	6.83	2.20	4.20	5.57	2.15
Average	6.85	2.18	4.20	5.59	2.14

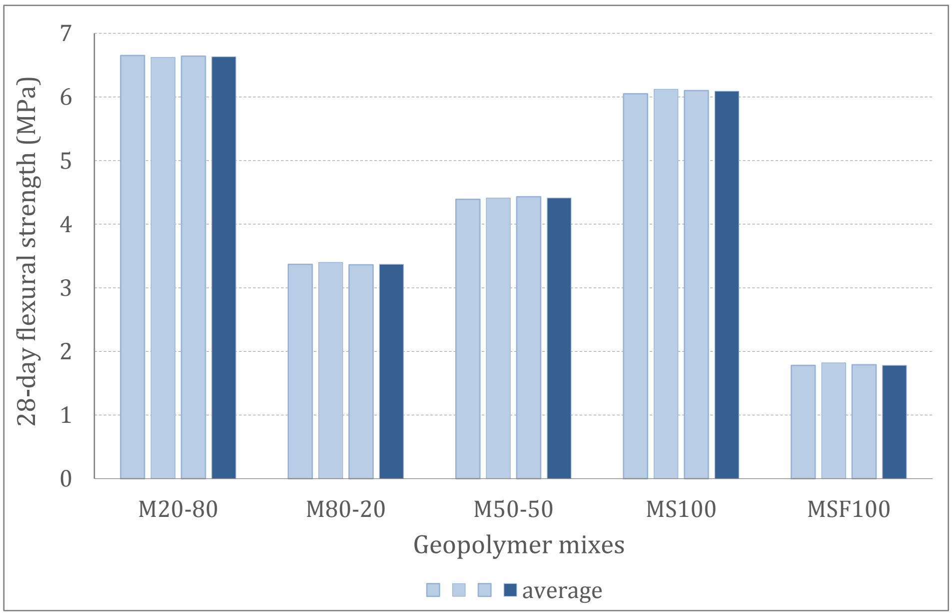

Fig. 19. 28-day flexural strength for ambient temperature.

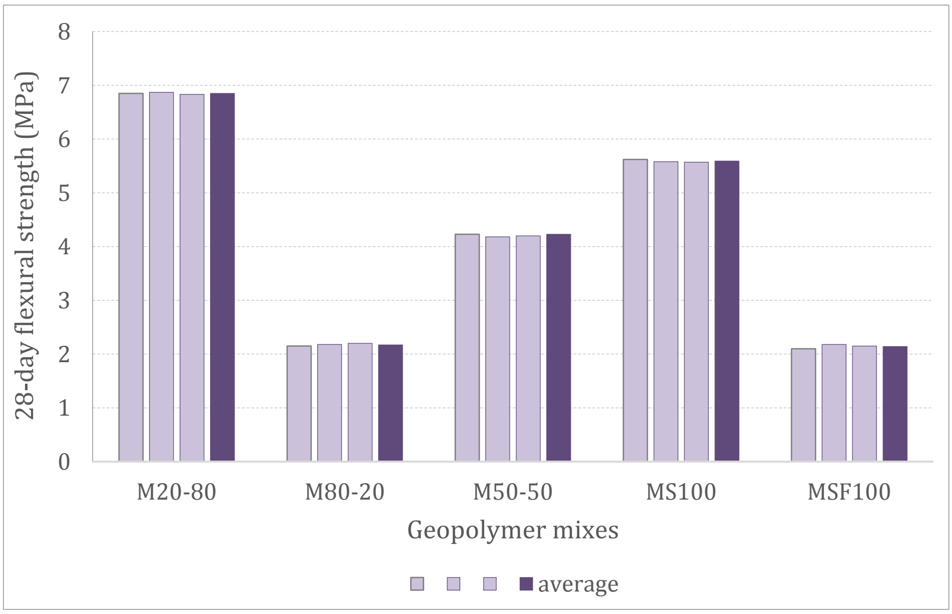

Fig. 20. 28-day flexural strength for oven temperature.

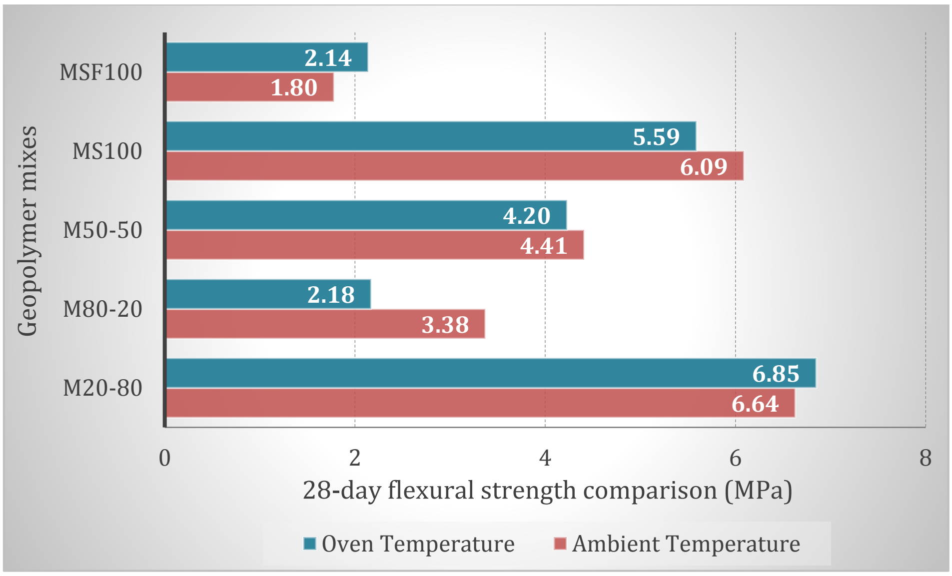

Fig. 21. 28-day flexural strength comparison.

6. Conclusions

This study aims to investigate the effect of using different minerals admixtures on the engineering properties of geopolymer mortar, and the effect of curing method of GM on the engineering properties of concrete. For the purpose of this study, five different mixes were prepared, each utilizing various mineral admixtures in different ratios: M20-80 (20% SF and 80% GGBS), M80-20 (80% SF and 20% GGBS), M50-50 (50% SF and 50% GGBS), MS100 (100% GGBS), MSF100 (100% SF).The curing methods for each sample were investigated separately under ambient and oven temperatures (65 °C) for 7 and 28 days to determine the final values of compressive and flexural strength.

Based on the experimental work and test results, the following conclusions were derived:

- The twenty-eight-day ambient temperature curing method, the maximum compressive strength values were recorded for the mix of M20-80, which is 27.9%, 26.5%, 14.5% and 72.8% higher than M80-20, M50-50, MS100 and MSF100, respectively. The maximum flexural strength values were recorded for the mix of M20-80, which is 49.2%, 33.4%, 8.14% and 73.15% higher than M80-20, M50-50, MS100 and MSF100, respectively.
- The twenty-eight-day oven temperature curing method, the maximum compressive strength values were recorded for the mix of M20-80, which is 61.3%, 44.3%, 26.75% and 70.2% higher than M80-20, M50-50, MS100 and MSF100, respectively. The maximum flexural strength values were recorded for the mix of M20-80, which is 68.3%, 38.2%, 18.4% and 68.7% higher than M80-20, M50-50, MS100 and MSF100, respectively.
- The results revealed that the compressive strength values of the mixes of MS100, M50-50 and M80-20 in which the curing of ambient method is used show significant increment compared to the same mixes cured in oven temperature. The increment in compressive strength of the ambient curing method was 14.4%, 25.8% and 46.4% for the mixes of MS100, M50-50 and M80-20, compared to the oved curing method, respectively.
- The flexural strength values of the mixes MS100, M50-50 and M80-20 in which the curing of ambient method is used show significant increment in the flexural strength compared to the same mixes cured in oven temperature. The increment in flexural strength of the ambient curing method was 8.2%, 4% and 35.6% higher for the mixes of MS100, M50-50 and M80-20, compared to the oved curing method, respectively.
- In summary, the results highlight the significant impact of different mineral admixtures and curing methods on the mechanical properties of geopolymer mortar, the mix of M20-80 demonstrating superior performance across various conditions.

Acknowledgements

None declared.

Funding

The authors received no financial support for the research, authorship, and/or publication of this manuscript.

Conflict of Interest

The authors declared no potential conflicts of interest with respect to the research, authorship, and/or publication of this manuscript.

Author Contributions

All of the authors made substantial contributions to conception and design, or acquisition of data, or analysis and interpretation of data; were involved in drafting the manuscript or revising it critically for important intellectual content; and gave final approval of the version to be published.

Data Availability

The datasets created and/or analyzed during the current study are not publicly available, but are available from the corresponding author upon reasonable request.

REFERENCES

Abutaha F, Abdul Razak H, Ibrahim H (2017). Effect of coating palm oil clinker aggregate on the engineering properties of normal grade concrete. *Coatings*, 7(10), 175.

Abutaha F, Abdul Razak H, Kanadasan J (2016). Effect of palm oil clinker (POC) aggregates on fresh and hardened properties of concrete. *Construction and Building Materials*, 112, 416–423.

Akbar A, Liew KM (2021). Multicriteria performance evaluation of fiber-reinforced cement composites: An environmental perspective. *Composites Part B: Engineering*, 218, 108937.

Al-Bakri AMM, Kamarudin H, Bnhussain M, Khairul Nizar I, Rafiza AR, Zarina Y (2012). The processing, characterization, and properties of fly ash based geopolymer concrete. *Reviews on Advanced Materials Science*, 30, 90–97.

Al-Safi S, Altharehi A, Alameri I, Al-Jolahy A (2025). The mechanical properties of cement mortar reinforced with silica fume subjected to sulfate and chloride environment. *Challenge Journal of Structural Mechanics*, 11(1), 55–69.

Alcan H, Aksu Alcan B, Bayrak B, Aydın A (2023). Potential improvement of clinker sand in the mechanical high temperature and transport properties with GGBS-based prepacked geopolymer composite. *Challenge Journal of Structural Mechanics*, 9(3), 92–106.

Aleem MIA, Arumairaj PD (2012). Geopolymer concrete - a review. *International Journal of Engineering Sciences and Emerging Technologies*, 1(2), 118–122.

Alnahhal MF, Alengaram UJ, Jumaat MZ, Abutaha F, Alqedra MA, Nayaka RR (2018). Assessment on engineering properties and CO2 emissions of recycled aggregate concrete incorporating waste products as supplements to Portland cement. *Journal of Cleaner Production*, 203, 822–835.

Boonserm K, Sata V, Pimraksa K, Chindaprasirt P (2012). Improved geopolymerization of bottom ash by incorporating fly ash and using waste gypsum as additive. *Cement and Concrete Composites*, 34(7), 819–824.

Danish A, Ozbakkaloglu T, Ali Mosaberpanah M, Salim MU, Bayram M, Yeon JH, Jafar K (2022). Sustainability benefits and commercialization challenges and strategies of geopolymer concrete: A review. *Journal of Building Engineering*, 58, 105005.

Deb PS, Sarker PK, Barbhuiya S (2016). Sorptivity and acid resistance of ambient-cured geopolymer mortars containing nano-silica. *Cement and Concrete Composites*, 72, 235–245.

Duxson P, Lukey GC, van Deventer JSJ (2006). Thermal evolution of metakaolin geopolymers: Part 1 – Physical evolution. *Journal of Non-Crystalline Solids*, 352(52–54), 5541–5555.

Duxson P, Fernández-Jiménez A, Provis JL, Lukey GC, Palomo A, van Deventer JSJ (2007a). Geopolymer technology: the current state of the art. *Journal of Materials Science*, 42(9), 2917–2933.

Duxson P, Lukey GC, van Deventer JSJ (2007b). The thermal evolution of metakaolin geopolymers: Part 2 – Phase stability and structural development. *Journal of Non-Crystalline Solids*, 353(22–23), 2186–2200.

EN 196-1 (2016). Methods of testing cement - Part 1: Determination of Strength. European Committee for Standardization, Brussels.

Fernández-Jiménez A, Palomo A (2003). Characterisation of fly ashes. Potential reactivity as alkaline cements. *Fuel*, 82(18), 2259–2265.

Hussin MW, Bhutta MAR, Azreen M, Ramadhansyah P J, Mirza J (2015). Performance of blended ash geopolymer concrete at elevated temperatures. *Materials and Structures*, 48(3), 709–720.

Ibrahim HA, Abdul Razak H, Abutaha F (2017). Strength and abrasion resistance of palm oil clinker pervious concrete under different curing method. *Construction and Building Materials*, 147, 576–587.

Khan MA, Memon SA, Farooq F, Javed MF, Aslam F, Alyousef R (2021). Compressive strength of fly-ash-based geopolymer concrete by gene expression programming and random forest. *Advances in Civil Engineering*, 2021, 6618407.

Kong DLY, Sanjayan JG (2010). Effect of elevated temperatures on geopolymer paste, mortar and concrete. *Cement and Concrete Research*, 40(2), 334–339.

Krivenko PV, Kovalchuk GYu (2007). Directed synthesis of alkaline aluminosilicate minerals in a geocement matrix. *Journal of Materials Science*, 42(9), 2944–2952.

Luhar S, Nicolaides D, Luhar I (2021). Fire resistance behaviour of geopolymer concrete: An overview. *Buildings*, 11(3), 82.

Mathew G, Joseph B (2018). Flexural behaviour of geopolymer concrete beams exposed to elevated temperatures. *Journal of Building Engineering*, 15, 311–317.

Mehta A, Siddique R (2017). Properties of low-calcium fly ash based geopolymer concrete incorporating OPC as partial replacement of fly ash. *Construction and Building Materials*, 150, 792–807.

Mucsi G, Szenczi Á, Nagy S (2018). Fiber reinforced geopolymer from synergetic utilization of fly ash and waste tire. *Journal of Cleaner Production*, 178, 429–440.

Nagajothi S, Elavenil S (2021). Effect of GGBS addition on reactivity and microstructure properties of ambient cured fly ash based geopolymer concrete. *Silicon*, 13(2), 507–516.

Narayanan A, Shanmugasundaram P (2017). An experimental investigation on flyash-based geopolymer mortar under different curing regime for thermal analysis. *Energy and Buildings*, 138, 539–545.

Narwade R, Jadhav R (2025). Concrete strength monitoring and damage detection using piezoelectric-based wireless sensor. *Challenge Journal of Concrete Research Letters*, 16(1), 40–50.

Qaidi SMA, Sulaiman Atrushi D, Mohammed AS, Unis Ahmed H, Faraj RH, Emad W, Tayeh BA, Mohammed Najm H (2022). Ultra-high-performance geopolymer concrete: A review. *Construction and Building Materials*, 346, 128495.

Rangan BV (2014). Geopolymer concrete for environmental protection. *The Indian Concrete Journal*, 88(4), 41–59.

Rashad AM, Zeedan SR (2011). The effect of activator concentration on the residual strength of alkali-activated fly ash pastes subjected to thermal load. *Construction and Building Materials*, 25(7), 3098–3107.

Shehata N, Mohamed OA, Sayed ET, Abdelkareem MA, Olabi AG (2022). Geopolymer concrete as green building materials: Recent applications, sustainable development and circular economy potentials. *Science of the Total Environment*, 836, 155577.

Shukor Lim NHA, Samadi M, Ariffin NF, Hussin MW, Rafique Bhutta MA, Sarbini NN, Abd Khalid NH, Aminuddin E (2018). Effect of curing conditions on compressive strength of FA-POFA-based geopolymer mortar. *IOP Conference Series: Materials Science and Engineering*, 431, 092007.

Singh B, Ishwarya G, Gupta M, Bhattacharyya SK (2015). Geopolymer concrete: A review of some recent developments. *Construction and Building Materials*, 85, 78–90.

Srivastava A, Mishra A, Singh S (2025). Mechanical and durability study of nano-SiO_2 and nano-TiO_2 on fiber reinforced concrete. *Challenge Journal of Concrete Research Letters*, 16(1), 33–39.

Sumajouw DMJ, Hardjito D, Wallah SE, Rangan BV (2007). Fly ash-based geopolymer concrete: study of slender reinforced columns. *Journal of Materials Science*, 42(9), 3124–3130.

Urtekin Y, Çelik Z (2025). Investigation of the effects of re-curing on mechanical properties of basalt-polypropylene hybrid fiber concretes after exposure to high temperature. *Challenge Journal of Structural Mechanics*, 11(1), 14–23.

Van Chanh N, Trung BD, Van Tuan DM (2008). Recent research geopolymer concrete. *The 3rd ACF International Conference-ACF/VCA*, Vietnam, vol.18, 235–241.

Wasim M, Ngo TD, Law D (2021). A state-of-the-art review on the durability of geopolymer concrete for sustainable structures and infrastructure. *Construction and Building Materials*, 291, 123381.

Zhao J, Tong L, Li B, Chen T, Wang C, Yang G, Zheng Y (2021). Eco-friendly geopolymer materials: A review of performance improvement, potential application and sustainability assessment. *Journal of Cleaner Production*, 307, 127085.

Challenge Journal of Concrete Research Letters (2025) 16(2) 85–94

Challenge Journal of Concrete Research Letters

Research Article

Effect of dimensions of specimens on the impact performance of concrete

Mohammed Gamal Al-Hagri [a,*], Shahed Husni Ben Issa Ebribesh [a],
Fares Alamoudi [a], Abdulrahman Rakan Al Haj Ali [a]

[a] *Department of Civil Engineering, İstanbul Aydın University, 34295 İstanbul, Türkiye*

ABSTRACT

Mechanical properties of concrete are size dependent. While many reports have discussed the size effect of the test specimen on the static properties of concrete, research on the effect of cross-sectional dimensions of the concrete beams on its impact performance is still scarce. This research experimentally evaluates the relationship between the cross-sectional dimensions and orientation of the concrete beam specimens on their impact performance. Repetitive drop-weight test was used to evaluate the impact energy absorption capacity of different concrete beams. A loading protocol to evaluate the impact energy of concrete beams having different cross-sectional dimensions was proposed. The results revealed that the impact performance of concrete is size dependent. Strong proportional relationships between the moment of inertia, cross-sectional area and impact energy were found. As the moment of inertia and cross-sectional area of the test specimen increase, its impact energy exponentially increases. Furthermore, a linear proportional relationship was found between the normalized impact energy and the normalized cross-sectional area × moment of inertia. This means that the impact performance of concrete beams depends on both their cross-sectional area and orientation. The proposed loading protocol has been proven to be able to accurately evaluate the impact energy of concrete specimens with significantly varying impact performance while importantly saving time.

ARTICLE INFO

Article history:

Received	– February 8, 2025
Revision requested	– April 11, 2025
Revision received	– April 20, 2025
Accepted	– May 2, 2025

Keywords:
Concrete
Dimensions of specimens
Drop-weight test
Impact performance
Orientation of specimens

Citation: Al-Hagri MG, Ebribesh SHBI, Alamoudi F, Al Haj Ali AR (2025). Effect of dimensions of specimens on the impact performance of concrete. *Challenge Journal of Concrete Research Letters*, 16(2), 85–94.

1. Introduction

Cement-based materials are the most used materials in the building industry. Global demand on such materials production is expected to further increase due to the increasing infrastructure development (Arif et al. 2020; Döndüren and Al-Hagri 2022). Understanding the properties of concrete under different conditions is critical to understand the behavior of buildings under various critical loading conditions. One of the most critical loading conditions that a structure might be subjected to is the impact loading condition. Impact load is a medium to high-strain rate type of loading that happens over a very short period. The criticality of the loading condition increases as its loading velocity, and accordingly strain rate, increases. During the impact actions, a huge amount of energy is imparted on the structure. This might lead to catastrophic results. This type of load might be created by many sources such as explosions, ballistic projectiles, and collisions of objects (Al-Hagri et al. 2024). Behavior of concrete under impact loads is the least understood compared to its behavior under other loading conditions. Since concrete is a strain-rate material, its properties under static loading cannot be directly used to evaluate its behavior under impact loading. While under static loads cracks tend to propagate through the weakest paths, under impact loads cracks might propagate through strong zones such as aggregate particles.

---

* *Corresponding author.* Tel.: +90-444-1-428 ; E-mail address: malhagri@aydin.edu.tr (M. G. Al-Hagri)

ISSN: 2548-0928 / DOI: https://doi.org/10.20528/cjcrl.2025.02.004

Some concrete properties such as mechanical properties are size dependent. This means that as the size of the test specimen changes, the obtained strength of concrete changes too. For this reason, standards usually specify the size of the test specimen that should be used to evaluate certain static properties of concrete. However, standards don't provide much information regarding the specimen size that should be used to evaluate the impact performance of concrete, especially under flexural impact loading. This is why different sizes of specimens have been used in literature to evaluate the impact performance of concrete. However, it is thought that change in the dimensions of the specimen might result in a change in the obtained results. Some examples of the used dimensions for beam specimens to evaluate the impact performance of concrete are presented in Table 1.

Table 1. Some examples of used beam specimen dimensions to evaluate impact strength of concrete.

Width (mm)	Height (mm)	Length (mm)	Loaded span (mm)	Reference
100	100	400	300	Cao et al. (2018); Wu et al. (2015); Yoo et al. (2015); Yu et al. (2025)
100	100	400	350	Zaki et al. (2021)
100	100	500	400	Al-Tayeb et al. (2012); Reda Taha et al. (2008)
80	100	400	300	Al-Hagri and Döndüren (2023, 2025); Bin Cai et al. (2024); Döndüren and Al-Hagri (2023)
70	70	260	210	Abid et al. (2021)
150	150	710	590	Kantar et al. (2011); Yılmaz et al. (2014)
100	50	400	300	Al-Tayeb et al. (2013a, 2013b)
50	50	750	690	Demirhan et al. (2019)

Although the size effect of concrete specimen on the static properties of concrete has been previously investigated by many studies such as (Brake et al. 2016; del Viso et al. 2008; Jiang et al. 2024; Mena-Alonso et al. 2024; Narayanan 2024; Visairo-Méndez et al. 2019; Yoo et al. 2016; Yu et al. 2025; Zi et al. 2014), only a limited number of studies have discussed the effect of dimensions of specimens on the impact performance of concrete. Li et al. (2018) investigated the specimen size effect on the compressive dynamic strength of concrete cylinders and cubes. The results showed that impact strength of concrete is affected by the size and shape of the test specimen. Lee et al. (2015) investigated the effect of cylinder size on the dynamic modulus of elasticity and compressive strength of concrete. They found that while the size of specimen didn't have a remarkable effect on the static and dynamic compressive strength and modulus of elasticity of normal strength concrete, it had a high effect in the case of high strength concrete. Krauthammer et al. (2003) and Elfahal et al. (2005) studied the size effect of normal strength and high-strength concrete cylinders respectively on the compressive impact strength of concrete. Their results showed that the behavior of concrete under impact loading is size dependent and is different from that known for static loading.

When the literature was explored, it was found that studies on the effect of dimensions of specimens on the impact behavior of concrete are very limited. Moreover, most of the published reports have focused on the size effect of cylindrical specimens on the compressive impact strength of concrete. However, according to (Bindiganavile and Banthia 2006), the flexural response of plain concrete is more size dependent than the compressive response under static and dynamic loading. Up to the best knowledge of the authors, only three studies could be found in the literature (Bindiganavile and Banthia 2006; Murali et al. 2022; Yoo and Banthia 2017) on the effect of dimensions of the concrete beams on their flexural impact strength. In all these studies, only three different sizes of prismatic beams were examined. By Murali et al. (2022), the impact behavior of preplaced aggregated fibrous concrete beam specimens having dimensions of 100×100×400 mm^3, 50×50×250 mm^3, and 150×150×550 mm^3 was investigated. By Yoo and Banthia (2017), the effect of beam dimensions (50×50×250 mm^3, 100×100×400 mm^3, 150×150×550 mm^3) on the impact strength of ultra-high-performance fiber-reinforced concrete beams was evaluated. By Bindiganavile and Banthia (2006), prismatic concrete beams with different dimensions (50×50×450 mm^3, 100×100×350 mm^3, 150×150×500 mm^3) were tested under drop-weight test. However, in the later study, repetitive impact test was not considered. This highlights the necessity of the current study.

In the current study, the effect of dimensions and orientation of concrete beams having different shapes (prismatic and cylindrical) on the impact performance of concrete have been experimentally evaluated using drop-weight test. Seven different beam cross-sectional dimensions and orientations have been examined. The relationship between moment of inertia (I), cross-sectional area (A), and impact energy (E) has been investigated. Moreover, a loading protocol to evaluate the impact performance of concrete specimens having varying sizes have been proposed and evaluated.

2. Experimental Program

2.1. Preparation of specimens

To evaluate the size effect of concrete specimens on the impact strength of concrete, concrete beams having different dimensions were produced. While the length of the concrete specimens was kept constant as 400 mm, the width (b) and the height (h) of the beams were changed. All beams have a loaded span of 300 mm. Seven different cross-sectional dimensions were evaluated within the scope of this study. All produced concrete beams were tested using drop-weight test. Details of the evaluated beam specimens are shown in Table 2.

Table 2. Details of the test specimens.

Specimen code	Specimen type	Dimensions (h×b×L) (mm)	Section orientation
S50×50	Prismatic	50×50×400	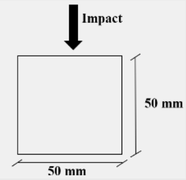
S50×100	Prismatic	50×100×400	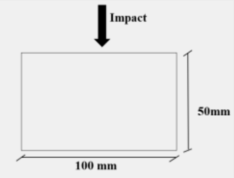
S100×50	Prismatic	100×50×400	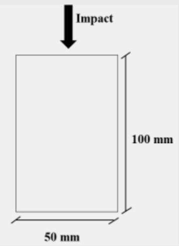
S150× 150	Prismatic	150×150×400	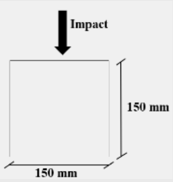
S150×100	Prismatic	150×100×400	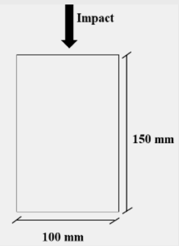
S100×150	Prismatic	100×150×400	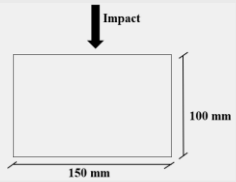
S110	Cylindrical	110×400	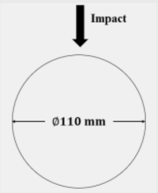

As can be seen from the table, prismatic beam specimens having six different width and height dimensions ranging from 50 mm to 150 mm were tested. Moreover, cylindrical beam specimens having a diameter of 110 mm were also evaluated. On average three samples were prepared and tested for each different cross-sectional size. It can be seen from the table that a unique specimen code was assigned to each group of specimens according to their cross-sectional dimensions.

In the code, the first number refers to the height of the specimen while the second one represents the width. For the cylindrical specimens, only one number representing the diameter of the cross-section was used.

In order to experimentally determine the compressive strength of concrete, three cylinders having a height of 300 mm and a diameter of 150 mm were also produced. After 24 hours of pouring the concrete into the proper molds, test specimens were demolded and put inside the curing tanks as presented in Fig. 1(a). All samples were tested after 28 days. The prepared test samples are shown in Fig. 1(b).

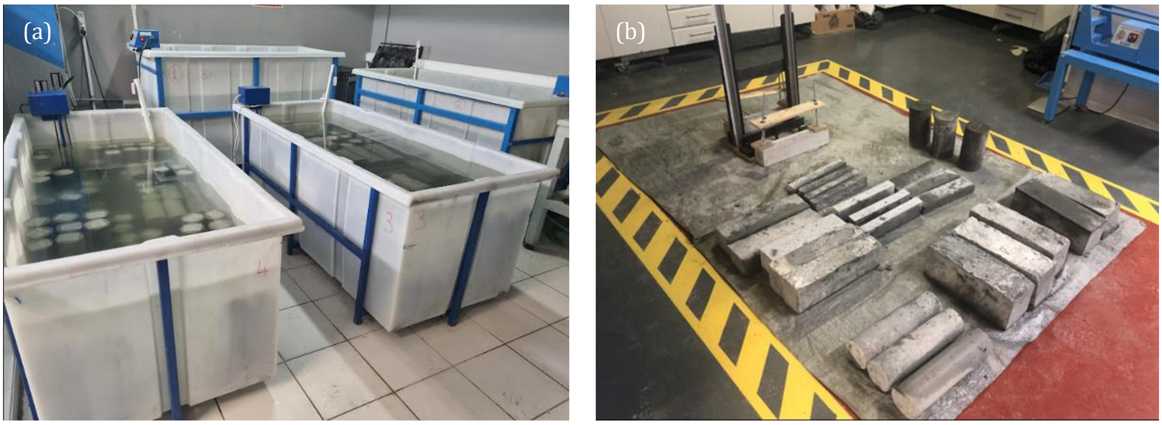

Fig. 1. Test specimens: (a) Inside the curing tanks; (b) After the curing process.

2.2. Procedure and testing

The impact strength of concrete beam specimens was evaluated using drop-weight impact test. For this reason, a proper drop weight impact test device was produced first. Some images of the production process of the device are presented in Fig. 2. Details of the prepared impact test device is shown in Fig. 3(a). The test device consists of two rails made of frictionless steel linear shaft having a high wear resistance and covered with chrome. The total length of the rails is 1 m each and the diameter is 25 mm. The shafts are tied to aluminum plates that support the rails and can be used for connection purposes. The rails are connected to a wooden frame that is used as support. To connect the impact hammer to the linear shafts, two bearings were used at the sides of the impact hammer. These bearings help minimize the loss of energy due to friction while allowing the impact hammer to move freely in the vertical direction. Considering the height of the test samples and the height of the hammer impact tip, an impact height of up to 70 cm can be obtained.

Impact hammers having different weights can be attached to the test unit. Since the impact performance of the prepared concrete beams was expected to greatly vary between the beams with small cross-sections and the bigger ones, two steel impact hammers were initially prepared. The weight of the smaller hammer is 1.49 kg, while the weight of the heavier one is 3.09 kg. The diameter of the impact tip of these impact hammers is 15 mm and 24 mm respectively. During the tests, it was found that bigger beams necessitated a heavier impact hammer, for this reason, extra weights were attached to the 3.09 kg impact hammer to increase its weight up to 5.20 kg. The used impact hammers are shown in Fig. 3.

To stop the test specimens from overturning and movement during the test, two reinforced concrete beams were produced and used as supports. As can be seen from Fig. 3, two threaded tie rods are put at each end of each RC beam. Using a proper wooden piece at each side, the samples are held tight in their position during the impact test.

The impact performance of the concrete beams was evaluated using the cumulative impact energy (E). The impact energy is calculated as $E = \sum mgh$, where m is the impact hammer weight (kg), g is the gravitational acceleration (9.81 m/s^2), and h is the impact height (m). The average impact energy of three specimens was calculated and reported.

Since a great variance between the impact energy of the smaller and bigger concrete beams is expected, and to save time, a proper loading protocol should be used. For this purpose, the following loading protocol was proposed. This loading protocol depends on gradually increasing the potential impact energy until failure of the sample. The potential impact energy was increased by gradually increasing the impact height first and then by increasing the impact weight. At first, the lighter impact hammer was used to hit the samples from a height of 10 cm for a maximum of 10 drops. If the sample passes this loading step and didn't fail, the impact height was increased by 10 cm. The impact test continued for a maximum of another 10 drops. If the samples pass this loading step too, the impact height was increased by another 10 cm. The process continued until the maximum impact height (i.e., 70 cm) was reached. After that, the lighter impact hammer was replaced by the 3.09 kg hammer. Impact test continued from a height of 10 cm. After that, the impact height was increased by 10 cm at each step. A maximum of ten impacts were used in each step. When the maximum height was reached again, the impact process continued for 100 hits in this loading step. If the sample didn't fail within this process, extra weight was added to the 3.09 kg impact hammer to increase its weight to 5.20 kg. The impact test then continued by using this heavier impact hammer from a height of 70 cm until the complete fracture of the sample. This loading protocol was used considering the loading protocols reported in (Cao et al. 2022; Hrynyk 2013), where the applied impact energy was changed during the impact test of RC specimens. This type of loading protocol is believed to better evaluate the impact performance of samples with greatly varying impact capacities while importantly saving time.

Fig. 2. Production of the impact test device.

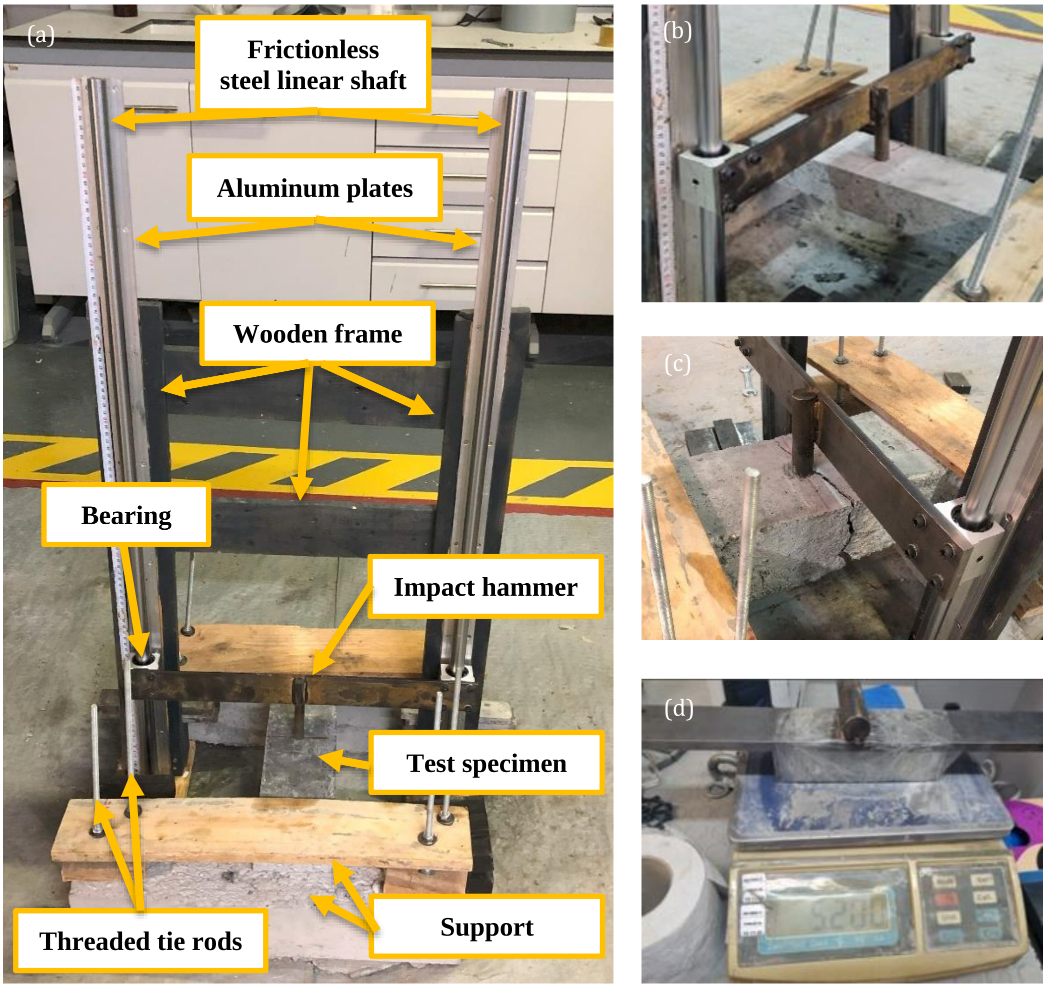

Fig. 3. Impact test set-up:
(a) drop-weight test device; (b) 1.49 kg impact hammer; (c) 3.09 kg impact hammer; (d) 5.20 kg impact hammer.

3. Results and Discussion

The compressive strength test (Fig. 4) was performed using three cylindrical samples. The average compressive strength was found to be 43.74 MPa. Repetitive drop-weight impact test (Fig. 5) was used to evaluate the impact strength of concrete beam specimens. The test results are presented in Table 3. In the table, the average impact energy of concrete beams was reported. It was found that all the tested samples showed a brittle failure. This means that the samples fractured directly without showing any visible cracks before failure. It also means that they did not show any elasto-plastic behavior. This brittle failure was found for all the tested samples, regardless of their sizes and shapes. Some images of fracture samples after the end of the impact test are presented in Fig. 6.

It's worth mentioning that this brittle behavior under impact loading can be shifted to a more ductile one by the incorporation of some additive materials into concrete such as fibers (Al-Hagri and Döndüren 2025) and tire rubbers (Döndüren and Al-Hagri 2023). It's also worth mentioning that not all additive materials have this capability. Some additive materials such as nano additives don't change the brittle behavior of concrete (Al-Hagri and Döndüren 2023).

Fig. 4. Compressive strength test of concrete.

Fig. 5. Impact test of concrete.

Table 3. Impact test results

Specimen code	Moment of inertia (I) (cm^4)	Cross-sectional area (A) (cm^2)	Impact energy up to failure (N·m)
S50×50	52.1	25	48.24
S50×100	416.7	50	26.31
S100×50	104.2	50	65.78
S150×150	4218.8	225	35,126.77
S150×100	2812.5	150	2,997.99
S100×150	1250.0	150	4,953.17
S110	718.7	95	43.85

Fig. 6. Fractured test samples.

The results revealed that while small impact hammer (1.49 kg) was sufficient to break samples with moment of inertia less than 750 cm^4 and cross-sectional area less than 100 cm^2, samples with higher A and I necessitated a higher weight to save the experimental time. In this case, the heavier impact hammer 3.09 kg was used. Moreover, some samples such as (S150×150 and S100×150) required an even heavier impact hammer. This is why during the test the authors attached extra weight to the 3.09 kg hammer increasing its weight to 5.20 kg. This indicates the efficiency of the proposed loading protocol. It is thought that using of the lighter weight hammer (1.49 kg) from a height of 10 cm would have necessitated a huge number of impacts to fracture the bigger beams. For example, if this loading step is the only one that is used for fracturing S150×150 beams, more than 24000 drops might have been necessary to produce the 35126.77 N·m impact energy that is necessary to fracture the samples. Which would have necessitated a lot of time to be achieved. On the other hand, if the heavy weight hammer (5.20 kg) from a height of 70 cm was used for all the beams specimens, samples with small cross- sectional dimensions might have failed from the first impact drop. This means that the impact energy of these small samples would have been inaccurately evaluated. This is a clear indication of the efficiency of the proposed loading protocol in accurately evaluating the impact performance of samples with different impact performances while remarkably saving experimental time.

It should be noted that there are some impact tests that can be used to evaluate the impact performance of concretes having varying impact performance such as the Charpy impact test. However, the Charpy impact test unit is much more expensive than the impact test device manufactured and used in the current study. The drop-weight test device used in this study costs approximately USD $50, which can be afforded by most research teams if not all. Moreover, this test device is very easy to manufacture. The loading protocol adapted in the current study can add up to the cost efficiency advantage of the drop-weight impact test device by making it efficient to test concretes with remarkably varying impact performances. Accordingly, a cost-efficient simple test procedure can be used to evaluate the impact performance of such concretes. A comparison between the proposed loading protocol and the use of the Charpy impact test can be investigated in future research.

As can be seen from Table 3, the impact performance of concrete is a size dependent property. To evaluate this relationship, the relationship between the impact energy and the moment of inertia is graphically presented in Fig. 7. As can be seen from the figure, the impact performance of concrete increased as the moment of inertia increased. Increasing the moment of inertia of the member increases its stiffness and toughness and accordingly its impact absorption capacity (Al-Hagri et al. 2024). An exponential relationship between the moment of inertia and the impact energy was found. The coefficient of determination (R^2), which gives an idea about the quality of the found relationship, has a very high value of 0.98. When the value of R^2 gets higher than 0.7, it represents a high-quality relationship. The higher the value is the higher quality it is (Al-Hagri and Döndüren 2025; Döndüren and Al-Hagri 2023; Gupta et al. 2015; Nakipoglu et al. 2022; Rahmani et al. 2012). This is a clear indication that the found relationship has a high quality and can be used to represent the relationship between the considered variables (i.e. impact energy and moment of inertia).

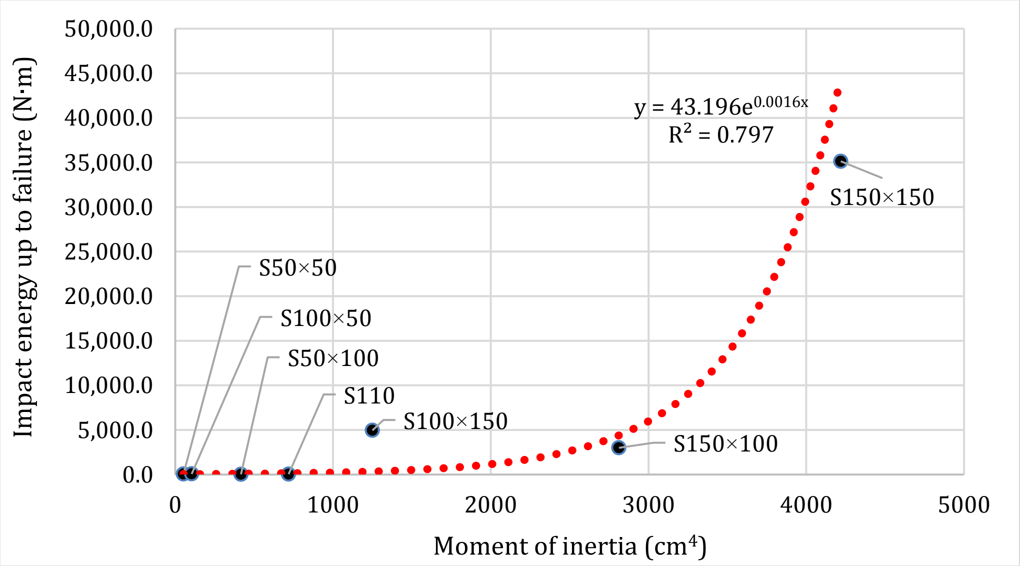

Fig. 7. Relationship between the moment of inertia and impact energy of concrete specimens.

On the other hand, the relationship between the impact energy and the cross-sectional area of the concrete beams was also evaluated. This relationship is presented in Fig. 8. The results showed that as the cross-sectional area of the beam increases, its impact performance increases. An exponential relationship between the cross-sectional area of the beam and the impact energy was found. This relationship has a value of R^2 close to 1. In general, as the cross-sectional area increases, the moment of inertia increases improving impact flexural strength of the beam, allowing it to absorb a higher impact energy.

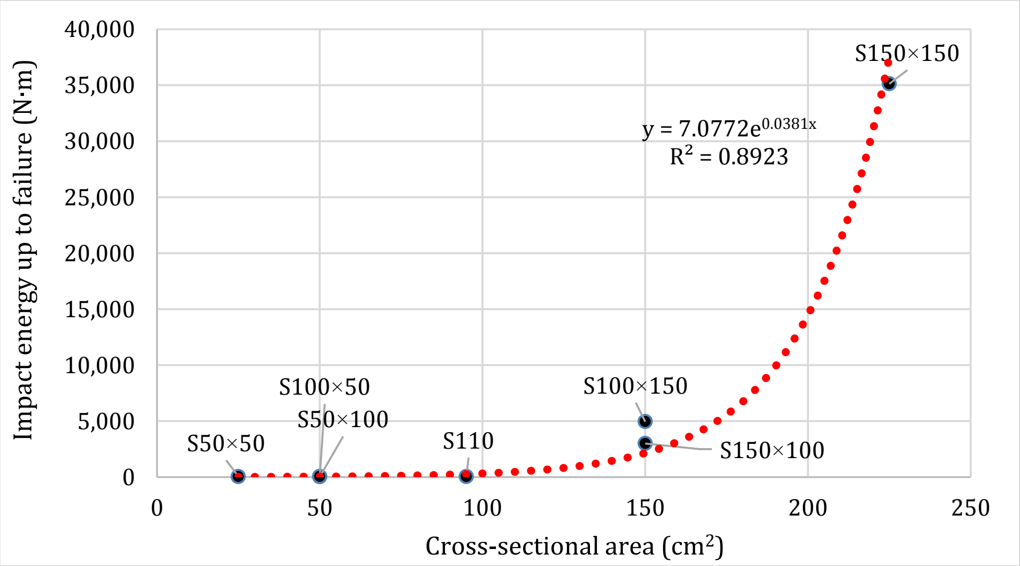

Fig. 8. Relationship between the cross-sectional area and impact energy of concrete specimens.

The results showed that the impact energy absorption capacity of concrete is a size dependent property that has a relationship with both the moment of inertia and the cross-sectional area of the test specimen. To evaluate the overall relationship between these three parameters, the relationship between the normalized impact energy and the normalized moment of inertia × the cross-sectional area (i.e., *I*×*A*) is graphically presented in Fig. 9. The normalized values were calculated taking the sample with the least cross-sectional area (i.e., S50×50) as the reference sample.

As can be seen from Fig. 9, there is a strong linear relationship with a value of $R^2 = 0.88$ between the normalized impact energy and normalized *I*×*A* of the concrete beams. This indicates that the impact performance of concrete greatly depends on both the moment of inertia and the cross-sectional area of the test specimen. These two properties are interconnected properties of the members. While the cross-sectional area depends on the dimensions of the cross-section, the moment of inertia depends on the dimensions and orientation of the cross-section.

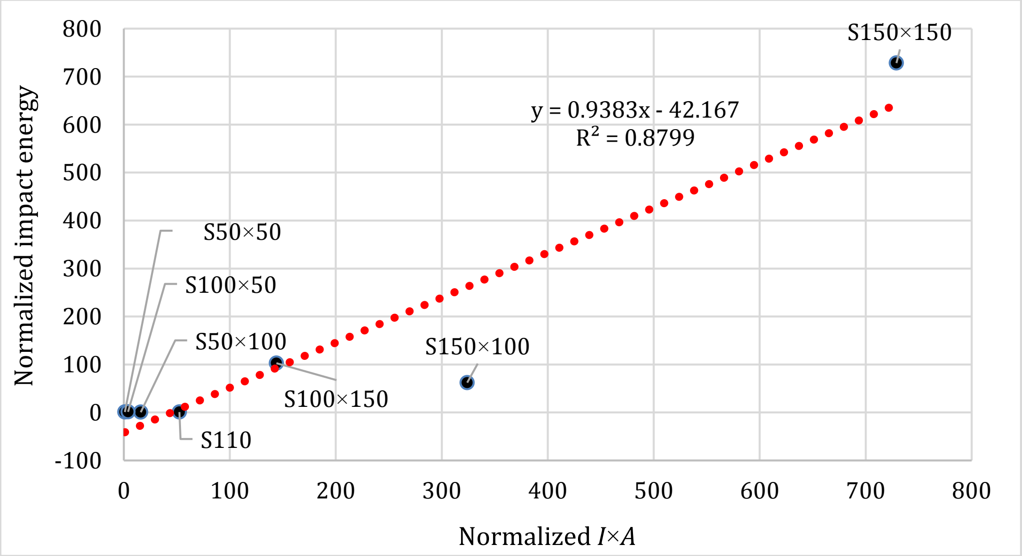

Fig. 9. Relationship between normalized cross-sectional area × moment of inertia (*I*×*A*) and normalized impact energy.

4. Conclusions

This research represents an experimental evaluation of the effect of the cross-sectional dimensions and orientation of concrete beams on their impact performance. Concrete beams with seven different cross-sectional dimensions and orientations have been tested under drop-weight test. A loading protocol for the repetitive impact test of samples having remarkably varying sizes has been proposed and validated. It was found that impact performance of concrete is a size dependent property. Increasing the moment of inertia and cross-sectional area of the concrete beams increased its impact performance. Increasing the moment of inertia of the sample increases its toughness and stiffness and accordingly its impact absorption capacity. Exponential relationships were found between the impact energy and both the moment of inertia and the cross-sectional area of the concrete beams. Moreover, a linear proportional relationship between the normalized impact energy and the normalized cross-sectional area × moment of inertia (*I*×*A*) was found. This indicates that the impact performance of concrete depends on both the cross-sectional area and the moment of inertia of the test beam (i.e., dimensions and orientation of the beam).

It is worth mentioning that while standards provide details on the dimensions of the standard samples that should be used in the evaluation of some mechanical properties under quasi-static loading, they generally don't provide much information regarding the standard dimensions of beam specimens under impact loading. Different cross-sectional dimensions and sizes have been used in the literature to evaluate the flexural impact performance of concrete. This indicates the necessity of more future research on this regard. This research provided some relationships between the cross-sectional dimensions and the impact performance of concrete. However, more research is still necessary. The size dependence of impact performance might depend on some other properties of concrete such as the compressive strength and the existence of additive materials. This hypothesis can be experimentally assessed in future research.

REFERENCES

Abid SR, Gunasekaran M, Ali SH, Kadhum AL, Al-Gasham TS, Fediuk R, Vatin N, Karelina M (2021). Impact performance of steel fiber-reinforced self-compacting concrete against repeated drop weight impact. *Crystals*, 11(2), 91.

Al-Hagri MG, Döndüren MS (2023). Experimental study on static and impact properties of concrete incorporating different nanoparticles in single and combined forms. *Magazine of Concrete Research*, 76(8), 1–35.

Al-Hagri MG, Döndüren MS (2025). Effect of single and hybrid incorporation of steel, polypropylene and polyethylene terephthalate fibres on the properties of concrete under static and impact loading. *Magazine of Concrete Research*, 77(9–10), 488–507.

Acknowledgements

None declared.

Funding

The authors received no financial support for the research, authorship, and/or publication of this manuscript.

Conflict of Interest

The authors declared no potential conflicts of interest with respect to the research, authorship, and/or publication of this manuscript.

Author Contributions

All of the authors made substantial contributions to conception and design, or acquisition of data, or analysis and interpretation of data; were involved in drafting the manuscript or revising it critically for important intellectual content; and gave final approval of the version to be published.

Data Availability

The datasets created and/or analyzed during the current study are not publicly available, but are available from the corresponding author upon reasonable request.

Al-Hagri MG, Döndüren MS, Yılmaz T, Anıl Ö, Erol H, Şengel HS (2024). Low-velocity impact behavior of two-way SFRC slabs strengthened with steel plate. *Archives of Civil and Mechanical Engineering*, 24(3), 144.

Al-Tayeb MM, Abu Bakar BH, Ismail H, Akil HM (2012). Impact resistance of concrete with partial replacements of sand and cement by waste rubber. *Polymer-Plastics Technology and Engineering*, 51(12), 1230–1236.

Al-Tayeb MM, Abu Bakar BH, Akil HM, Ismail H (2013a). Performance of rubberized and hybrid rubberized concrete structures under static and impact load conditions. *Experimental Mechanics*, 53(3), 377–384.

Al-Tayeb MM, Abu Bakar BH, Ismail H, Akil HM (2013b). Effect of partial replacement of sand by recycled fine crumb rubber on the performance of hybrid rubberized-normal concrete under impact load: experiment and simulation. *Journal of Cleaner Production*, 59, 284–289.

Arif M, Al-Hagri MG, Shariq M, Rahman I, Hassan A, Baqi A (2020). Mechanical properties and microstructure of micro- and nano-additives-based modified concrete composites: A sustainable solution. *Journal of the Institution of Engineers (India): Series A*, 101(1), 89–104.

Bin Cai, Lu S, Fu F (2024). Behavior of steel fiber-reinforced coal gangue concrete beams under impact load. *Engineering Structures*, 314, 118306.

Bindiganavile V, Banthia N (2006). Size effects and the dynamic response of plain concrete. *Journal of Materials in Civil Engineering*, 18(4), 485–491.

Brake NA, Allahdadi H, Adam F (2016). Flexural strength and fracture size effects of pervious concrete. *Construction and Building Materials*, 113, 536–543.

Cao M, Li L, Zhang C, Feng J (2018). Behaviour and damage assessment of a new hybrid-fibre-reinforced mortar under impact load. *Magazine of Concrete Research*, 70(17), 905–918.

Cao Y, Alyousef R, Baharom S, Shah SNR, Alaskar A, Alabduljabbar H, Mustafa Mohamed A, Assilzadeh H (2022). Dynamic attainment of mixed aspect ratio for concrete members reinforced with steel fiber under impact loading. *Mechanics of Advanced Materials and Structures*, 29(14), 1986–1995.

del Viso JR, Carmona JR, Ruiz G (2008). Shape and size effects on the compressive strength of high-strength concrete. *Cement and Concrete Research*, 38(3), 386–395.

Demirhan S, Yıldırım G, Banyhussan QS, Koca K, Anıl Ö, Erdem RT, Şahmaran M (2019). Impact behaviour of nano-modified deflection-hardening fibre reinforced concretes. *Magazine of Concrete Research*, 72(17), 865-887.

Döndüren MS, Al-Hagri MG (2022). A review of the effect and optimization of use of nano-TiO_2 in cementitious composites. *Research on Engineering Structures and Materials*, 8(2), 283–305.

Döndüren MS, Al-Hagri MG (2023). Single and combined effect of fine and coarse tire rubbers on the static, microstructural, and impact properties of concrete. *Strength of Materials*, 55(5), 1055–1078.

Elfahal MM, Krauthammer T, Ohno T, Beppu M, Mindess S (2005). Size effect for normal strength concrete cylinders subjected to axial impact. *International Journal of Impact Engineering*, 31(4), 461–481.

Gupta T, Sharma RK, Chaudhary S (2015). Impact resistance of concrete containing waste rubber fiber and silica fume. *International Journal of Impact Engineering*, 83, 76–87.

Hrynyk T (2013). Behaviour and Modelling of Reinforced Concrete Slabs and Shells Under Static and Dynamic Loads. *Ph.D. thesis*, University of Toronto, Toronto, Canada.

Jiang N, Ge Z, Wang Z, Gao T, Zhang H, Ling Y, Šavija B (2024). Size effect on compressive strength of foamed concrete: Experimental and numerical studies. *Materials and Design*, 240.

Kantar E, Erdem RT, Anıl Ö (2011). Nonlinear finite element analysis of impact behavior of concrete beam. *Mathematical and Computational Applications*, 16(1), 183–193.

Krauthammer T, Elfahal MM, Lim J, Ohno T, Beppu M, Markeset G (2003). Size effect for high-strength concrete cylinders subjected to axial impact. *International Journal of Impact Engineering*, 28(9), 1001–1016.

Lee BJ, Kee SH, Oh T, Kim YY (2015). Effect of cylinder size on the modulus of elasticity and compressive strength of concrete from static and dynamic tests. *Advances in Materials Science and Engineering*, 2015, 580638.

Li M, Hao H, Shi Y, Hao Y (2018). Specimen shape and size effects on the concrete compressive strength under static and dynamic tests. *Construction and Building Materials*, 161, 84–93.

Mena-Alonso Á, González DC, Mínguez J, Vicente MA (2024). Size effect on the flexural fatigue behavior of high-strength plain and fiber-reinforced concrete. *Construction and Building Materials*, 411, 134424.

Murali G, Abid S, Vatin N (2022). Experimental and analytical modeling of flexural impact strength of preplaced aggregate fibrous concrete beams. *Materials*, 15(11), 3857.

Nakipoglu A, Al-Hagri MG, Döndüren MS (2022). Effect of column cross section and concrete compressive strength on the resistance of RC columns subjected to axial loads and loads created by creep. *NOHU Journal of Engineering Sciences*, 11(4), 999–1005.

Narayanan S (2024). Effect of size and shape of test specimen on compressive strength of concrete. *Concrete International*, 46(1), 45–51.

Rahmani T, Kiani B, Shekarchi M, Safari A (2012). Statistical and experimental analysis on the behavior of fiber reinforced concretes subjected to drop weight test. *Construction and Building Materials*, 37, 360–369.

Reda Taha MM, El-Dieb AS, Abd El-Wahab MA, Abdel-Hameed ME (2008). Mechanical, fracture, and microstructural investigations of rubber concrete. *Journal of Materials in Civil Engineering*, 20(10), 640–649.

Visairo-Méndez R, Torres-Acosta AA, Alvarado-Cárdenas R (2019). Specimen size effect on the durability indexes determination for cement-based materials. *Revista ALCONPAT*, 9(3), 288–302.

Wu M, Chen Z, Zhang C (2015). Determining the impact behavior of concrete beams through experimental testing and meso-scale simulation: I. Drop-weight tests. *Engineering Fracture Mechanics*, 135, 94–112.

Yılmaz MC, Anıl Ö, Alyavuz B, Kantar E (2014). Load displacement behavior of concrete beam under monotonic static and low velocity impact load. *International Journal of Civil Engineering*, 12(4), 488–503.

Yoo DY, Banthia N (2017). Size-dependent impact resistance of ultra-high-performance fiber-reinforced concrete beams. *Construction and Building Materials*, 142, 363–375.

Yoo D-Y, Yoon Y-S, Banthia N (2015). Flexural response of steel-fiber-reinforced concrete beams: Effects of strength, fiber content, and strain-rate. *Cement and Concrete Composites*, 64, 84–92.

Yoo DY, Banthia N, Kang ST, Yoon YS (2016). Size effect in ultra-high-performance concrete beams. *Engineering Fracture Mechanics*, 157, 86–106.

Yu L, Wang G, Ren T, Yang T, Chen Q, Song M (2025). Study on compressive size effect of rock-filled concrete considering initial pores. *Structures*, 71, 108030.

Zaki RA, AbdelAleem BH, Hassan AAA, Colbourne B (2021). Impact resistance of steel fiber reinforced concrete in cold temperatures. *Cement and Concrete Composites*, 122, 104116.

Zi G, Kim J, Bažant ZP (2014). Size effect on biaxial flexural strength of concrete. *ACI Materials Journal*, 111(3), 319–326.

CHALLENGE JOURNAL OF CONCRETE RESEARCH LETTERS (2025) 16(2) 95–114

Challenge Journal of Concrete Research Letters

Research Article

Behavior of multi-cell steel columns under impact loading

Kamel Kandil [a], Mostafa El-Shami [a], Ghada Mousa Hekal [a,*], Osama Magdy ElGouhary [a]

[a] *Department of Civil Engineering, Menoufia University, Shebin ElKoum, 6132711 Menofia, Egypt*

ABSTRACT

This study investigates the behavior of multi-cell steel columns (MCCs) under impact loading through both experimental and numerical analysis. Twelve specimens, including single-cell columns (SCC) and four-cell MCC configurations, were tested in empty and concrete-filled conditions. The specimens were categorized into three groups based on a fixed height-to-width ratio (*R*). A nonlinear finite element model was developed using ABAQUS and validated against experimental data. Key parameters, including peak deflection, failure modes, deflection-time relationships, maximum impact forces, energy absorption and the rectangularity ratio effect, were examined to provide insights into impact-resistant structural design. The results demonstrate that the internal partitioning of the column into cells significantly reduces local buckling under impact loading by enhancing the section's local stiffness. In addition, internal partitioning improves energy absorption for empty models. On the other hand, concrete-filled models do not show the same behavior although concrete filling significantly improves resistance to impact forces. The results also provides that increase of the *R* ratio results in an increase in impact force and a decrease in mid-point displacement. For empty single-cell columns, an increase in *R* results in a decrease in energy absorption, which may be due to energy dissipation through local buckling under the falling impactor. These findings contribute to the advancement of impact-resistant column designs for applications in structural and transportation engineering.

ARTICLE INFO

Article history:

Received	– February 25, 2025
Revision requested	– April 21, 2025
Revision received	– May 2, 2025
Accepted	– May 12, 2025

Keywords:
Multi-cell columns
Energy absorption
Impact loading
Finite element modeling

Citation: Kandil K, El-Shami M, Hekal GM, ElGouhary OM (2025). Behavior of multi-cell steel columns under impact loading. *Challenge Journal of Concrete Research Letters*, 16(2), 95–114.

1. Introduction

Columns are essential structural elements, and their failure can lead to catastrophic consequences. Among various cross-sectional designs, tubular sections have demonstrated outstanding performance under compression, bending, and torsion. Their superior mechanical properties, combined with an aesthetically appealing shape, have made them widely applicable in structural engineering. Tubular sections are commonly used in buildings, bridges, barriers, offshore structures, and towers, among other applications (Wardenier 2001; Wardenier et al. 2010).

When tubular sections have insufficient wall thickness to support the required loads, filling the hollow section with concrete is a proven method to enhance strength. Several studies have investigated the behavior of concrete-filled tubular columns under compression loading, such as the studies conducted by Campbell (1994), Guler et al. (2013), Chu (2014), Patil and Mohite (2014), Bedage and Shinde (2015), and Kirankumar et al. (2016).

As vertical structural elements, columns are particularly vulnerable to environmental hazards such as impact, wind, and earthquakes. Among these, impact loading generates highly localized pressure, often exceeding the intensity of other hazards. This has driven growing research interest in understanding the behavior of empty and concrete-filled hollow sections under impact loading to develop more resilient design methods. Sean-

---

* *Corresponding author.* E-mail address: gahda.mousa@sh-eng.menofia.edu.eg (G. M. Hekal)

ISSN: 2548-0928 / DOI: https://doi.org/10.20528/cjcrl.2025.02.005

gatith (1997) presented an extensive experimental program and finite element analysis on FRP composite box beams subjected to impact loads, testing 48 simply supported beams while varying impact velocity, striker mass, span length, and wall thickness. Finite element modeling was performed using LS-DYNA3D. Similarly, Bambach et al. (2008) presented experimental program and finite element analysis of hollow and concrete-filled steel beams subjected to large-mass, low-velocity lateral impacts at mid-span. Yousuf et al. (2010) conducted a comprehensive test program to investigate the impact performance of pre-compressed stainless-steel concrete-filled steel tube (CFST) columns. Their study compared stainless steel column with mild steel column and analyzed the behavior of in-filled tubes under both impact and pre-compressive loads. Al-Thairy (2012) investigated the behavior of axially compressed steel columns under vehicle impact, using ABAQUS/Explicit for numerical modeling, conducting a parametric study, developing a simplified vehicle model, proposing an analytical method for column response, and evaluating design provisions. Yousuf et al. (2012) presented an experimental and numerical investigation on the behaviour of hollow and concrete-filled tubular columns from mild steel subjected to static and impact loading. Experimental and numerical results obtained by ABAQUS/Explicit program were compared. Additionally, the impact response of concrete-filled tubes was compared with that of hollow section tubes. Zhu et al. (2018) investigated the lateral impact resistance of rectangular hollow steel tubes and those partially filled with concrete, demonstrating that concrete effectively mitigates local buckling. Hou et al. (2018) conducted a finite element analysis to evaluate the life-cycle behavior of concrete-filled steel tubes (CFST) subjected to pre-loading, residual stress, and lateral impact. Yang et al. (2019) and Zhu et al. (2023) investigated the impact force, deformation, and failure modes of high-strength concrete-filled steel tubular (HSCFST) members under lateral impact, highlighting their superior impact resistance. Feng et al. (2022) conducted transverse continuous impact tests on cantilevered square CFST columns, examining the effects of impact mass and height. Their results demonstrated a positive correlation between cumulative plastic displacement and stiffness degradation with repeated impacts. Overall, previous research indicates that hollow tubular sections are prone to local deformations under impact loading. However, when these sections are filled with concrete, local deformations are significantly restricted, enhancing their ability to withstand greater lateral impact forces. Uslu et al. (2024) investigated 70 circular columns, which included both concrete-filled and hollow steel tubes, under axial loading. The study varied key parameters, such as concrete compressive strength (f_c), diameter-to-thickness (D/t), and length-to-diameter (L/D) ratios. Results showed that the ultimate axial load increased with higher f_c and D/t, but decreased with higher L/D. The findings were consistent with Eurocode 4, and finite element modeling slightly overestimated the axial capacity by about 5%.

Another effective solution to mitigate local buckling in hollow steel columns is the use of internal continuous stiffeners. These stiffeners reduce the likelihood of buckling in the outer shell by dividing the column into multiple smaller sections, known as cells, forming what is referred to as a multi-cell column (MCC).

Although research on MCCs as structural elements remains limited, their widespread use as energy absorbers in mechanical engineering has highlighted their potential advantages. This has drawn attention to their possible application as an alternative to concrete-filled tubular (CFT) columns, particularly in structures subjected to dynamic loads, where enhanced energy absorption is a highly desirable characteristic.

Numerous researchers have investigated the behavior of multi-cell columns (MCCs). Zhang et al. (2006) conducted analytical and numerical studies on the axial crushing of square MCCs, revealing that dividing a single-cell column into a 3×3 cell configuration increased its energy absorption by 50%. Similarly, Krolak et al. (2007, 2009) demonstrated that internally partitioning a column into multiple cells enhanced its load-carrying capacity and improved its buckling behavior. Bi et al. (2010) performed nonlinear finite element crash simulations on aluminum foam-filled single- and triple-cell hexagonal columns, showing that triple-cell composite columns exhibited greater crushing forces due to the corner effect. Song et al. (2012) conducted finite element analysis on axially loaded tubes with square, hexagonal, and octagonal cross-sections featuring origami-inspired patterns. The results revealed that these patterned tubes exhibited reduced initial peak forces and demonstrated more consistent and stable crushing behavior compared to traditional tubular designs. Yin et al. (2014) explored the energy absorption characteristics of foam-filled multi-cell thin-walled structures (FMTSs) through LS-DYNA simulations, while Sofi (2015), Wu et al. (2016), and Ahmed et al. (2017) examined the application of multi-cell thin-walled tubes in crashworthiness structures. Their findings consistently indicated that multi-cell thin-walled structures outperform single-cell structures in energy absorption. The energy absorption performance of MCCs is largely influenced by their shape and geometry. Yin et al. (2015) found that FMTSs with nine cells exhibited the best crashworthiness characteristics, while Ahmed et al. (2017) demonstrated that curvy stiffeners significantly improved energy absorption by increasing the mean crushing force and crush force efficiency compared to conventional configurations. Hassam et al. (2020) conducted experimental and finite element (FE) simulations on four multi-cell cross-shaped CFST stub columns, comparing their performance with existing CFST design formulas. Their results showed that these formulas underestimated the axial compressive capacity of cross-shaped CFST columns. Further investigations by Hassam et al. (2022) on ten multi-cell cross-shaped CFST columns examined key parameters such as slenderness ratio, width-to-thickness ratio of the steel tube, and load eccentricity. They found that the multi-cell configuration significantly improved concrete confinement. Yang et al. (2021) experimented with rectangular steel tubes and U-shaped steel plates to create three-cell cross-shaped steel tubes, testing nine slender columns under axial compression. Their findings indicated that increasing limb length enhanced load-bearing capacity while reducing ductility. More recently, Zheng et al. (2024) tested six stub columns under axial compression, varying cross-section form and concrete strength. Their results provided insights into failure patterns, ultimate strength, load-strain behavior, compressive stiffness, and ductility. They concluded that using longitudinal stiffeners or multi-cell configurations improves the axial compressive strength, stiffness, and ductility of cross-shaped CFST columns, further reinforcing the superior mechanical performance of multi-cell designs.

Previous research in this field has primarily focused on the behavior of axially loaded MCCs. To the best of the authors' knowledge, no prior studies have examined the response of MCCs to lateral impact loading. However, Tran et al. (2014) and Tran et al. (2015) theoretically investigated the behavior of multi-cell square tubes under oblique and axial impact loading, respectively.

In this study, a finite element (FE) model was developed using ABAQUS, a well-established and highly accurate finite element software, to analyze the response of both single-cell columns (SCCs) and multi-cell columns (MCCs) under lateral impact loading. Additionally, laboratory experiments were conducted on all specimens. A comparison between the numerical model and experimental results was performed, focusing on key parameters such as mid-point displacement and deformed shape. Further comparative analyses were conducted across all specimens, considering factors such as the rectangularity ratio of the cross-section (R), internal partitioning of the column into multiple cells, and concrete filling. The results, including mid-point displacement, impact force, energy absorption, and failure modes, were observed and discussed in detail.

2. Experimental Models and Test Setup

2.1. Specification of the tested specimens

Twelve specimens were prepared for testing, categorized into three groups. Each group consisted of two single-cell column (SCC) specimens—one filled with concrete (F) and the other empty (E)—and two multi-cell column (MCC) specimens, also with one filled (F) and one empty (E). Each group maintained a fixed height-to-width ratio ($R=h/b$), while all specimens shared the same cross-sectional area.

The total column length was 2860 mm, with an effective length of 2500 mm. Table 1 provides a detailed overview of the model dimensions, R ratios for each group, and the concrete filling conditions of the sections.

Table 1. Description of the tested specimens.

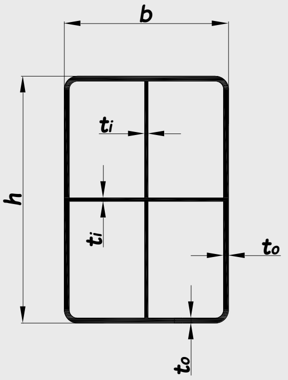

R	Condition	Dimensions (mm)				Concrete filling
		b	h	t_o	t_i	
1.00	SCC	100	100	5	–	E
						F
	MCC	100	100	4	2	E
						F
1.50	SCC	100	150	4	–	E
						F
	MCC	100	150	3	2	E
						F
2.25	SCC	100	225	3	–	E
						F
	MCC	100	225	2	2	E
						F

SCC: Single-cell column; MCC: Multi-cell column; E: Empty; F: Concrete-filled

2.2. Drop weight (impactor)

The drop weight was constructed from solid steel cylinders of varying diameters, welded together to form a unified mass. To ensure that the impact load was applied as a point load, the lower end of the drop weight was shaped into a conical section, as illustrated in Fig. 1. The total weight of the projectile was 57.85 kg.

2.3. Materials used for specimen fabrication

2.3.1. Concrete

A self-compacting concrete mix was used for specimen fabrication to facilitate placement and ensure complete filling of narrow sections, preventing voids and segregation.

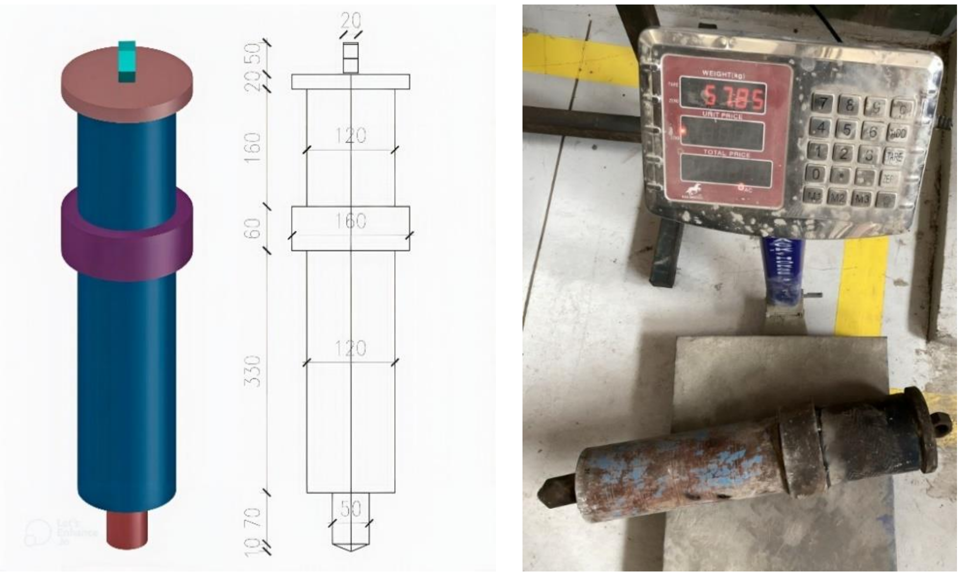

Fig. 1. Details of drop weight (impactor) (all dimensions are in mm).

Both the compressive and tensile strengths of the concrete mix were determined experimentally in accordance with the Egyptian Standard Specifications (ES1658-4/2008 and ISO1920-3:2004). The results showed a compressive strength of 46.3 MPa and a tensile strength of 4.08 MPa.

2.3.2. Material of steel tube and longitudinal stiffeners

The test specimens were fabricated using ST37 grade mild steel, with measured tensile strength (F_u) of 360 MPa and nominal yield strength (F_y) of 240 MPa.

2.4. Test setup and instrumentation

The tests in this study were conducted in the laboratory of the Institute of Concrete Structures Research at the Housing and Building National Research Center (HBRC). A custom-designed steel setup was used to support the tested specimens and provide the required end conditions. To ensure precise impact application, a PVC pipe with a diameter of 200 mm and a height of 3.00 meters was installed vertically at the center of each specimen. The pipe was secured using formwork to maintain vertical alignment and ensure that the load was applied precisely at the center of the sample. For a simply supported end condition, the columns were fully constrained in all displacement directions, effectively preventing any movement. In particular, displacement in the direction of the applied load was restricted. This restraint system included a U-shaped steel plate fixed to the support with bolts, as well as a steel rod to firmly secure the specimen, as illustrated in Fig. 2. The Linear Variable Differential Transformer (LVDT) device, shown in Fig. 3, was used to measure displacement over time, providing precise readings of the structure's deflection under both static and dynamic loads. Next, the specimen was positioned within the test setup, ensuring an effective span of 2500 mm. The LVDT device was placed directly beneath the center of the specimen to accurately record displacement data over time. Subsequently, a 57.85 kg impactor was released from a height of 3.3 meters through the PVC pipe, striking the specimen precisely at its center. The complete test setup is illustrated in Fig. 4.

3. Finite Element Modeling

To gain a deeper understanding of the behavior of multi-cell steel columns under impact loading, a finite element model was developed. In this study, ABAQUS/Explicit was used for analysis. ABAQUS/Explicit is a specialized analysis tool that employs an explicit dynamic finite element formulation. It is particularly well-suited for modeling short-duration, transient dynamic events such as impact and blast loads. Additionally, it efficiently handles highly nonlinear problems involving evolving contact conditions, such as forming simulations. The finite element models in this study were developed using the explicit nonlinear finite element code ABAQUS/Explicit. The following sections provide a detailed description of the FE model utilized in this research.

Fig. 2. Impact test support conditions.

Fig. 3. Displacement with time measurement device: (a) LVDT device; (b) Data logger and computer.

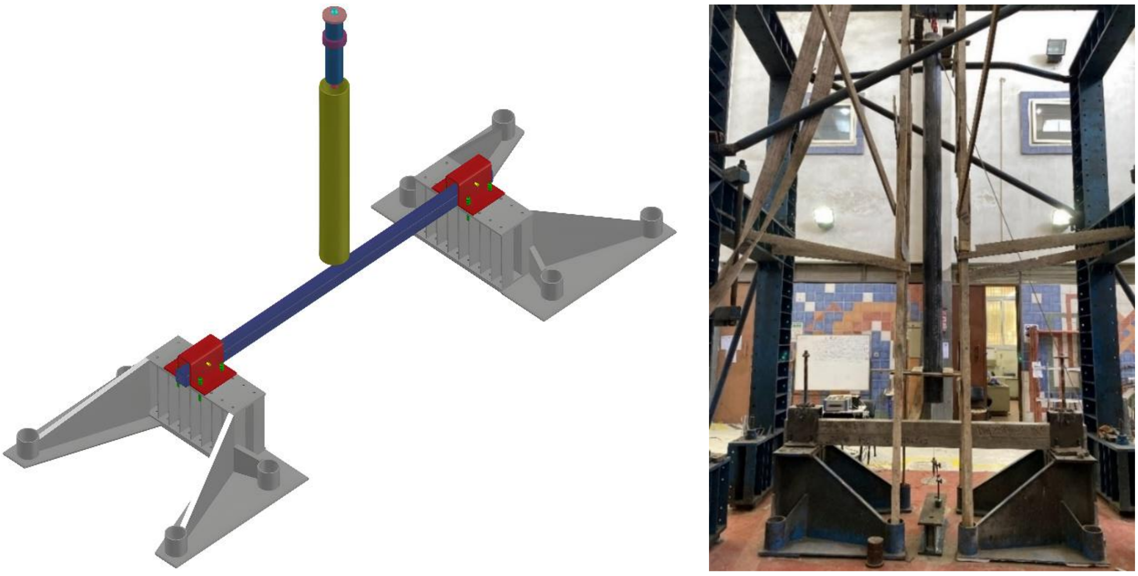

Fig. 4. Impact test setup.

3.1. Geometrical modeling

The steel tube and concrete were modeled using C3D8R elements, which are eight-node, reduced-integration solid elements. Each node of this element has three translational degrees of freedom, making it well-suited for defining contact surfaces necessary for applying impact loads. Additionally, it effectively integrates constitutive laws and is highly suitable for nonlinear dynamic analysis, allowing for finite strain and large-displacement rotations. A total of 7,752 elements were used to model the steel tube, while the concrete was represented by 24,168 elements. Meanwhile, the impactor was modeled as a rigid body using R3D4 elements and was discretized into 373 fine elements, as illustrated in Fig. 5.

Fig. 5. Mesh configuration of concrete-filled column under impact.

3.2. Material modeling

3.2.1. Material modeling of steel tube and longitudinal stiffeners

The modeling of the steel material requires defining the density, which was taken as 7,850 kg/m^3, the linear part in the stress-strain curve of steel and nonlinear part of the curve. The elastic properties are completely defined by giving the Young's modulus (E), and the Poisson's ratio (ν), the values of 210,000 MPa and 0.3 respectively.

The nonlinear part of the stress-strain curve of steel material was modeled using the PLASTIC option available in ABAQUS. It is used to describe the perfect plasticity or isotropic hardening behavior. Isotropic hardening means that the yield surface changes size uniformly in all directions such that the yield stress increases (or decreases) in all stress directions as plastic straining occurs. ABAQUS provides an isotropic hardening model, which is useful for cases involving gross plastic straining or in cases where the straining at each point is essentially in the same direction in strain space throughout the analysis. Although the model is referred to as a "hardening" model, strain softening or hardening followed by softening can be defined. If isotropic hardening is defined, the yield stress can be given as a tabular function of plastic strain and the yield stress at a given state is simply interpolated from the table of data. Since the buckling analysis involves large in-elastic strains, the nominal (engineering) static stress–strain curves were converted to true stress and logarithmic plastic true strain curves. The true stress (σ_{true}) and plastic true strain ($\varepsilon_{\mathrm{true}}^{\mathrm{pl}}$) were calculated using Eqs. (1) and (2) as given by ABAQUS. Figs. 6 and 7 show the relationship between the engineering and true stress strain curves.

$$\sigma_{true} = \sigma_{nom}\,(\,1 + \varepsilon_{nom}\,) \tag{1}$$

$$\varepsilon_{true}^{pl} = ln(\,1 + \varepsilon_{nom}\,) - \frac{\sigma_{true}}{E} \tag{2}$$

where E is the initial Young's modulus; σ_{true} is the true stress; σ_{nom} is the nominal stress; $\varepsilon_{\mathrm{true}}$ is the true strain; and $\varepsilon_{\mathrm{nom}}$ is the nominal strain.

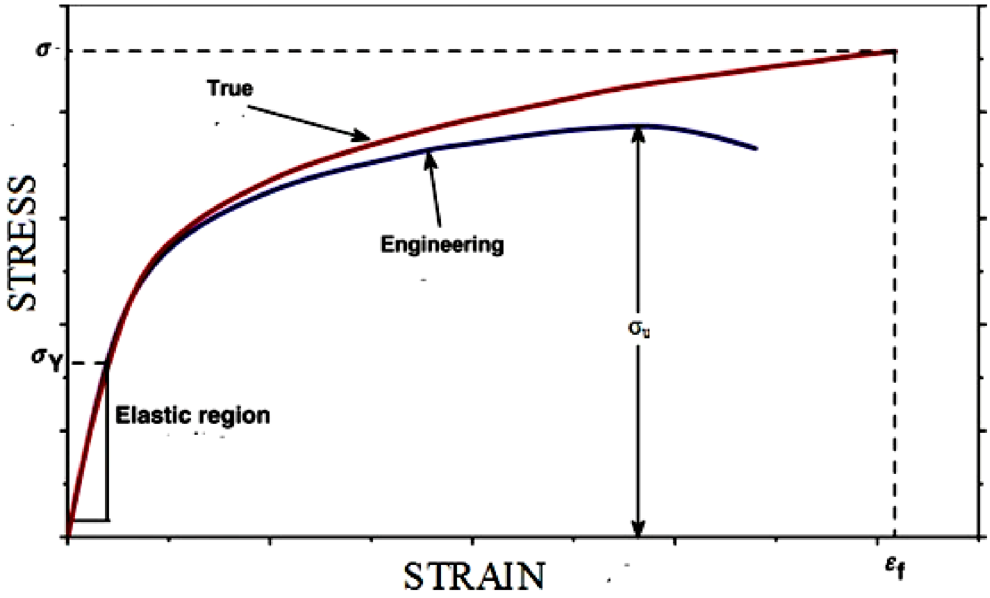

Fig. 6. The relationship between engineering and true stress-strain curves for steel (Elkady 2023).

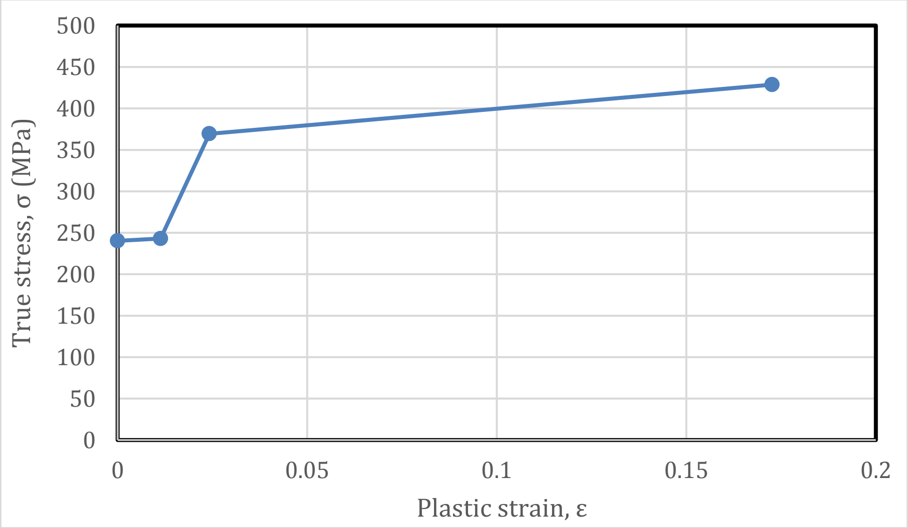

Fig. 7. True stress-plastic strain curve for ST37.

3.2.2. Material modeling of the confined concrete

Defining confined normal concrete requires specifying its density and stress-strain curve properties, which can be divided into two parts: elastic and plastic. The concrete material's mass density was defined using the DENSITY option in ABAQUS. The linear portion of the stress-strain curve was established using the ELASTIC option, where Young's modulus and Poisson's ratio (taken as 0.2) were specified to define the material's elastic behavior. The plastic behavior of concrete was modeled using the DRUCKER-PRAGER model in ABAQUS, which is widely used for simulating concrete and other quasi-brittle materials under various loading conditions, including cyclic loads. This model assumes that the primary failure mechanisms are tensile cracking and compressive crushing. The DRUCKER-PRAGER option was utilized to define a linear Drucker-Prager model with associated flow and isotropic hardening. The material parameters were set as follows: friction angle (β) = 20°, dilation angle (φ) = 35°, and the ratio of flow stress in triaxial tension to that in compression (K) = 0.8. The DRUCKER-PRAGER HARDENING option was used to define the equivalent uniaxial stress-strain curves for confined concrete. The confinement effect in concrete-filled box steel columns depends on the D/t ratio, where D is depth. Columns with a high D/t ratio provide weak confinement, leading to premature failure due to local buckling of the steel tubes. Conversely, columns with a low D/t ratio offer strong confinement due to increased thickness, enhancing the strength of the infill concrete and allowing it to be treated as confined concrete. The relationship between the equivalent uniaxial stress-strain curves for both unconfined and confined concrete is illustrated in Fig. 8, as presented by Ellobody et al. (2006), where f_c represents the unconfined concrete cylinder compressive strength, equal to 0.8×F_{cu}, and F_{cu} is the unconfined concrete cube compressive strength. The corresponding unconfined strain (ε_c) is taken as 0.003, as recommended by ACI specifications. Mander et al. (1988) proposed Eqs. (3) and (4) to describe stress-strain relationships, from which the confined concrete compressive strength (f_{cc}) and the corresponding confined strain (ε_{cc}) can be determined.

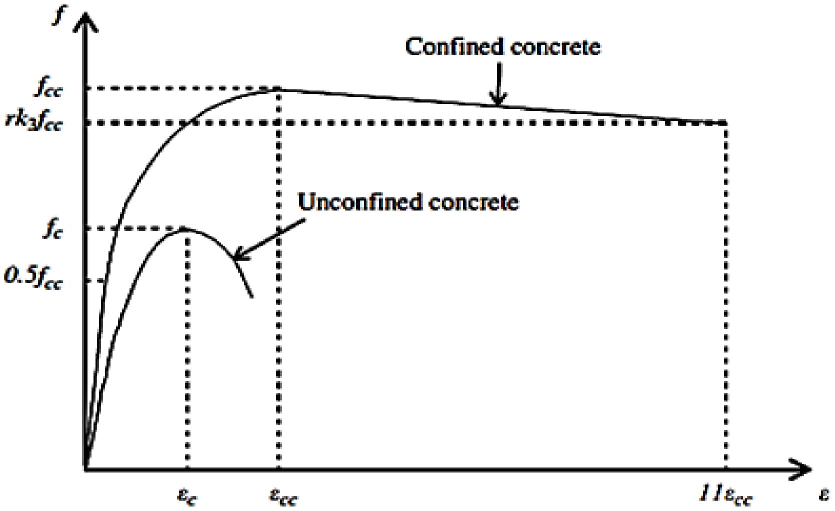

Fig. 8. Equivalent uniaxial stress-strain curve for confined and unconfined concrete (Ellobody et al. 2006).

$$f_{cc} = f_c + k_1 f_1 \tag{3}$$

$$\varepsilon_{cc} = \varepsilon_c(1 + k_2 \frac{f_1}{f_c}) \tag{4}$$

where f_1 is the confining pressure from steel tube that depends on the D/t ratio and the steel box yield stress; and k_1 and k_2 are coefficients that depend on lateral pressure and concrete mix.

Based on their tests, Richart et al. (1928) found the average values of those coefficients are k_1=4.1 and k_2=5k_1. Also, tests of Balmer (1949) showed that k_1 has an average value of 5.6, and increases by decreasing lateral pressures.

The approximate value of (f_1) can be obtained from empirical Eqs. (5) or (6) given by Hu et al. (2003), where f_{yd} is the yield strength of the steel tube.

$$f_1 / f_{yd} = 0.043646 - 0.000832(D/t)$$

$$21.7 \leq (D/t) \leq 47 \tag{5}$$

$$f_1 / f_{yd} = 0.006241 - 0.0000357(D/t)$$

$$47 \leq (D/t) \leq 150 \tag{6}$$

The stress strain relation diagram of concrete is also divided into three parts. The first part is the initially assumed elastic range to the proportional limit stress. The value of the proportional limit stress is taken as 0.5(f_{cc}) as given by Hu et al. (2003). The initial Young's modulus of confined concrete (E_{cc}) is reasonably calculated using the empirical Eq. (7) given by ACI 318-19 (2019).

$$E_{cc} = 4700\sqrt{f_{cc}} \quad \text{(MPa)} \tag{7}$$

The second part of the equivalent uniaxial stress–strain curve for confined concrete was determined by Eq. (8), which is a common equation proposed by Saenz (1964). This part starts from the proportional limit stress 0.5(f_{cc}) to the confined concrete strength (f_{cc}). This equation is used to represent the multidimensional stress and strain values for the equivalent uniaxial stress and strain values. The unknowns of the equation are the uniaxial stress (f) and strain (ε) values. Substituting the strain values (ε) between the proportional strain, which is equal to (0.5f_{cc}/E_{cc}), and the confined strain (ε_{cc}) gives the corresponding value of the confined concrete strength.

$$f = \frac{E_{cc}\varepsilon}{1+(R+R_E-2)(\varepsilon/\varepsilon_{cc}) - (2R-1)(\varepsilon/\varepsilon_{cc})^2 + R(\varepsilon/\varepsilon_{cc})^3} \tag{8}$$

where R_E and R values are calculated from Eqs. (9) and (10), respectively.

$$R_E = \frac{E_{cc}\varepsilon_{cc}}{f_{cc}} \tag{9}$$

$$R = \frac{R_E(R_\sigma - 1)}{(R_\varepsilon - 1)^2} - \frac{1}{R_\varepsilon} \tag{10}$$

where R_σ and R_ε are constants, values taken to be equal to 4.0, as recommended by Hu and Schnobrich (1989).

The third part of the confined concrete stress–strain curve is the descending part from the confined concrete strength (f_{cc}) to a value lower than or equal to $r{\cdot}k_3{\cdot}f_{cc}$ with the corresponding strain of 11ε_{cc}. The reduction factor (k_3) depends on the D/t ratio and the steel tube yield stress (f_y). The approximate value of k_3 can be calculated from empirical Eqs. (11) and (12) given by Hu et al. (2003).

$$k_3 = 1 \qquad 21.7 \leq (D/t) \leq 47 \tag{11}$$

$$k_3 = 0.0000339\left(\frac{D}{t}\right)^2 - 0.0100085\left(\frac{D}{t}\right) + 1.3491$$

$$47 \leq \left(\frac{D}{t}\right) \leq 150 \tag{12}$$

The reduction factor (r) was introduced by Ellobody et al. (2006), based on the experimental investigation conducted by Giakoumelis and Lam (2004). The value of r is taken as 1.0 for concrete with cube strength (f_{cu}) equal to 30 MPa. The value of r is taken as 0.5 for concrete with f_{cu} greater than or equal to 100 MPa.

3.3. Contact and interaction

The interface element was utilized to model the contact between the concrete and the steel tube. This element consists of master and slave surfaces that correspond to the matching contact faces of the steel tube and concrete elements. According to Capilla and García (2013), the friction coefficient for simulating the interaction between concrete and steel tubes in composite columns ranges from 0.2 to 0.8. In this study, a friction coefficient of 0.8 was adopted. The interface element permits surface separation under tensile forces but prevents penetration between the contacting surfaces. Additionally, the interaction between the column and the projectile was modelled as hard contact to accurately represent the impact conditions.

3.4. Boundary conditions

To simulate the motion of the impactor, it was given an initial velocity (8.05 m/s) in a direction perpendicular to the column while the rest of DOFs were constrained. The column was given a hinged-hinged boundary condition to simulate test.

4. Comparison of Results

In the following sections, the results obtained from analysis are compared with the experimental results. The compared results include shape of failure and Maximum displacement due to impact loading.

4.1. Deformed shape of column after impact

Figs. 9–20 represent a comparison between the deformed shape of the 12-tested specimens and the corresponding FE models.

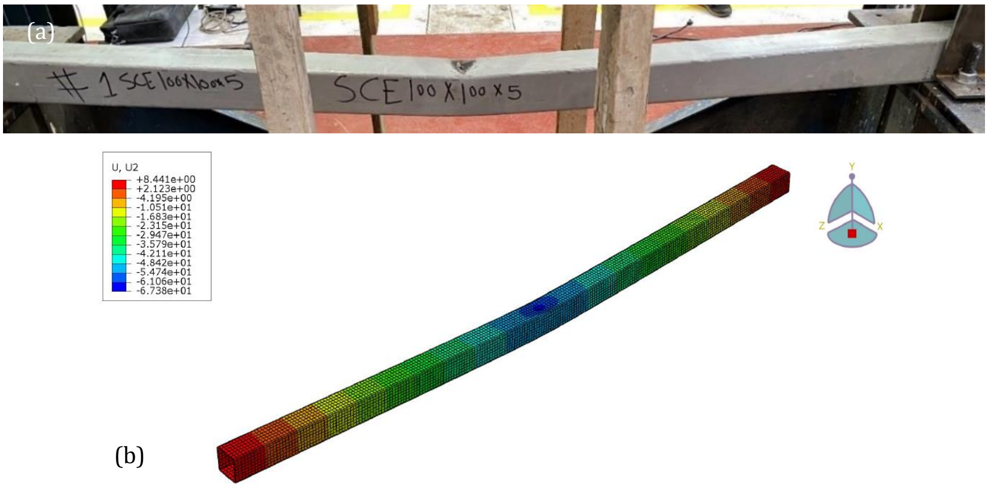

Fig. 9. Deformed shape of 100X100X5 empty single-cell column (SCC-E):
(a) Deformed shape of tested specimen; (b) Deformed shape of tested specimen's FE model.

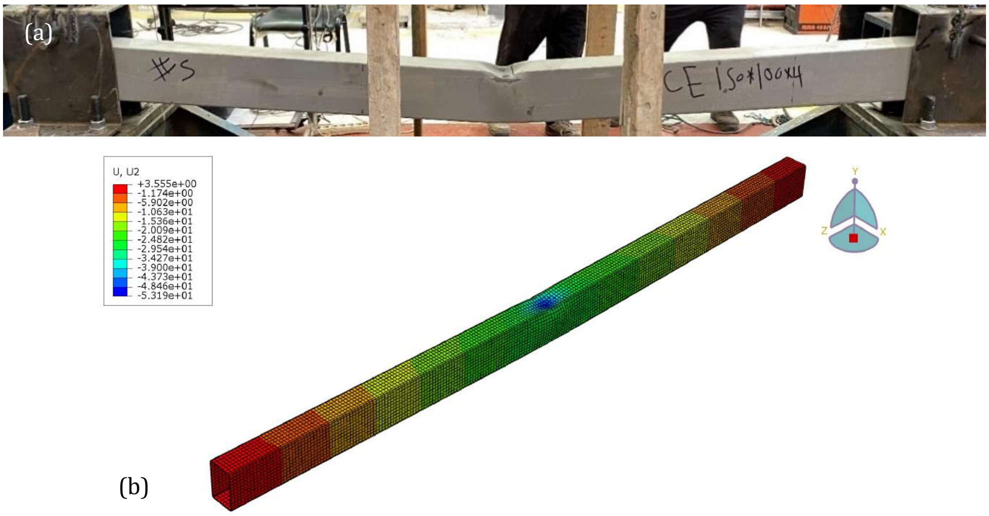

Fig. 10. Deformed shape of 100X150X4 empty single-cell column (SCC-E):
(a) Deformed shape of tested specimen; (b) Deformed shape of tested specimen's FE model.

Fig. 11. Deformed shape of 100X225X3 empty single-cell column (SCC-E):
(a) Deformed shape of tested specimen; (b) Deformed shape of tested specimen's FE model.

Fig. 12. Deformed shape of 100X100X5 filled single-cell column (SCC-F):
(a) Deformed shape of tested specimen; (b) Deformed shape of tested specimen's FE model.

Fig. 13. Deformed shape of 100X150X4 filled single-cell column (SCC-F):
(a) Deformed shape of tested specimen; (b) Deformed shape of tested specimen's FE model.

Fig. 14. Deformed shape of 100X225X3 filled single-cell column (SCC-F):
(a) Deformed shape of tested specimen; (b) Deformed shape of tested specimen's FE model.

Fig. 15. Deformed shape of 100X100X4X2 empty multi-cell column (MCC-E):
(a) Deformed shape of tested specimen; (b) Deformed shape of tested specimen's FE model.

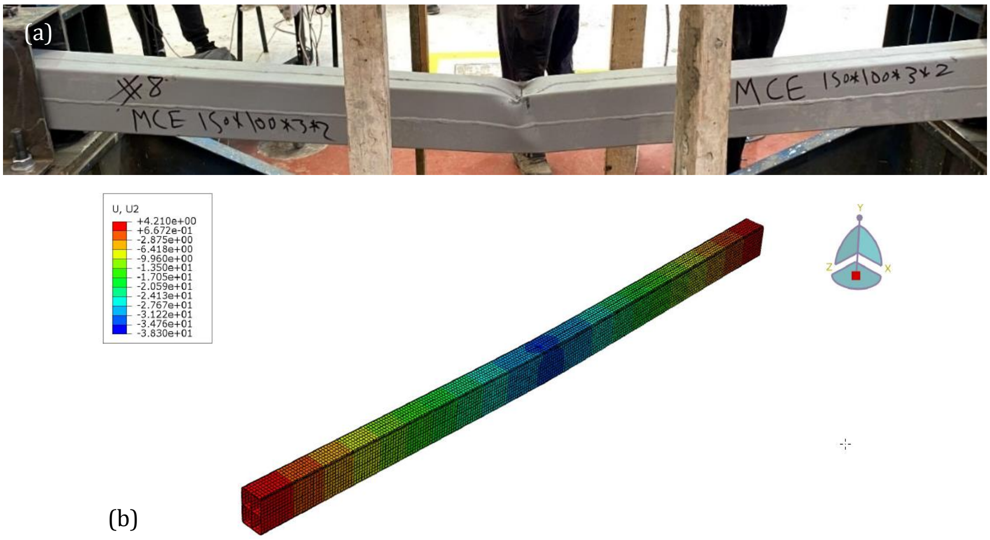

Fig. 16. Deformed shape of 100X150X3X2 empty multi-cell column (MCC-E):
(a) Deformed shape of tested specimen; (b) Deformed shape of tested specimen's FE model.

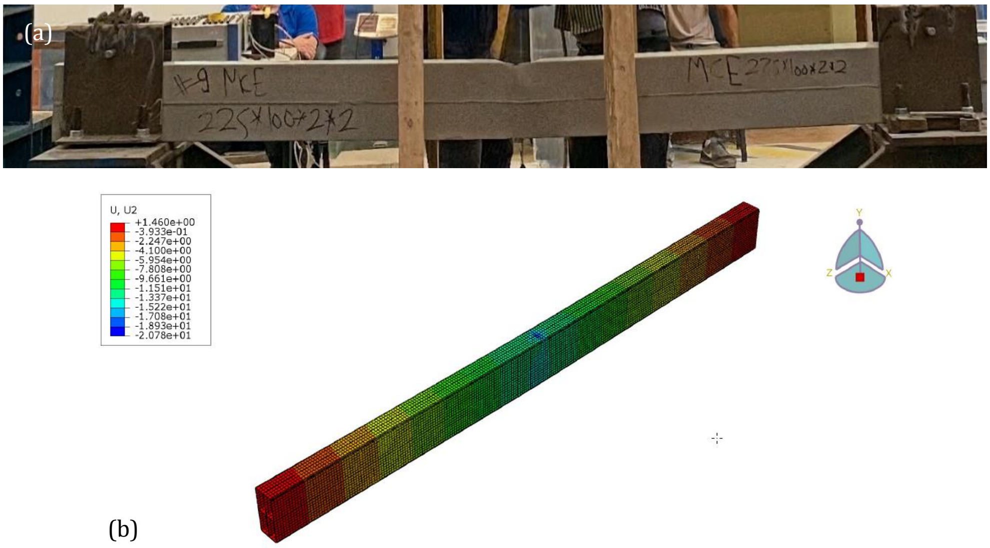

Fig. 17. Deformed shape of 100X225X2X2 empty multi-cell column (MCC-E):
(a) Deformed shape of tested specimen; (b) Deformed shape of tested specimen's FE model.

Fig. 18. Deformed shape of 100X100X4X2 filled multi-cell column (MCC-F):
(a) Deformed shape of tested specimen; (b) Deformed shape of tested specimen's FE model.

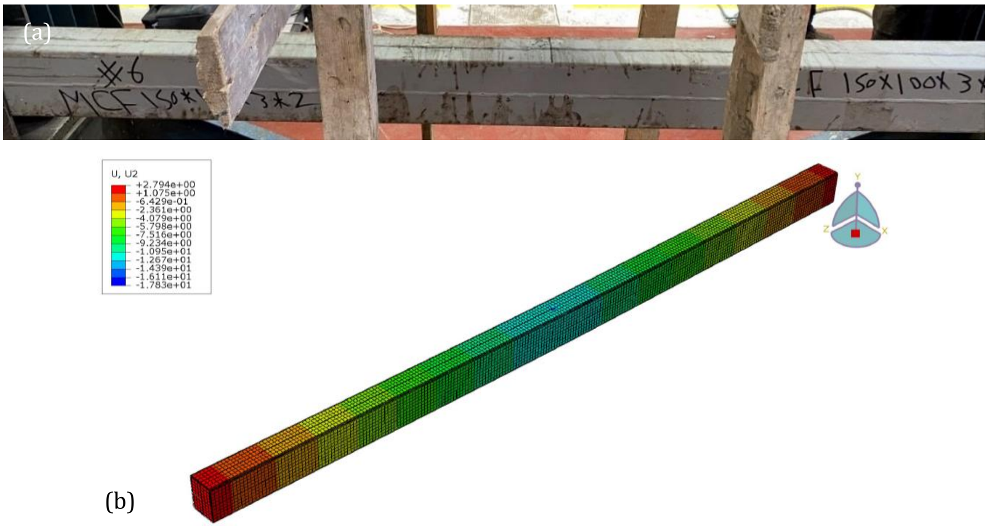

Fig. 19. Deformed shape of 100X150X3X2 filled multi-cell column (MCC-F):
(a) Deformed shape of tested specimen; (b) Deformed shape of tested specimen's FE model.

Fig. 20. Deformed shape of 100X225X2X2 filled multi-cell column (MCC-F):
(a) Deformed shape of tested specimen; (b) Deformed shape of tested specimen's FE model.

4.2. Max displacement at mid-point of sample

Table 2 provides a comparison between maximum displacements in experimental and analytical models. It is clear that the FE models represents the tests on steel and composite tubular columns under impact loading accurately.

5. Results of Analytical Models

Numerical analyses of the 12 models were performed under the same conditions. The main outcomes from analysis include maximum displacement at mid-span, maximum impact force, mode of failure and energy absorption.

Table 2. Comparison between experimental and FE models.

Concrete filling	*R*	Sample label	Maximum deflection (mm)		Difference (%)
			Experimental	FE model	
Empty columns	1.00	SCC-E (100X100X5)	46.485	52.500	11.46
		MCC-E (100X100X4X2)	60.937	59.165	-2.99
	1.50	SCC-E (100X150X4)	26.369	24.707	-6.73
		MCC-E (100X150X3X2)	29.993	32.072	6.48
	2.25	SCC-E (100X225X3)	9.522	10.424	8.65
		MCC-E (100X225X2X2)	18.564	18.092	-2.61
Concrete-filled columns	1.00	SCC-F (100X100X5)	38.644	34.715	-11.32
		MCC-F (100X100X4X2)	35.464	37.864	6.34
	1.50	SCC-F (100X150X4)	8.976	9.501	5.52
		MCC-F (100X150X3X2)	12.588	12.537	-0.40
	2.25	SCC-F (100X225X3)	4.251	4.689	9.34
		MCC-F (100X225X2X2)	5.736	5.221	-9.87

5.1. Mid-point displacement

The time-displacement curves for all models are illustrated in Figs. 21 and 22. The displacement of the lower side midpoint of each model was chosen as a reference point, as it provides a clear indication of model rigidity and strength. Fig. 21 compares the displacement of all concrete-filled single and multi-cell column models. It is evident that single-cell models exhibit smaller displacements compared to multi-cell columns with the same cross-sectional area. Specifically, the maximum displacement of the (100×100) single-cell model is reduced by approximately 8.32% compared to its multi-cell counterpart. Similarly, reductions of about 24.22% and 10.19% are observed for the (150×100) and (225×100) models, respectively. Fig. 22 presents a comparison of all empty single and multi-cell column models, showing that single-cell models consistently experience smaller displacements than multi-cell columns of the same cross-sectional area. The maximum displacement of the (100×100) single-cell empty model is reduced by approximately 11.26% compared to the multi-cell empty model. Additionally, reductions of about 22.96% and 42.38% are observed for the (150×100) and (225×100) models, respectively. A summary of the maximum displacement values for all models is provided in Fig. 23.

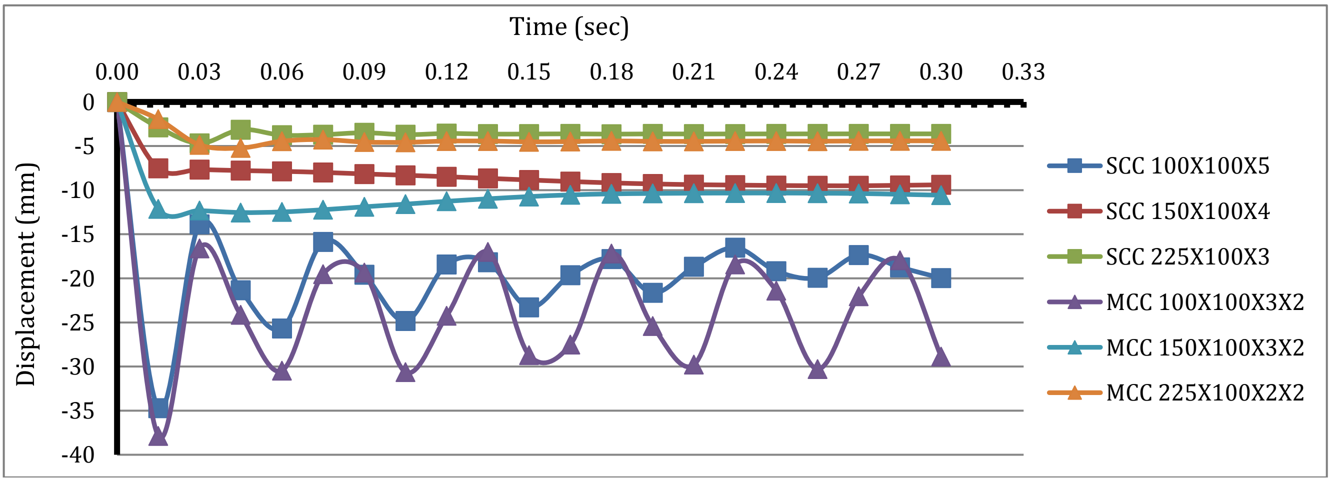

Fig. 21. Time-displacement relationships for concrete-filled columns.

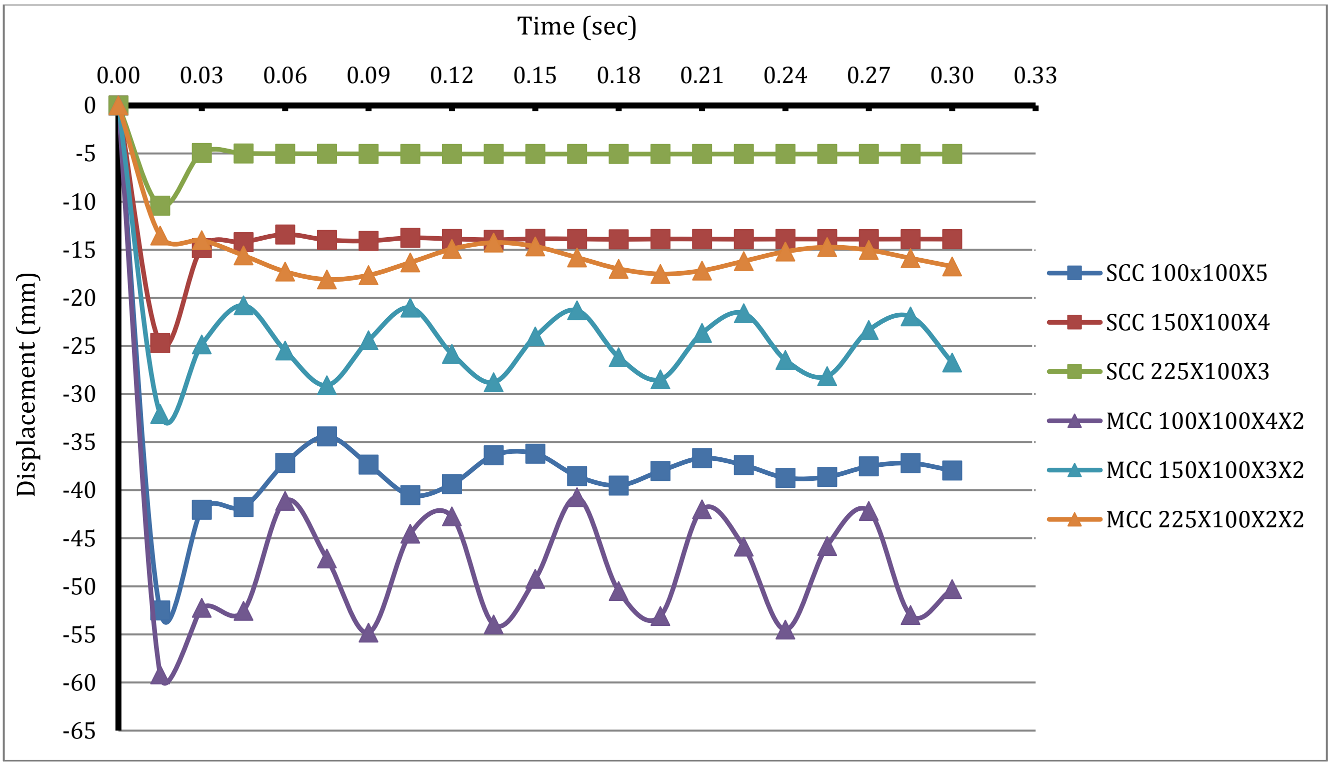

Fig. 22. Time-displacement relationships for empty columns.

These results are logical, as global deformation is primarily influenced by the moment of inertia. When two columns have the same cross-sectional area, the single-cell column possesses a greater moment of inertia than the multi-cell column. This is because, in single-cell columns, the material is concentrated along the periphery, placing it farther from the section's center of gravity, thereby enhancing rigidity and reducing deformation.

As illustrated in Fig. 23, the concrete-filled single-cell model with dimensions 225×100 mm exhibits the lowest maximum displacement of 4.689 mm, while the empty multi-cell model with dimensions 100×100 mm has the highest maximum displacement of 59.165 mm.

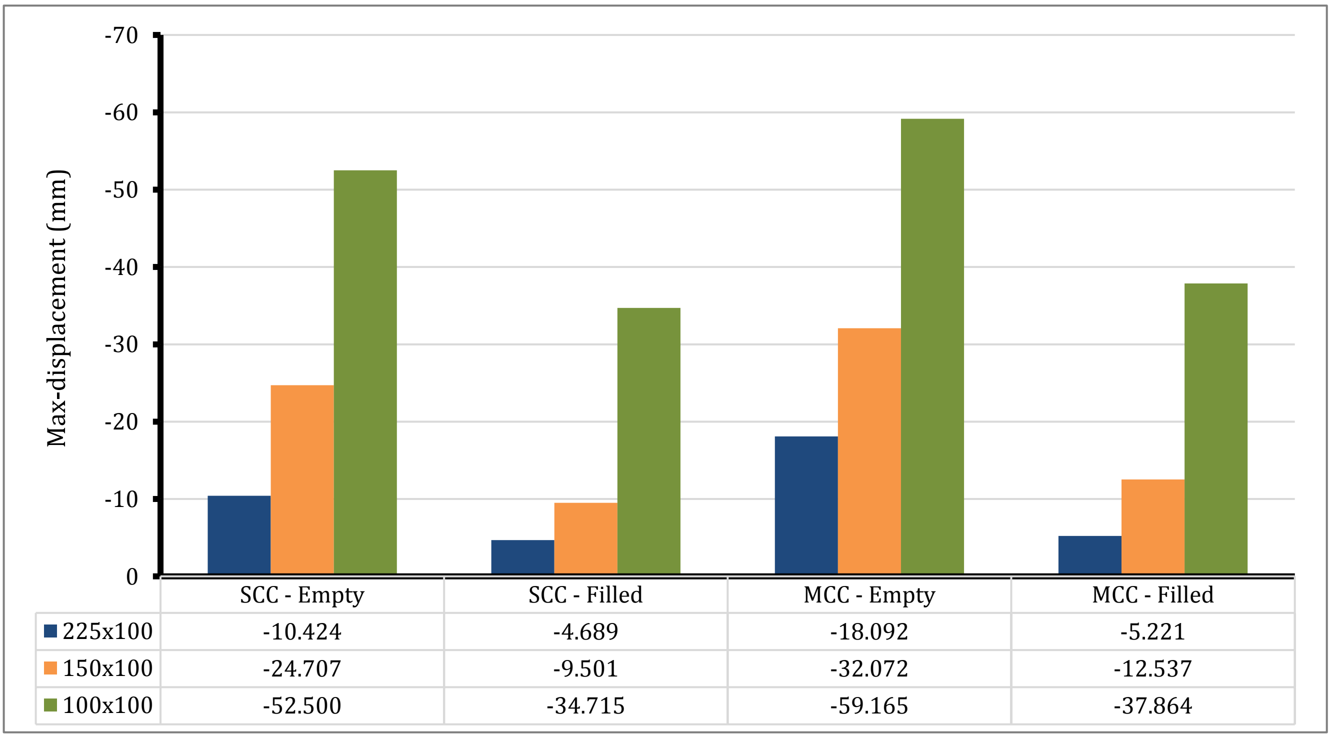

	SCC - Empty	SCC - Filled	MCC - Empty	MCC - Filled
■ 225x100	-10.424	-4.689	-18.092	-5.221
■ 150x100	-24.707	-9.501	-32.072	-12.537
■ 100x100	-52.500	-34.715	-59.165	-37.864

Fig. 23. Maximum displacements for all models.

5.2. Impact load capacity

Fig. 24 summarizes and explains the maximum impact forces for all models. The determination of maximum impact force provides a more precise correlation with absorbed energy. The figure indicates that the concrete-filled single-cell model with dimensions 225×100 mm exhibits the highest impact force among all models. This highlights the superior impact resistance of concrete-filled models compared to empty ones, as well as the influence of model dimensions on the amount of impact force that can be sustained.

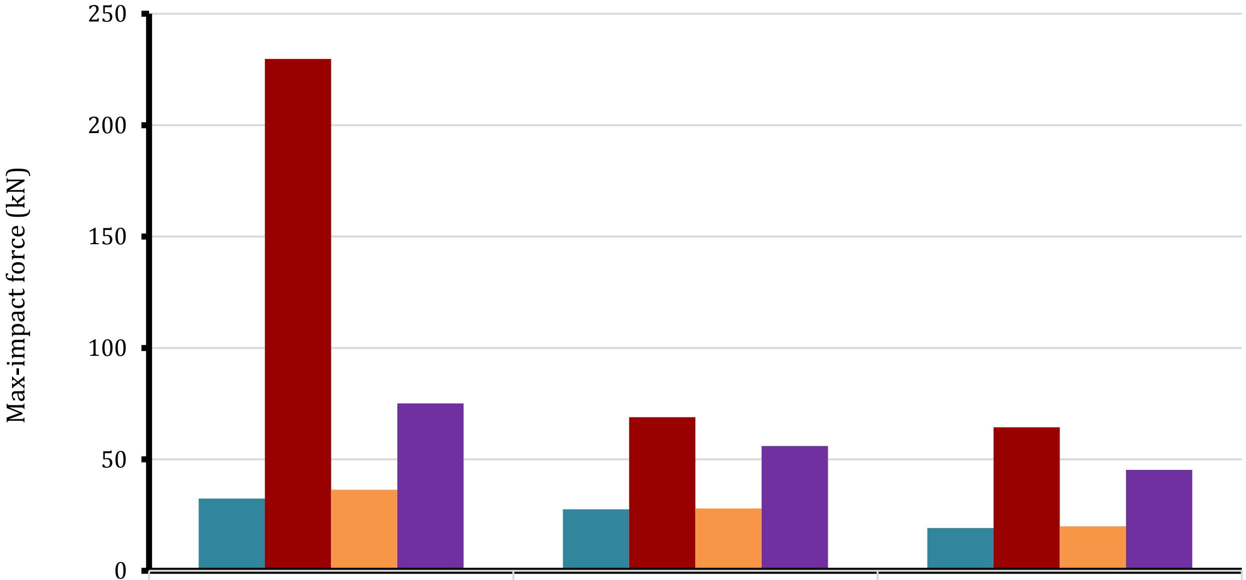

	225x100	150x100	100x100
🟦 SCC - Empty	32.425	27.630	19.161
🟥 SCC - Filled	229.715	68.956	64.376
🟧 MCC - Empty	36.366	27.941	19.967
🟪 MCC - Filled	75.108	55.989	45.291

Fig. 24. Maximum impact force for all models.

5.3. Energy absorption

When a structure is impacted by a moving object, the kinetic energy of the projectile is transformed into strain energy within the structure, which is partially dissipated through local plastic deformation and strain energy. Energy-absorbing structures undergo significant deformation to absorb the impact energy while maintaining their structural integrity. Yin et al. (2014, 2015) introduced the concept of "crashworthiness indicators" to evaluate a structure's ability to absorb energy. These indicators include energy absorption (EA), specific energy absorption (SEA), mean crushing force (MCF), and crash load efficiency (CLE). Energy absorption (EA) can be defined in terms of the deflection of the structural element. According to ACI Committee 363, energy absorption is determined by the toughness of mid-span deflection (displacement). This is calculated as the total area under the load-deflection curve from the origin to the point of rupture, as expressed in Eq. (13).

$$EA = \int_0^d F(x)\,dx \qquad (13)$$

where d is the crushing displacement and F denotes the impact force.

For all column models with dimensions 225×100 mm, the highest and lowest energy absorption values were recorded at 4214.972 J and 1204.036 J for the concrete-filled single-cell and empty single-cell models, respectively. The increased energy absorption in filled models can be attributed to the enhanced stiffness provided by the concrete filling, which helps distribute the impact force over a larger cross-sectional area. Across all model groups, the concrete-filled single-cell column exhibits the highest energy absorption, while the empty single-cell model has the lowest. In multi-cell models, the energy absorbed by the empty multi-cell column is either greater than or nearly equal to that of the concrete-filled multi-cell column. This performance may be due to the presence of cross-steel webs, which contribute to stiffness, reducing the impact of concrete filling on overall rigidity.

However, in models with dimensions 100×100 mm, the concrete-filled multi-cell model absorbs more energy than its empty counterpart. This is because, in these models, stiffness is nearly equal along both the horizontal and vertical axes, making the filled multi-cell model more rigid and better able to absorb impact energy. The energy absorption of all models is illustrated in Fig. 25.

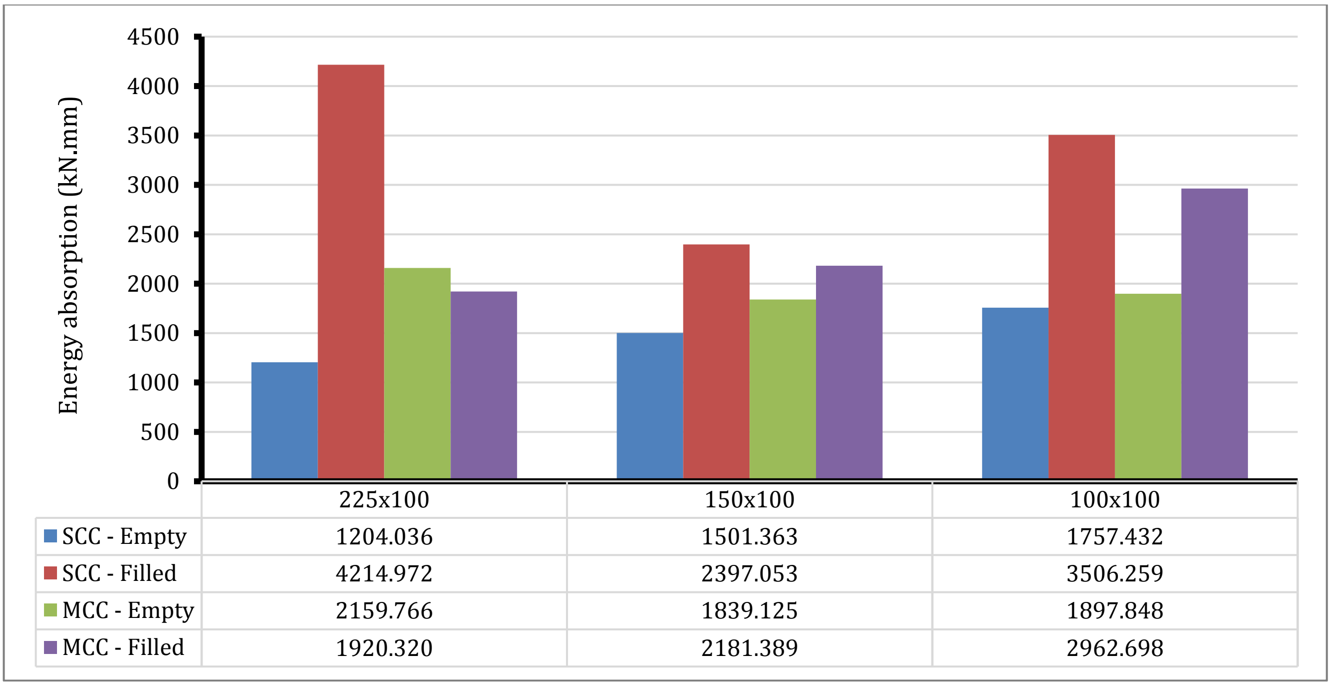

	225x100	150x100	100x100
🟦 SCC - Empty	1204.036	1501.363	1757.432
🟥 SCC - Filled	4214.972	2397.053	3506.259
🟩 MCC - Empty	2159.766	1839.125	1897.848
🟪 MCC - Filled	1920.320	2181.389	2962.698

Fig. 25. Energy absorption for all models.

5.4. Failure modes

For all empty single-cell column models, the primary failure mode was local buckling. In contrast, in all concrete-filled column models, the presence of concrete significantly reduced the effects of local buckling. A similar effect was observed in empty multi-cell column models, where the presence of cross-steel webs helped mitigate local buckling. Fig. 26 illustrates the local buckling failure of empty single-cell column models with various dimensions under impact loading. Figs. 27 and 28 depict the global deformation of both single and multi-cell models, including concrete-filled and empty multi-cell columns, under impact loading. These figures clearly highlight the differences in local buckling behavior between empty and concrete-filled column models.

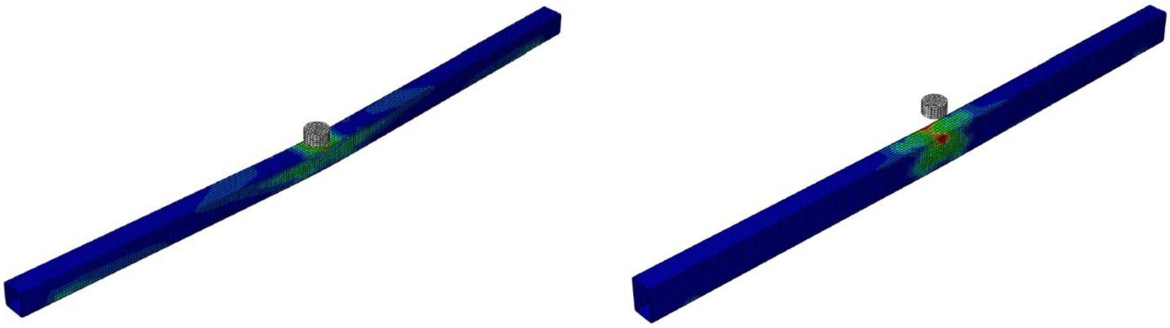

(a) 100×100 mm empty single-cell model (b) 150×100 mm empty single-cell model

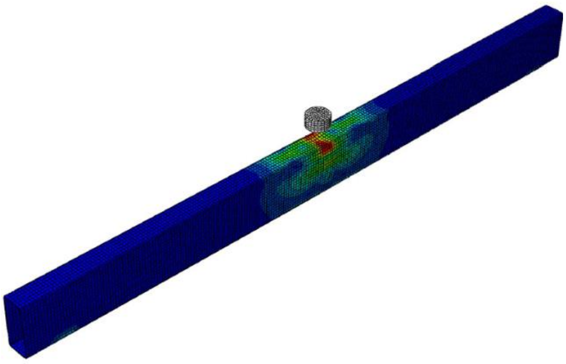

(c) 225×100 mm empty single-cell model

Fig. 26. Local buckling effects for empty single-cell models after impact load.

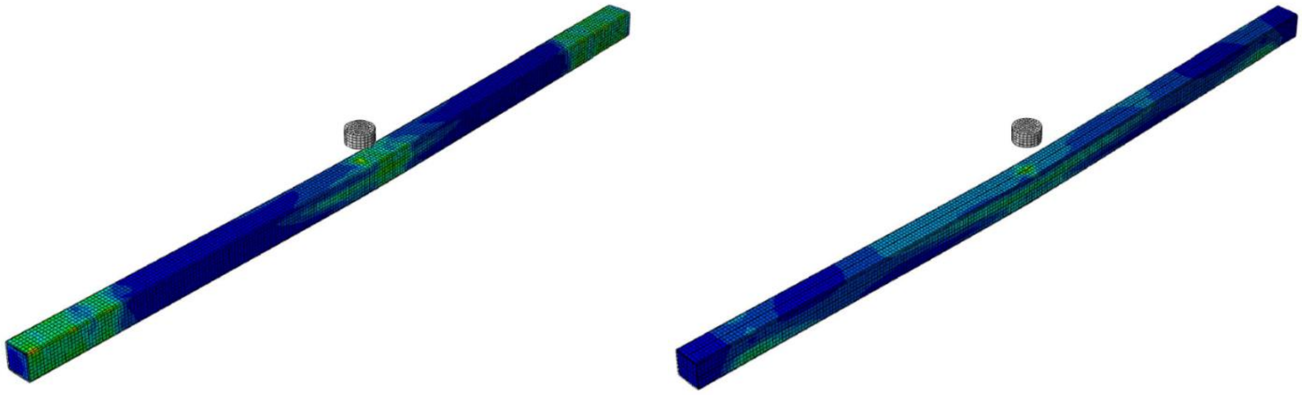

(a) 100×100 mm filled single-cell model (b) 100×100 mm filled multi-cell model

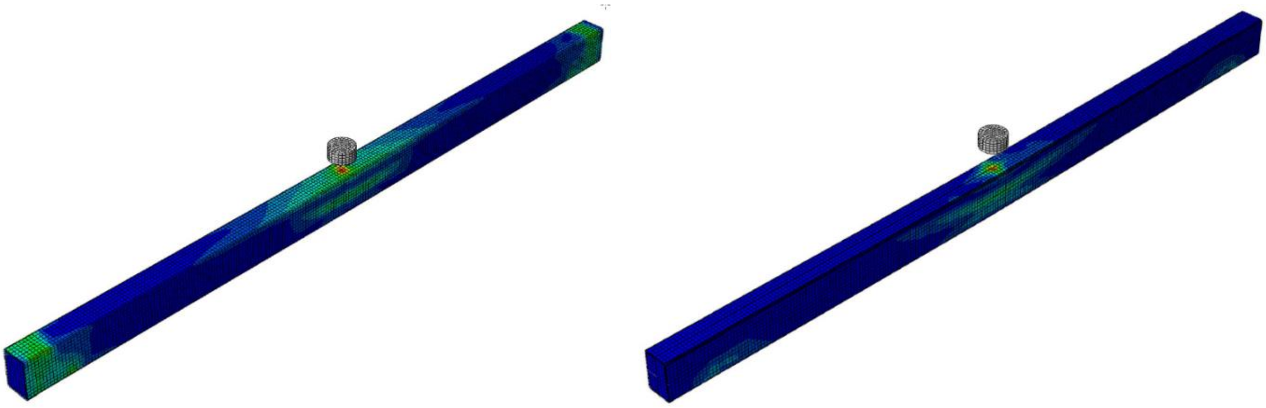

(c) 150×100 mm filled single-cell model (d) 150×100 mm filled multi-cell model

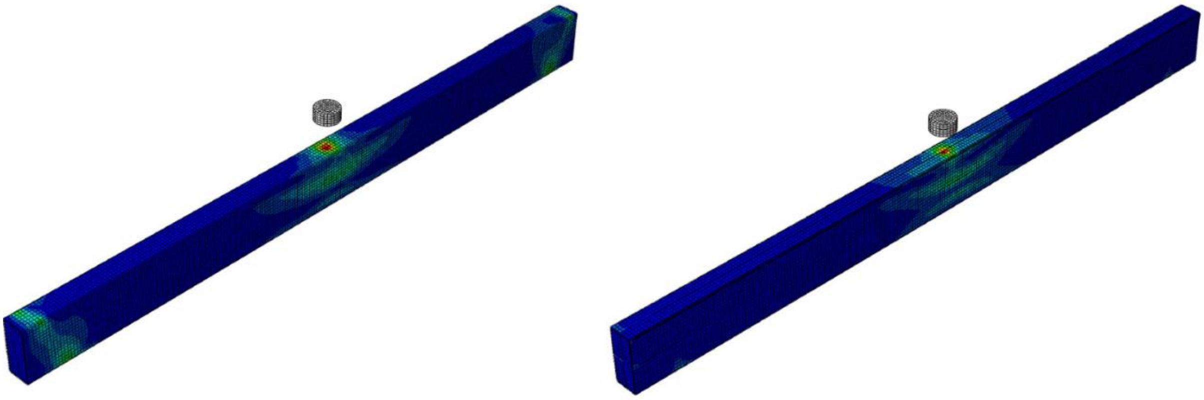

(e) 225×100 mm filled single-cell model (f) 225×100 mm filled multi-cell model

Fig. 27. Global deformations for concrete-filled single- and multi-cell models after impact load.

5.5. Rectangularity ratio effect

The rectangularity ratio, *R*, is the ratio of the height to the width of the section, which is one of the most important factors that have been considered in the current study. The effects of rectangularity ratio on both force - displacement and absorbed energy are presented in Figs. 29–31.

Fig. 29 illustrates the effect of *R* on maximum impact force which can be noted that max-impact force increases with increasing *R*. The increasing percentage has reached 257% when the *R* ratio was increased by 2.25% in case of filled single-cell model. In all models, there is a marked increase in maximum impact force with increasing *R*. Fig. 30 illustrates effect of *R* on maximum mid-point displacement which decreases with increasing of *R*. For example, empty multi-cell model recorded maximum mid-point displacement of 59.165 mm when *R* equals to 1 and recorded 18.092 mm when *R* equals to 2.25 with decreasing percentage of 69.42%. In all models, there is a marked decrease in maximum mid-point displacement with increasing *R*. Fig. 31 illustrates effect of *R* on energy absorbed which shows a difference in the effect of *R* on the amount of energy absorbed which decreases when the ratio reaches 1.50 and then increase when the ratio reaches 2.25 in case of filled single-cell. But in case of empty single-cell, increasing *R* leads to deceasing in amount of energy absorbed by model which may be because dissipation of energy in local buckling under falling impactor.

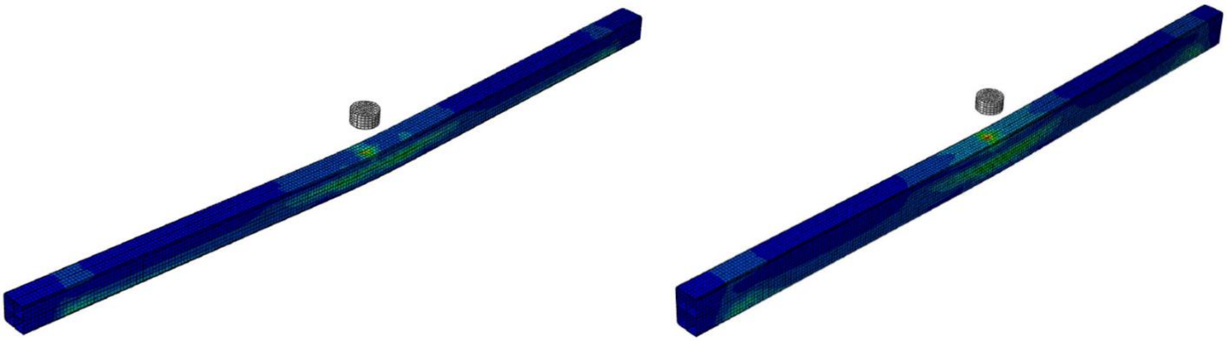

(a) 100×100 mm empty multi-cell model (b) 150×100 mm empty multi-cell model

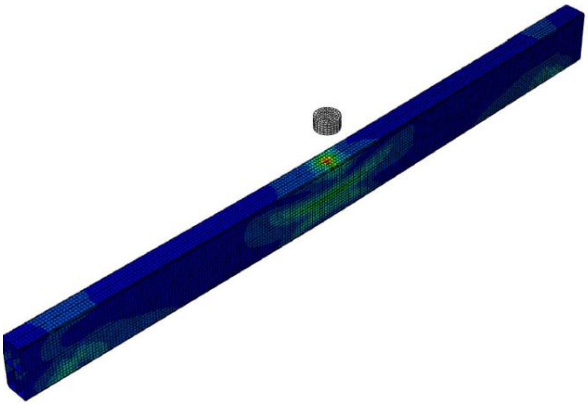

(c) 225×100 mm empty multi-cell model

Fig. 28. Global deformations for empty multi-cell models after impact load.

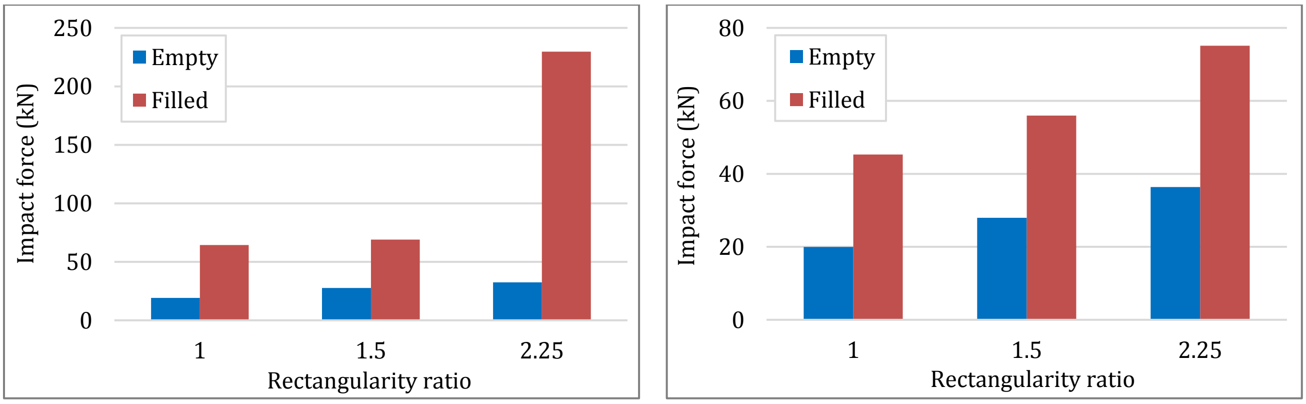

(a) Single-cell models (b) Multi-cell models

Fig. 29. Effect of rectangularity ratio on maximum impact force.

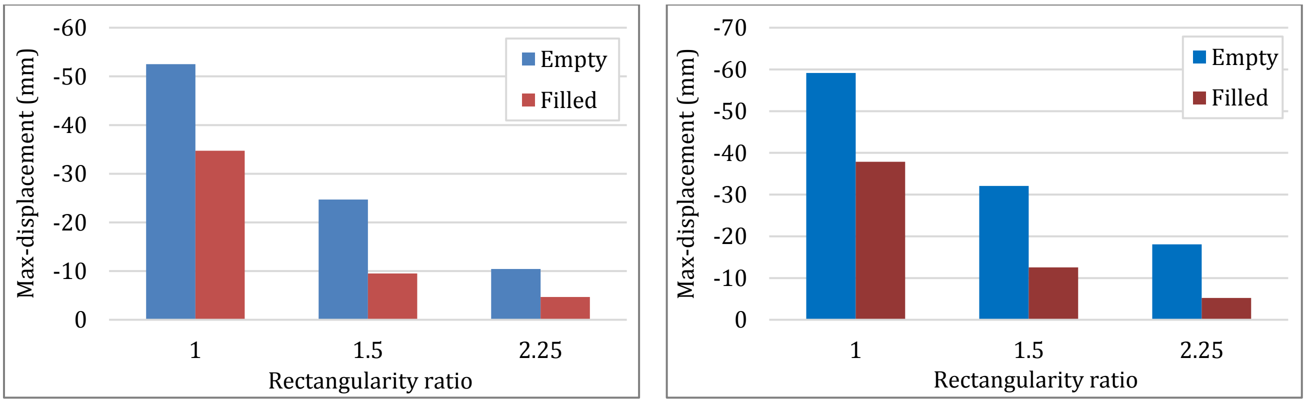

(a) Single-cell models (b) Multi-cell models

Fig. 30. Effect of rectangularity ratio on maximum mid-point displacement.

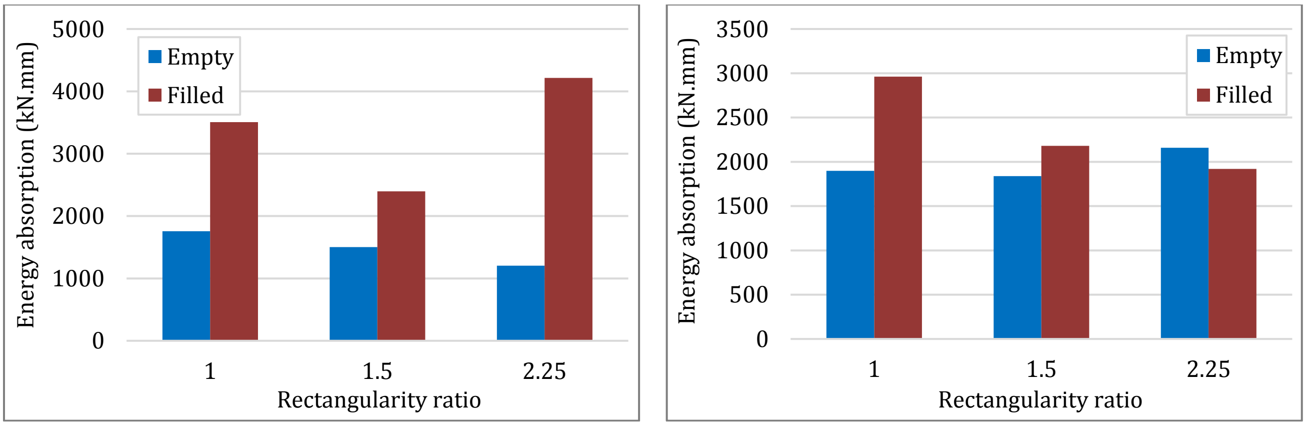

(a) Single-cell models (b) Multi-cell models

Fig. 31. Effect of rectangularity ratio on energy absorption.

6. Conclusions

This study examined the behavior of single and multi-cell steel columns, both with and without concrete filling, and analyzed the effect of section dimensions (rectangularity ratio) on their performance.

Based on the experimental and modeling results, the following conclusions were drawn:

- For all models, single-cell columns exhibited lower displacement values compared to multi-cell columns. This can be attributed to the influence of the moment of inertia on global deformations. Given the same cross-sectional area, a single-cell column has a greater moment of inertia than a multi-cell column, as its material is distributed along the periphery, placing it farther from the section's center of gravity.
- The internal division of a column into multiple cells significantly reduced local buckling under impact by increasing the section's local stiffness. A similar stiffening effect was observed with concrete filling.
- For empty models, multi-cell columns absorbed more energy than single-cell columns, indicating that the impactor's kinetic energy was effectively converted into strain energy within the column, which was dissipated through local plastic deformation. However, concrete-filled models did not follow this trend, as concrete, unlike steel, is a brittle material that lacks the ability to undergo large deformation to absorb impact energy without compromising its structural integrity.
- The rectangularity ratio (*R*) had a significant effect on impact force and mid-point displacement. An increase of 2.25% in *R* resulted in an increase of 257% in impact force and a reduction of 69.42% in mid-point displacement.
- For empty single-cell columns, an increase in *R* led to a decrease in energy absorption. This may be due to energy dissipation through local buckling under the falling impactor.

Acknowledgements

None declared.

Funding

The authors received no financial support for the research, authorship, and/or publication of this manuscript.

Conflict of Interest

The authors declared no potential conflicts of interest with respect to the research, authorship, and/or publication of this manuscript.

Author Contributions

All of the authors made substantial contributions to conception and design, or acquisition of data, or analysis and interpretation of data; were involved in drafting the manuscript or revising it critically for important intellectual content; and gave final approval of the version to be published.

Data Availability

The datasets created and/or analyzed during the current study are not publicly available, but are available from the corresponding author upon reasonable request.

REFERENCES

ABAQUS User's Guide (2014). Abaqus Documentation User's Guide. s.l.: Dassault Systemes, Simulia Corp.

ACI 318-19 (2019). Building Code Requirements for Structural Concrete and Commentary. American Concrete Institute, Farmington Hills, MI.

Ahmed N, Xue P, Kamran M, Zafar N, Mustafa A, Zahran M (2017). Investigation of the energy absorption characteristics of metallic tubes with curvy stiffeners under dynamic axial crushing. *Latin American Journal of Solids and Structures*, 14(7), 1443-1463.

Al-Thairy H (2012). Behaviour and Design of Steel Columns Subjected to Vehicle Impact. *Ph.D. thesis*, University of Manchester, Manchester, UK.

Balmer GG (1949). Shearing strength of concrete under high triaxial stress computation of Mohr's envelope as a curve. SP-23, Structural Research Laboratory, U.S. Bureau of Reclamation.

Bambach M, Zhao H, Grzebieta R (2008). Hollow and concrete filled steel hollow sections under transverse impact loads. *Engineering Structures*, 30(10), 2859-2870.

Bedage SD, Shinde DN (2015). Concrete filled steel tubes subjected to axil compression. *International Journal of Research in Engineering and Technology*, 4(6), 459-464.

Bi J, Fang H, Wang Q, Ren X (2010). Modeling and optimization of foam-filled thin-walled columns for crashworthiness designs. *Finite Elements in Analysis and Design*, 46(9), 698–709

Campbell A (1994). Axial Load Capacity of Circular Steel Tube Columns Filled with High Strength Concrete. *M.Sc. thesis,* Victoria University of Technology, Victoria, Australia.

Capilla AE, García MLR (2013). Finite element modelling of innovative concrete-filled tubular columns under room and elevated temperatures. In: *European Project FRISCC "Fire Resistance of Innovative and Slender Concrete Filled Tubular Composite Columns"*, Engineering, Materials Science (Editor UPV).

Chu K (2014). Axial load behaviour of steel tube columns in-filled with various high-performance concretes. *M.Sc. Thesis,* Ryerson University, Toronto, Ontario, Canada.

EOS1658-4/2008 (2008) Testing of concrete – Part 3: Making and curing test specimens (ISO 1920-3:2004 equivalent). Egyptian Organization for Standardization and Quality, Cairo, Egypt.

Elkady A (2023). ABAQUS_SteelMat_Generator: A tool for generating metal plastic and damage parameters for ABAQUS. *Jurnal Ilmu Pendidikan*, 7(2), 809-820.

Ellobody, E, Young B, Lam D (2006). Behaviour of normal and high strength concrete-filled compact steel tube circular stub columns. *Journal of Constructional Steel Research,* 62(7), 706-715.

Feng Z, Wang X, Zhang S, Chu Y (2022). Experimental investigation on cantilever square CFST columns under lateral continuous impact loads. *Journal of Constructional Steel Research*, 196(2), 107416.

Giakoumelis G, Lam D (2004). Axial capacity of circular concrete-filled tube columns. *Journal of Constructional Steel Research,* 60(7), 1049-1068.

Guler S, Lale E, Aydogan M (2013). Behaviour of SFRC filled steel tube columns under axial load. *Journal of Advanced Steel Construction*, 9(1), 14-25.

Hassam M, Guo LH, Wang YH (2020). Experimental and numerical investigation of cross-shaped stub CFSTs under axial compression. *Magazine of Concrete Research*, 73(23), 1225-1240.

Hassam M, Geo LH, Chen J (2022). Concentric and eccentric compression performance of multiple-cell cruciform CFSTs. *Journal of Constructional Steel Research*, 192(3), 107205.

Hou CC, Han LH (2018). Life-cycle performance of deteriorated concrete-filled steel tubular (CFST) structures subject to lateral impact. *Thin-Walled Structures*, 132(11), 362-374.

Hu HT, Schnobrich WC (1989). Constitutive modeling of concrete by using nonassociated plasticity. *Journal of Materials in Civil Engineering*, 1(4), 199–216.

Hu HT, Huang CS, Wu MH, Wu YM (2003). Nonlinear analysis of axially loaded concrete-filled tube columns with confinement effect. *Journal of Structural Engineering ASCE,* 129(10), 1322–1329.

ISO 1920-3:2004 (2004). Testing of concrete – Part 3: Making and curing test specimens. International Organization for Standardization, Geneva, Switzerland.

Kirankumar P, Babu S, Ram D (2016). Comparative study of concrete filled steel tube columns under axial compression. *International Journal of Constructive Research in Civil Engineering*, 2(2), 11-17.

Krolak M, Kowal-Michalska K, Mania R, Swiniarski, J (2007). Experimental tests of stability and load carrying capacity of compressed thin-walled multi-cell columns of triangular cross-section. *Thin-Walled Structures*, 45(10), 883-887.

Królak M, Mechalska K, Mania R, Swiniarski J (2009). Stability and load-carrying capacity of multi-cell thin-walled columns of rectangular cross-sections. *Journal of Theoretical and Applied Mechanics*, 47(2), 435-456.

Mander JB, Priestley MJN, Park R (1988). Theoretical stress–strain model for confined concrete*. Journal Structural Engineering,* 114(8), 1804-1826.

Patil B, Mohite P (2014). Parametric study of square concrete filled steel tube columns subjected to concentric loading. *International Journal of Engineering Research and Applications*, 4(8), 109-112.

Richart FE, Brandtzaeg A, Brown RL (1928). A study of the failure of concrete under combined compressive stresses. *Bulletin 185, Univ. of Illinois Engineering Experimental Station*, Champaign, 111.

Saenz LP (1964). Discussion of 'Equation for the stress–strain curve of concrete' by Desayi P. Krishnan S. *Journal of American Concrete Institute*, 61, 1229–1235.

Seangatith S (1997). Characterization and analysis of composite beams subjected to impact loads. *Ph.D. thesis*, University of Texas at Arlington, Arlington, TX, USA.

Sofi M (2015). A review on energy absorption of multi cell thin walled structure*. Journal of Advanced Review on Scientific Research*, 16(1), 18-24.

Song J, Chen Y, Lu G (2012). Axial crushing of thin-walled structures with origami patterns. *Thin-Walled Structures*, 54, 65–71.

Tran T, Hou S, Han X, Chau M (2015). Crushing analysis and numerical optimization of angle element structures under axial impact loading. *Composite Structures*, 119, 422–435.

Tran T, Hou S, Han X, Nguyen N, Chau M (2014). Theoretical prediction and crashworthiness optimization of multi-cell square tubes under oblique impact loading. *International Journal of Mechanical Sciences*, 89, 177–193.

Uslu F, Taşkın K (2024). Experimental and Finite element method investigation of axial load carrying capacity of concrete filled circular steel tube columns according to different slenderness ratios. *International Journal of Steel Structures*, 24(3), 619–634.

Wardenier J (2001). Hollow sections in structural applications. Edited by CIDECT-Comité International pour le Développement et l'Etude de la Construction Tubulaire, John Wiley & Sons, Australia.

Wardenier J, Packer J, Zhao X-L, van der Vegte G (2010). Hollow sections in structural applications. 2nd edition, Edited by CIDECT - Comité International pour le Développement et l'Etude de la Construction Tubulaire. Bouwen met staal, Zeotemeer, Netherlands.

Wu S, Zheng G, Sun G, Liu Q, Li G, Li Q (2016). On design of multi-cell thin-wall structures for crashworthiness. *International Journal of Impact Engineering*, 88, 102–117.

Yang X, Yang H, Zhang S (2019). Rate-dependent constitutive models of S690 high- strength structural steel. *Construction and Building Materials*, 198(7), 597–607.

Yang H, Zhang JC, Du GF, Mao ZH (2021). Experimental study on the behavior of cross-shaped concrete-filled steel tubular intermediate long columns under axial compression. *Progress in Steel Building Structures*, 23(7), 49-57.

Yin H, Wen G, Liu Z, Qing Q (2014). Crashworthiness optimization design for foam-filled multi-cell thin-walled structures. *Thin-Walled Structures*, 75, 8–17.

Yin H, Xiao Y, Wen G, Qing Q, Deng Y (2015). Multiobjective optimization for foam-filled multi-cell thin-walled structures under lateral impact. *Thin-Walled Structures*, 94, 1–12.

Yousuf M, Uy B, Tao Z (2010). Experimental behaviour of pre-compressed concrete-filled stainless steel tubular columns subjected to transverse impact loads. *4th International Conference on Steel & Composite Structure*, 21-23 July 2010, Sydney, Australia.

Yousuf M, UY B, Tao Z, Remennikov A, Liew R (2012). Behaviour and resistance of hollow and concrete-filled mild steel columns due to transverse impact loading. *Australian Journal of Structural Engineering*, 13(1), 65-80.

Zhang X, Cheng G, Zhang H (2006). Theoretical prediction and numerical simulation of multi-cell square thin-walled structures. *Thin-Walled Structures*, 44(11), 1185–1191.

Zheng Y, Lin Y, Ma S (2024). Axial compressive behavior of stiffened and multi-cell cross-shaped CFST stub columns. *Constructional Steel Research*, 213, 108399.

Zhu A-Z, Xu W, Gao K, Ge H-B, Zhu J-H (2018). Lateral impact response of rectangular hollow and partially concrete-filled steel tubular columns. *Thin-Walled Structures*, 130(9), 114-131.

Zhu Y, Gardner L, Yang H (2023). Experimental investigation into the transverse impact performance of high-strength circular CFST members*. Thin-Walled Structures,* 189(3), 110923.